LIGHT FIDELITY TRACKING SYSTEM

An Undergraduate Research Scholars Thesis

by

AMANDA ABOUJAOUDE[1], MICHAEL SPORKIN[2], RYAN QUINN[3]

Submitted to the LAUNCH: Undergraduate Research office at
Texas A&M University
in partial fulfillment of requirements for the designation as an

UNDERGRADUATE RESEARCH SCHOLAR

Approved by
Faculty Research Advisor: Dr. Christi K. Madsen

May 2021

Majors: Electrical Engineering[1]
Electrical Engineering[2]
Electrical Engineering[3]

RESEARCH COMPLIANCE CERTIFICATION

Research activities involving the use of human subjects, vertebrate animals, and/or biohazards must be reviewed and approved by the appropriate Texas A&M University regulatory research committee (i.e., IRB, IACUC, IBC) before the activity can commence. This requirement applies to activities conducted at Texas A&M and to activities conducted at non-Texas A&M facilities or institutions. In both cases, students are responsible for working with the relevant Texas A&M research compliance program to ensure and document that all Texas A&M compliance obligations are met before the study begins.

We, Amanda Aboujaoude, Michael Sporkin, Ryan Quinn, certify that all research compliance requirements related to this Undergraduate Research Scholars thesis have been addressed with my Research Faculty Advisor prior to the collection of any data used in this final thesis submission.

This project did not require approval from the Texas A&M University Research Compliance & Biosafety office.

TABLE OF CONTENTS

ABSTRACT

Light Fidelity Tracking System

Amanda Aboujaoude[1], Michael Sporkin[2], Ryan Quinn[3]
Department of Electrical and Computer Engineering[1]
Department of Electrical and Computer Engineering[2]
Department of Electrical and Computer Engineering[3]
Texas A&M University

Research Faculty Advisor: Dr. Christi K. Madsen
Department of Electrical and Computer Engineering
Texas A&M University

The proposed project will establish a baseline for a LiFi system through the implementation of a restorable stationary link to transmit an acceptable amount of power between a stationary base module and a mobile user module across the steradian application range. Since existing LiFi systems have limited mobility tracking, if any, this project will improve the widespread applicability of LiFi communication and increase the versatility of system use. The laser diode-based system will implement a searching and tracking methodology that facilitates communication between a stationary base and a mobile user through the establishment of a representative link. Transmission of power from the laser diode to a photodetector on the opposing module will represent a link connection that could employ methods of optical communication data transfer. Upon movement of the mobile user in a given space, the link can be re-established. The system is being developed as an integrated product of four functional subsystems: an optical path that facilitates the representative connection; a searching subsystem that enables the base and mobile user to locate each other; a motor

subsystem that aligns the modules to form the representative link; and a method of reading and recording output power to verify connection. The focus of research will be the tracking methodology, a significant challenge associated with the narrow-beam and directionally dependent laser diode responsible for communication. The objective output product will be a starting point for further research into faster, cheaper, and more efficient means of tracking for optical wireless communication systems.

DEDICATION

To our friends, families, instructors, and peers who supported us throughout the research process.

ACKNOWLEDGEMENTS

Contributors

We would like to thank our faculty advisor, Dr. Christi Madsen, for her guidance and support throughout the course of this research.

Thanks also go to our friends and colleagues and the department faculty and staff for making our time at Texas A&M University a great experience.

The research materials analyzed/used for Light Fidelity Tracking System were provided by the Texas A&M University Department of Electrical and Computer Engineering, Dr. Christi Madsen, Amanda Aboujaoude, Michael Sporkin, and Ryan Quinn.

Funding Sources

Undergraduate research was supported by Dr. Christi Madsen and the Department of Electrical and Computer Engineering at Texas A&M University.

No additional funding was received.

NOMENCLATURE

AD2	National Instruments Analog Discovery Device 2
ADC	Analog to Digital Converter
CCS	Constant Current Source
FAST	Follow and Search Tracking
GUI	Graphical User Interface
IC	Integrated Circuit
LD	Laser Diode
LDC	Laser Diode Controller
LED	Light Emitting Diode
LiFi	Light Fidelity
MOSFET	Metal Oxide Semiconductor Field Effect Transistor
NIR	Near Infrared
OWC	Optical Wireless Communication
PC	Photoconductive Mode
PD	Photodetector/Photodiode
PV	Photovoltaic Mode
RSL	Representative Stationary Link
TIA	Transimpedance Amplifier
USB	Universal Serial Bus
VCSEL	Vertical Cavity Surface Emitting Laser
WiFi	Wireless Fidelity

1. INTRODUCTION

Growing device interconnectivity demands better methods of communication. WiFi continues to improve, but bandwidth limitations inhibit both speed of data transfer and indefinite expansion of devices to networks. Wired connections are faster and more reliable, but lack the option of mobility demanded by industry and consumers alike. Optical Wireless Communication (OWC) aims to bridge this gap by providing high speed connectivity through the use of visible, infrared, and ultraviolet light on the electromagnetic spectrum [1]. Light fidelity (LiFi) systems operate by rapidly modulating visible light at a speed imperceptible to the human eye, using the binary on/off signal to communicate large quantities of data to remote photodetectors [2].

A common light source used in LiFi are Vertical Cavity Surface Emitting Lasers (VCSEL) for their support of high modulation speeds and a large bandwidth. However, their directional nature limits the field of reception and requires a complex optical path to reach a photodetector and requires power safety considerations. Additionally, mass commercialization of LiFi requires mobility. VSCEL's promise of faster connectivity than WiFi loses traction if users are confined to one location, since existing fiber optic cables already provide a high-speed link when the user can stay physically connected and stationary [3]. The historical and well-researched approach to OWC tracking and alignment systems incorporates beam steering as the main approach [4]. Such beam steering systems include optical components which cost thousands of dollars, such as spatial light modulators which cost over ten thousand dollars each [5]. In order to compete and differentiate, directional LiFi transmitters must be able to follow their targets and incorporate cost-effective tracking methodologies.

1.1 Scope and Operational Description

The proposed project will establish a baseline for a LiFi system through the implementation of a restorable Representative Stationary Link (RSL). Transmission of power from the laser diode to a photodetector on the opposing module will represent a link connection that could employ methods of optical communication data transfer. The mobility problem inherent to VCSEL-based LiFi systems will be addressed by researching and experimenting with searching and tracking techniques. A well-defined monodirectional optical path will be paired via an initial system alignment to transmit an acceptable amount of power between a stationary base module and a mobile user module across the steradian application range. This initial link will be restored if lost by searching and tracking the mobile user module after movement. The method of searching and tracking, henceforth referred to as Follow and Search Tracking (FAST), is the primary experimental focus of this research. In order to power both modules, separate and optimized power supplies will be implemented on each end. For verification that the optical path is established and maintained, a method of measuring and recording output power will be included on the receiving module. Subsystem documentation and experimental results will be included in the introduction with system level methods and results in the subsequent sections.

The proposed LiFi tracking system is intended to operate in environments demanding high internet and mobility within an enclosed, indoor space. The stationary base module will be optimally located to minimize potential distance to a mobile user module and the number of obstructed pathways. The following experimental constraints to be considered that extend to such a setup are as follows:

- Obstructions in the optical path will not be remedied; however, recognizing that there is no valid path between modules will be considered.

- Before the link is established, the mobile module is stationary and both modules are within each other's operational steradian range.
- System will be able to reestablish a lost link after movement of the mobile user module at a strolling pace within the base module’s operational steradian range.
- Operational design distance will span the average room, with further experimental ranges potentially considered. Corresponding steradian ranges will decrease as distance increases.
- The system will not be designed to operate with external or environmental disturbances (other similar receivers, poor lighting, etc.).
- The VCSEL used to gauge power level availability and maintenance will be a class 3a laser or under, and will operate at a power level and wavelength safe to the human eye following ANSI Z136.8 - Safe Use of Lasers in Research, Development, or Testing.

1.2 Users

Direct users of the proposed system could be researchers either incorporating the tracking function into an existing LiFi system or combining OWC components to build a VCSEL-based LiFi system capable of mobile tracking. From a tracking standpoint, future researchers could explore possible improvements, such as the possibility of path prediction tracking algorithms using AI or machine learning to implement a maintained link during mobile module movement. Such an improvement introduces no additional hardware or cost and would be able to use the proposed system’s architecture as a starting point. Assuming the tracking methods are implemented successfully, the commercial user groups would be those in environments demanding high internet and mobility within an enclosed, indoor space.

1.3 System Overview

The Light Fidelity Tracking System as described in Figure 1.3.1 is composed of a stationary base module and a mobile user module which are each divided into four functional subsystems: Optical Path, Link Communication, Motor Control, and Module Search. The Module Search Subsystems of each module use sensors as a method of feedback related to determining the location of the opposite module and establishing alignment. This sensor data is then sent to the Motor Control Subsystems of the same module. These Motor Control Subsystems use received data to control motors which reorient the Optical Path and Module Search Subsystems accordingly. The Optical Path Subsystem of the base module radiates a laser diode beam at the other module's equivalent subsystem. The received signal on the photodetector of the mobile module is sent to the Link Communication Subsystem's Power Recorder. The Link Communication Subsystem of the mobile module uses this signal to calculate PD power and send this data to the Motor Control Subsystem. The Link Communication Subsystem of the base module controls power to the Optical Path Subsystem's laser diode. The end result of these subsystems is the facilitation of RSL alignment and the implementation of the FAST algorithm as defined above. The developmental methods, results, and conclusions for these subsystems will be further explained in the following sections.

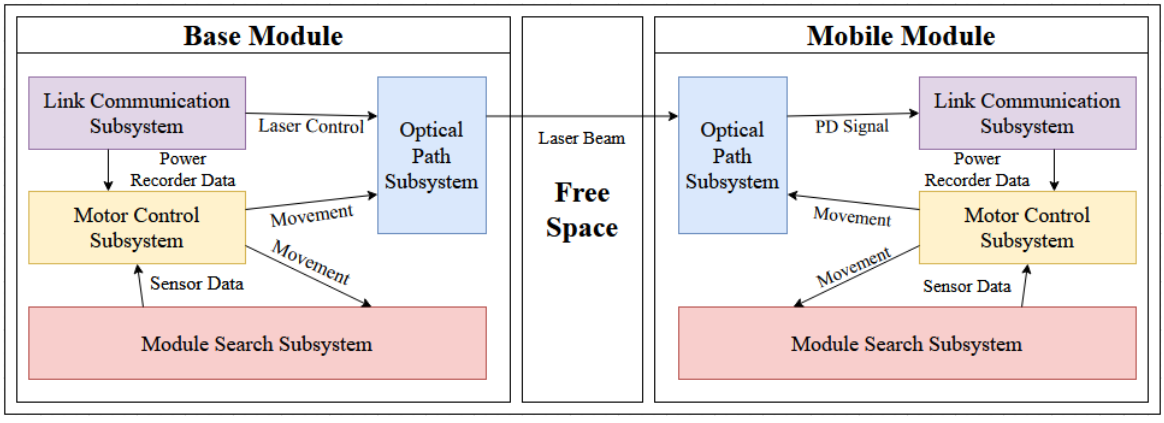

Figure 1.3.1: LiFi Tracking System Functional Block Diagram

1.4 Motor Control Subsystem

The primary role of the motor control subsystem is to allow for the alignment of the stationary base module and mobile module using precise motor motions of each module's rotating and tilting platform. Proper alignment of each module is integral in transmitting power from the VCSEL on one module to the PD on the opposing module. Furthermore, the secondary portion of the motor control subsystem will allow for corrective motor movements to be made to the PD on the X-Y axis; these motions will enhance the amount of power received from the VCSEL on the opposing module.

1.4.1 Motor Control Subsystem Methods

The stationary base module, as shown in Figure 1.4.1, and mobile module must each be capable of performing a wall-to-wall sweep of the given space in search of the opposing module's target. When the target is found, each module must come to a stop and begin coordinate alignment of the VCSEL with the PD. Corrective measures on the PD in the X-Y directions will be taken after initial alignment is achieved.

1.4.1.1 Rotating and Tilting Platform – Hardware

The rotating and tilting platform required the use of highly accurate motor motions in order to allow for the initial alignment of the fairly miniature VCSEL and PD from distances up to ten meters. To enable such motions, stepper motors were used for the rotational and tilting movements. The average stepper motor maintains an angular resolution of 1.8° which would project massive inaccuracies in motion at large distances. In order to limit this inaccuracy, multiple parallel gear combinations were used to shave the angular resolution down. By combining four 40:20 tooth gears in parallel, the angular resolution became 0.1125°. With a substantially lower angular resolution, the rotating and tilting platform may align with minimal

error. Not only this, but lightweight plywood was used to build the platform in order to reduce the weight of the load on the stepper motors; a smaller load allows for less strain on the motors and more precise motion.

Figure 1.4.1: Rotating and Tilting Platform

1.4.1.2 Rotating and Tilting Platform – Software

Using L298N motor drivers, the stepper motors were able to be controlled by the Raspberry Pi microcontroller. The main portion of the rotating and tilting platform software, as displayed in Figure 1.4.2, was responsible for moving towards a (x, y, z) coordinate given by the module search subsystem. As stated above, the platform would stop the sweeping motion once the target was within the frame of reference of the camera. Once the target had been acquired, the platform would align with the coordinate value that was provided.

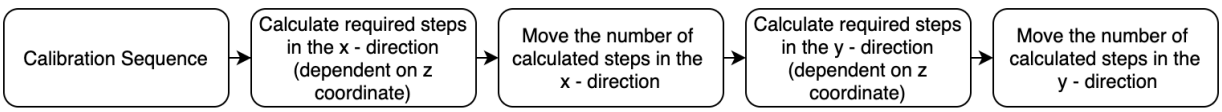

Figure 1.4.2: Positing Towards Given (x, y, z) Coordinate Program

The sweeping portion of the program allowed for the rotating and tilting platform to perform a 180° steradian motion of the given setting to discover the target, as depicted in Figure 1.4.3.

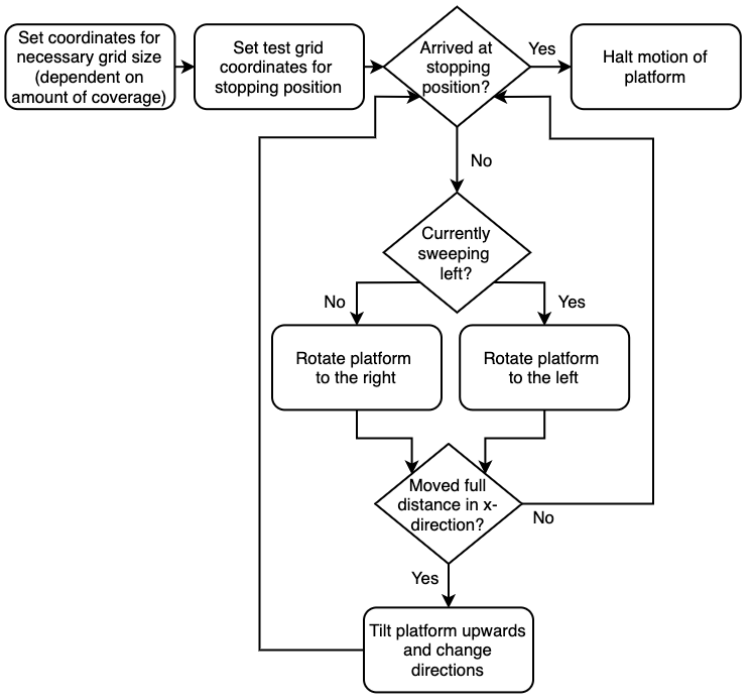

Figure 1.4.3: Steradian Sweep Program

1.4.1.3 X-Y Axis Frame – Hardware

The X-Y axis frame, as pictured in Figure 1.4.4, must be capable of moving the attached PD around an X-Y coordinate system to optimize the power received from the VCSEL. Due to the fact that the frame must be mounted upon the rotating and tilting platform, the frame must be lightweight in order to avoid drastically increasing the load on the stepper motors. By using balsa wood, this goal was achieved. Servo motors were used to permit the necessary motion of the frame because they are not only lightweight but also easily manageable for such simple functionality. The frame is able to move three inches in the y-direction and x-direction to find the point of highest power.

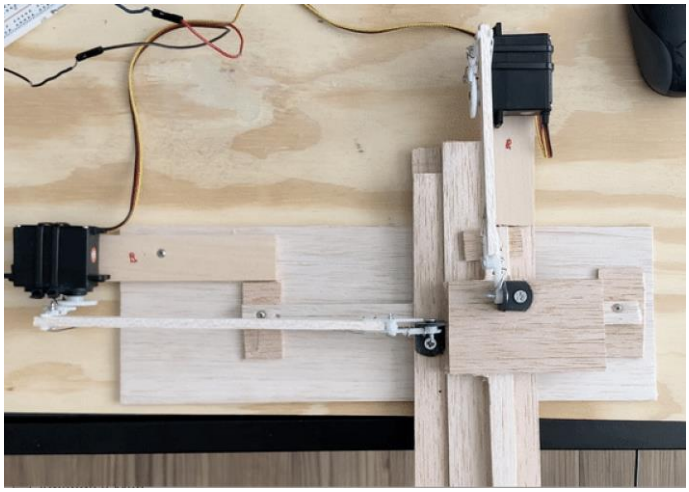

Figure 1.4.4: X-Y Axis Frame

1.4.1.4 X-Y Axis Frame – Software

The primary focus of the X-Y axis frame program, as shown in Figure 1.4.5, was to perform a snake-like motion of the PD until the point of highest power was met. After such a power level was achieved, the system would stop all motion.

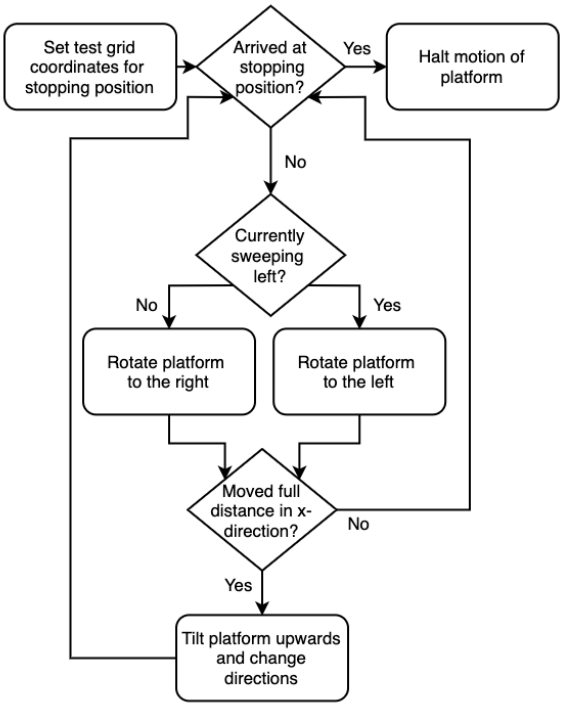

Figure 1.4.5: PD Correction Program

1.4.2 Motor Control Subsystem Results

In order to validate the functionality of the rotating and tilting platform and X-Y axis frame, multiple tests were performed at various distances to ensure consistent accuracy amongst both devices. Strenuous testing on each of the programs resulted in the data depicted below.

1.4.2.1 Rotating and Tilting Platform

The most fundamental test performed on the rotating and tilting platform involved checking the distance between laser beam points on an opposing wall, as displayed in Table 1.4.1. Such a test showed proof that the mechanical system was functioning consistently with the same amount of distance between each laser beam point for a certain distance away from the wall.

Table 1.4.1: Accuracy of Stepper Motors and Gear System

Distance Between Motor Steps		
Distance Away (m)	Theoretical (mm)	Measured (mm)
3.5	6.9	7
5.5	10.8	10 to 17
10	19.7	20 to 26

Secondly, the system was also tested on its ability to stop steradian sweeping at a point in a given coordinate system. Such a test showed the rotating and tilting platform's ability to halt when the target was in the point of view of the camera, as depicted in Table 1.4.2.

Table 1.4.2: Steradian Sweep

Distance from Orginin Laser Beam to Coordinate on 20 by 10 Grid				
	Theoretical y - Distance (mm)	Theoretical x - Distance (mm)	Measured y - Distance (mm)	Measured x - Distance (mm)
(x,y) = (20,10) and (test2, test1) = (5, 1)	28	140	33	127
(x,y) = (20,10) and (test2, test1) = (6, 2)	56	168	45.7	154.9
(x,y) = (20,10) and (test2, test1) = (15, 2)	56	420	58.4	474.9
(x,y) = (20,10) and (test2, test1) = (10, 1)	28	280	48.3	330.2
(x,y) = (20,10) and (test2, test1) = (19, 1)	28	532	30.5	596.9

Lastly, the platform was tested on its ability to move towards a given (x, y, z) coordinate in order to align the VCSEL on one platform with the PD on the other, as shown in Table 1.4.3.

Table 1.4.3: Positioning Towards Given (x, y, z) Coordinate

Theoretical (x, y, z) Coordinates and Measured Distance Away from Theoretical (x, y, z) Coordinates				
Theoretical x - Coordinate (m)	Theoretical y - Coordinate (m)	Theoretical z - Coordinate (m)	Measured Distance Away from Theoretical x - Coordiante (mm)	Measured Distance Away from Theoretical y - Coordinate (mm)
0.101	0.101	3.5	12.7	5.08
0.4	0.4	5.5	0	0
0.101	0.101	5.5	0	3.1
0.07	0.07	10	14.8	5.2
0.05	0.05	10	25.4	12.6
0.025	0.025	10	5	0
0.05	0.1	10	0	15

1.4.2.2 X-Y Axis Frame

The X-Y axis frame was tested on its ability to perform a snake-like motion and halt at a specific coordinate in a defined grid-system, as displayed in Table 1.4.4. Such a motion would allow for correction in the x-direction and y-direction for optimized power receival to the PD.

Table 1.4.4: PD Correction

Distance from Orginin Point to Coordinate on 72 by 52 Grid				
	Theoretical y - Distance (mm)	Theoretical x - Distance (mm)	Measured y - Distance (mm)	Measured x - Distance (mm)
(x,y) = (72, 52) and (test2, test1) = (20, 51)	63.3	8.1	63	7
(x,y) = (72, 52) and (test2, test1) = (71, 51)	63.3	49.4	60	55
(x,y) = (72, 52) and (test2, test1) = (60, 20)	21.1	48.6	18.5	50.2
(x,y) = (72, 52) and (test2, test1) = (50, 31)	42.2	40.5	38	37.1
(x,y) = (72, 52) and (test2, test1) = (60, 51)	63.3	49.4	61.5	52.5

1.4.3 Motor Control Subsystem Optimization

1.4.3.1 Rotating and Tilting Platform – Hardware

Previously, the rotating and tilting platform had required the use of multiple gears and struggled to move back to its original position during the calibration phase of its program. Due to these difficulties, the platform was rebuilt, as pictured in Figure 1.4.6, to correct for these errors and performs nearly identically to the previous system in terms of validation, if not better. In addition, the platform is able to move back to its original location, the design is cleaner, and the overall platform is more reliable with regards to motion.

Figure 1.4.6: Optimized Rotating and Tilting Platform

1.4.4 Motor Control Subsystem Conclusion

The previous and optimized generations of the rotating and tilting platform performed as anticipated. As depicted in the results section, the theoretical values and experimental values for each of the tests regarding the rotating and tilting platform were fairly similar with only minor differences due to error within the stepper motor motions and distance. In addition, the X-Y axis frame also performed as expected with minor error between the experimental and theoretical values. The large acceptance field of the PD, power correction from the X-Y axis frame, and inherent accuracy of the rotating and tilting platform, has allowed error from the overall system to be sufficiently accounted for.

1.5 Module Search Subsystem

The module search subsystem finds an opposite module by scanning a designated space for a defined tracking target, outputting position data necessary to align the system. Primarily, the module search captures an image frame and analyzes contours of similar HSV values to identify a defined tracking target, then uses trigonometric identities to calculate a position in an (x, y, z) coordinate system relative to the center of the frame. This data is passed to the motor control subsystem to make appropriate adjustments for alignment. Additionally, the module search system also looks for a toggling LED in a set position relative to the tracking target and stops searching once seen. The following sections outline in more detail the exact functionality of the system.

1.5.1 Module Search Subsystem Methods and Code Logic

All of the following algorithms were written in Python to run on a Raspberry Pi with a designated camera module. Shown below in Figure 1.5.1 is an overview of the entire code logic, with each step being described in more detail in the following subsections.

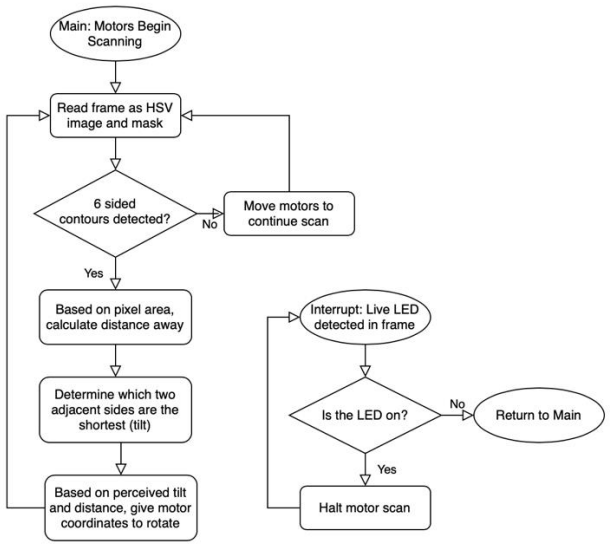

Figure 1.5.1: Overall Module Search Subsystem Code Flow Diagram

1.5.1.1 Finding the Target

The below flowchart outlines the procedure used to convert the captured video frame into the binary image used to identify the tracking target. All colors other than the specific HSV range of the target are masked, and only six-sided contours are identified. From here, the flow diagram pictured in Figure 1.5.2 in section 1.5.1.2 begins.

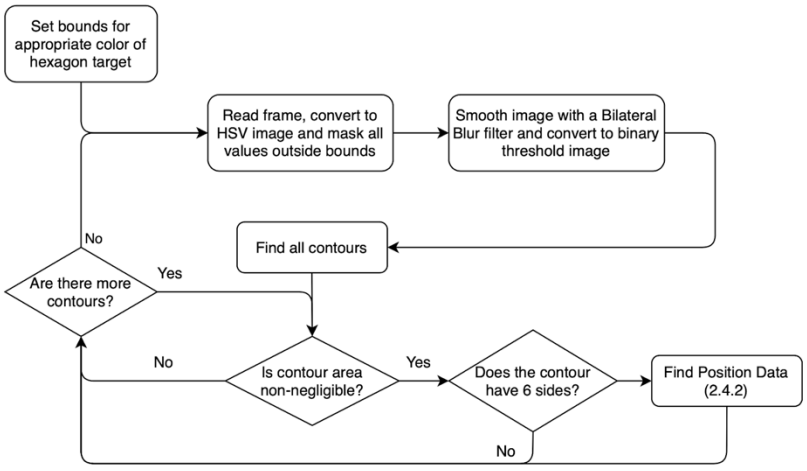

Figure 1.5.2: Target Identification Flowchart

1.5.1.2 Outputting Positional Data

Figure 1.5.3 shows the process flow implemented in code to find position in meters away from the center of the camera. All of the position data is output to the motor control subsystem for physical alignment.

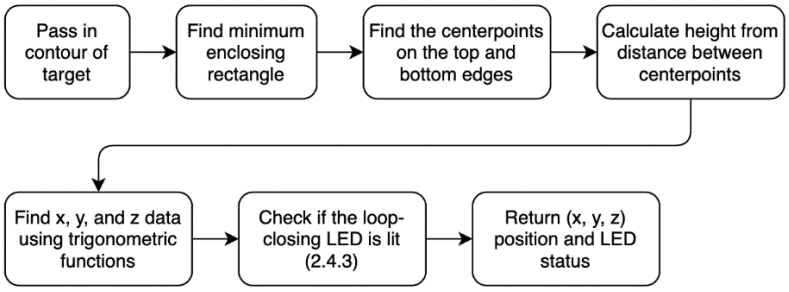

Figure 1.5.3: Positional Locating Code Flowchart

The minimum enclosing rectangle and the centerpoints of the leftmost and rightmost edges are used to find the center pixel of the tracking target, which is used as the reference point when calculating position. Additionally, the distance between these centerpoints gives a width of the target in pixels. Since the width of the target is known, a ratio of pixels per meter can be determined by dividing the measured pixel width by the known width. Using this ratio, similar triangles, and empirical data points, a relationship between the z distance to the camera and the height of the target in pixels can be calculated as follows:

First, the x-direction width of the target is calculated.

$$x2 - x1 = wp = width\ in\ pixels$$

Dividing this pixel width by the known width of the target (4.5 inches = .1143 meters) in gives a ratio of pixels per meter.

$$p = wp/.1143 = pixels\ per\ meter$$

From here, experimental data is required to map a relationship between z and p. For a perfectly centered target, the z distance can be calculated using similar triangles formed by half the width of the target as the opposite side and the distance z as the adjacent side. This is visually represented in figure 1.5.4.

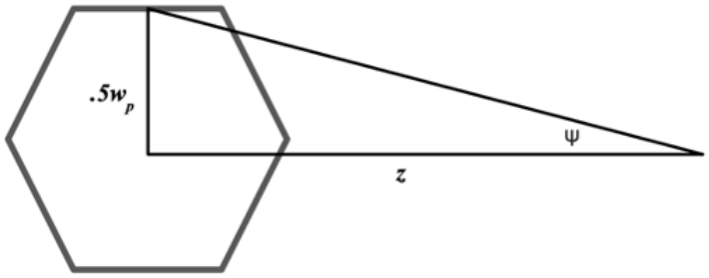

Figure 1.5.4: ψ as visually represented with trigonometry

Thus, let the angle ψ be represented by:

$$\psi = \tan^{-1}(w_p/2z)$$

Then, for any distance z:

$$z = (w_p/2)/\tan\psi$$

Additionally, the offset distance in the horizontal direction from the center of the frame of the camera can be calculated as:

$x = (c_x - c_{hx})/p$, *where* c_x = *center frame x coordinate and* c_{hx} = *center x coordinate of hexagon*

And the offset distance in the vertical direction from the center frame of the camera can be calculated as:

$y = (c_y - c_{hy})/p$, *where* c_y = *center frame y coordinate and* c_{hy} = *center y coordinate of hexagon*

Therefore, using the similar triangles logic shown in figure 1.5.5, an angular offset in the x and y directions can be calculated.

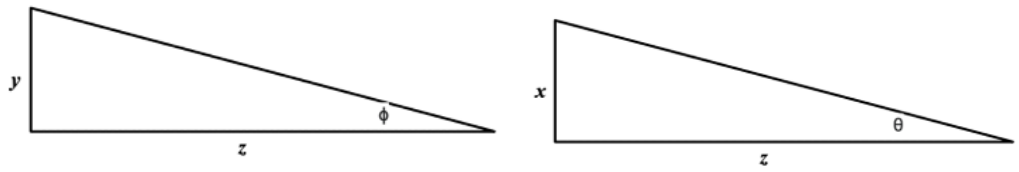

Figure 1.5.5: x and y direction triangles

$\theta = \tan^{-1}(x/z)$ *and* $\phi = \tan^{-1}(y/z)$

Since ψ is needed to calculate z, empirical data was collected to find a relationship between the distance z and the width in pixels. The results of this test are given below in figure 1.5.6.

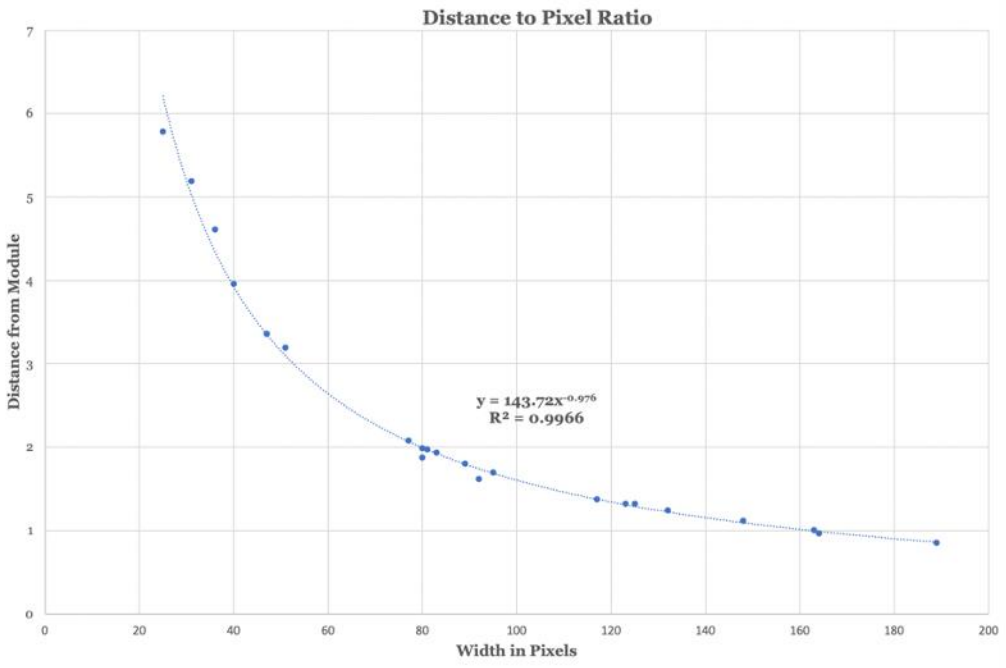

Figure 1.5.6: Empirical Distance to Pixel Relationship

The relationship was shown to be a power function rather than a linear relationship as expected, likely due to the backlit target emitting radial light that constricts in two directions with distance. The code and algorithm were changed to reflect this finding. To find the angular offset in the x and y directions, z is calculated as follows:

$$z = 143.72 * w_p \text{ ^ } -.976$$

1.5.1.3 Closed Loop LED Recognition

Following the calculation of position data, the frame is passed into a new function that masks the image rated for a blue LED. The pixels directly above the tracking target are monitored for significant changes in their HSV value from the expected target color to the bright blue-white color emitted by a blue LED above the tracking target. Masking everything but the area right above the tracking target eliminates the possibility of noisy false positives from overhead or external lighting, and an optical path defined to be unobstructed eliminates the need to account for anything interrupting the view of the target. The following flowchart in Figure 1.5.7 visually outlines the algorithm.

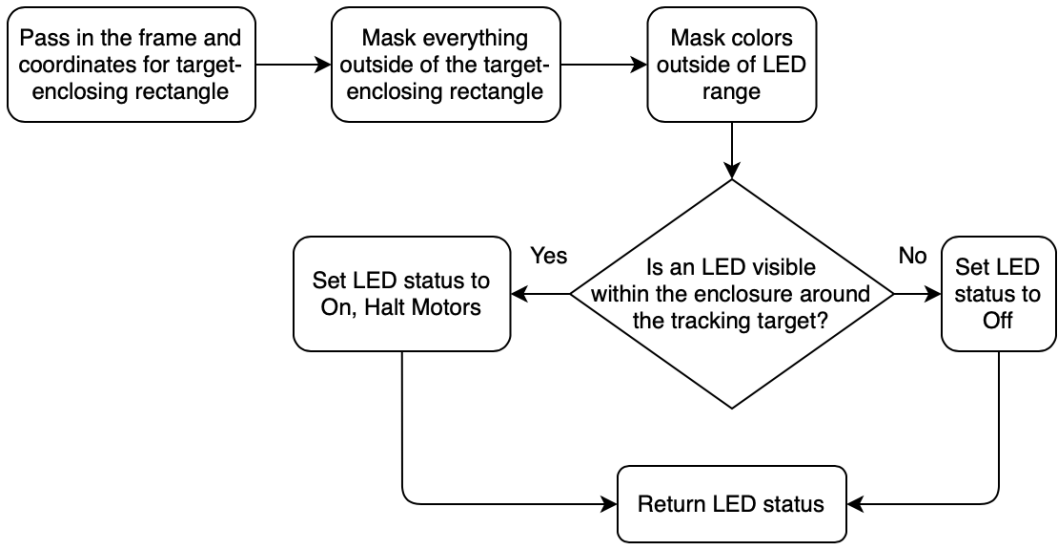

Figure 1.5.7: Closed-Loop Link Communication LED Recognition

1.5.1.4 Tracking Target

To minimize external dependencies on lighting conditions, the tracking target was chosen to be backlit and provide its own light. RGB LEDs are diffused in a hexagonal shape and outlined by a 3D printed frame 4.5” edge to edge and 5.20” vertex to vertex. The LEDs are selected as green because that was experimentally determined to be the brightest color option for these particular bulbs. The frame and LED array are housed in a cardboard box module for both stability and light emission control. Atop this box sits the blue LED necessary for closed loop feedback. These are fed by a constant current source and powered by a 5V power supply. The target is shown below in figure 1.5.8. Two identical targets were produced, one for each module.

Figure 1.5.8: Tracking Target

1.6 Optical Path Subsystem

The optical path subsystem constitutes the physical implementation of the representative stationary link (RSL) between the two modules of the system as well as the interfaces with the bridge that is the link communication subsystem. A representative optical path consisting of a laser diode, photodetector, and other optical path devices will be implemented to balance approximating the optical components of an implemented LiFi system with realistic requirements for facilitating the RSL with the other subsystems. The optical path subsystem includes a major research focus of the project. The laser diode beam characteristics as well as the range of voltage levels read by the photodetector operating circuit corresponding to different scenarios (ambient noise, angled/normal incidence, direct/indirect alignment, etc.) are entirely unknown until the subsystem is implemented. Of course, theory-based calculations and assumptions can provide rough estimates and a method by which to select components; however, the experimental outcome will be the overall limiting factor for much of this systems performance. This includes defining many of the alignment tolerances critical to the other subsystems. Therefore, an additional purpose of this subsystem is to thoroughly define the implemented optical path's power and beam characteristics and the corresponding alignment tolerances demanded.

1.6.1 Optical Path Subsystem Methods

The optical path subsystem constitutes the physical implementation of the representative stationary link (RSL) between the two modules of the system as well as the interfaces with the bridge that is the link communication subsystem. A representative optical path consisting of a laser diode, photodetector, and other optical path devices will be implemented to mimic the optical components of an implemented LiFi system. In order to do so, an effective threshold

power level distinguishable from ambient noise must be incident onto the photodetector after establishing a RSL in order to ensure the hypothetical transmission of data. Also, the components chosen must facilitate the competitive potential of a realistic LiFi system. In addition to potential for data transmission, these components will be chosen and the path will be designed by balancing tradeoffs between power and tracking tolerances resulting from physical component specifications and beam characteristics. Calculations, software simulation, and experimental testing will estimate and validate these requirements. This subsystem also includes the necessary analog circuitry to convert the photodetector current to a measurable voltage. A brief, initial overview of the initial expected design of the optical path is shown in Figure 1.7.1:

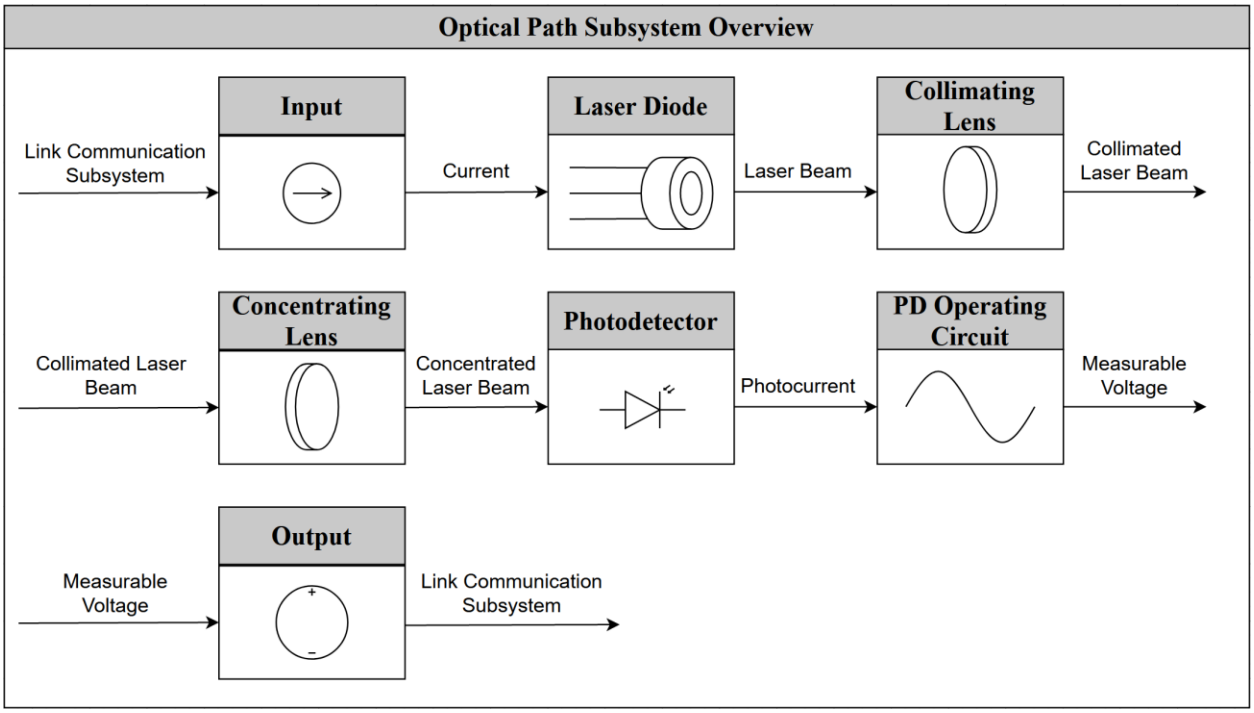

Figure 1.6.1: Initial Design of Optical Path and its Components

1.6.1.1 Laser Diode Selection

In order to start with the optical path design, the preliminary consideration for both data transmission potential and optical path characteristics is the laser diode. As mentioned in the

Introduction section, , the superior device for laser-based data transmission (both for fiber optic cables and Optical Wireless Communications (OWC)) is the Vertical Cavity Surface Emitting Laser (VCSEL) [3]. Specific analysis into the solid-state physics, semiconductor design, and other such laser theory will be left out of this report for the sake of brevity. However, the main takeaway, which is accepted by academia involved in OWC, is that the VCSEL is the superior laser diode for OWC and LiFi applications due to its exceptional potential for relatively large bandwidth and high modulation speeds [3]. These VCSEL diodes are typically in the Near-Infrared (NIR) wavelength range and are non-visible. Moreover, to fit the intended application, the VCSEL must be at a safe power level for humans. Accepting these facts and moving forward with the component selection process, the first step is understanding the safety standards commonly associated with laser diodes.

After taking and passing the TAMU General Laser Safety Training Course, it became clear that the ANSI Z136.8 - Safe Use of Lasers in Research, Development, or Testing and the Texas Department of State Health Services, Radiation Control Program 25 TAC 289.301 Registration and Radiation Safety Requirements for Lasers and Intense-Pulsed Light Therapy based on this standard must be followed [6]. Also, IEEE standards for OWC communications exist [7]. According to the Laser Institute of America's published and free to access information based on the ANSI standards, lasers of Class 3R (aka 3A) and below satisfy the desired safety requirements for the proposed application [8]. With this information, commercially available VCSEL diodes that fit these specifications were researched and compared. As it turns out, there were very few viable options. Table 1.6.1 below shows the two predominant VCSEL selections from reputable manufacturers and electronics distributors:

Table 1.6.1: VCSEL Decision Matrix

Metric	Thorlabs	TT Electronics	Desired
Wavelength	850 nm	850 nm	Near infrared, non-visible >700nm
Optical Power	2 mW	1.5 mW	Less than 5 mW (safety)
Operating Current	4 mA	7 mA	Less than 10 mA (Pi Compatibility)
Operating Voltage	2.2 V	2.2 V	Less than 2.5 V (Pi Compatibility)
Laser Class	1M	1M	Below Class IIIb (3b)
Beam Divergence	12°	24°	Reasonable for Collimation (less than 30°)
Package	T0-46	T0-46	Compatible with Optical Mounts from Lab
Price	$150	$15.10	Need to buy two, must be reasonable price

Note: the specifications included in Table 1.6.1 were derived from the datasheets of the Thorlabs L850VH1 and the TT Electronics OPV310 VCSEL diodes. The above metrics for comparison were derived from the laser safety classes, current and voltage limits for compatibility with the Raspberry Pi (from Raspberry Pi Datasheets), and compatibility with existing hardware in the research lab (located in the Wisenbaker Engineering Building). Since both diodes satisfied the desired metrics, the cheaper option was chosen as the slight decline in specification quality was determined to be negligible compared to the increase in price. Therefore, the TT Electronics OPV310 VCSEL diode was chosen, and its relevant specifications are included in Table 1.6.1. Other characteristics of this diode from its datasheet include that it contains a flat lens, was designed to be utilized for air transmission of data, and it was designed for applications where low current is required with high on-axis optical power. These characteristics are all highly desired for a LiFi system as well as for favorable conditions relating to alignment tolerances. It is important to note that the included flat lens will not result in a collimated output beam and the beam divergence angle of 24° will not be sufficient for the

application range of one to ten meters. Therefore, a collimating lens will need to be implemented as expected in Figure 1.6.1. Moreover, choosing a specific photodiode and concentrating lens (if necessary) will be difficult unless the beam characteristics can be estimated across the application range. To do this, some preliminary choices for photodiodes are needed and can be incorporated with Gaussian beam and geometric optics calculations to predict optical path performance and choose finalized components.

1.6.1.2 Preliminary Photodiode Component Selection

Preferred metrics for photodiodes were similarly derived from both necessary LiFi characteristics as well as preferred specifications for optimal alignment tolerances. However, there was a significantly larger amount of commercially available photodiodes compared to the few VCSEL options. A suitable option, the Thorlabs FDS100, was chosen for its desirable characteristics which fit the following metrics:

- Wavelength Range: a property of the photodiode material related to the semiconductor bandgap and must include the VCSEL wavelength of 850 nanometers.
- Responsivity: the amount of produced photocurrent dependent on incident optical power and wavelength for a photodiode. This is the most critical specification to ensure sufficient power conversion efficiency as well as enabling the ability to distinguish the VCSEL beam from ambient noise.
- Active area: the size of the detector which can capture the incident beam and convert the detected incident irradiance into photocurrent.
- Rise Time: the speed at which photocurrent is produced relative to changes in the incident optical power.

Each of these specifications is of significant importance for various reasons, and it was thus difficult to choose between the many options of photodiodes which all have relative benefits. According to the Thorlabs FDS100 data sheet, the FDS100 has a wavelength range of 350 – 1100 nm, a responsivity of 0.55 A/W, an active area of 13 mm^2, and a rise time of 10 ns. For its relatively low price, these photodiode specifications seemed suitable for the intended application due to relative comparison with other options. To confirm the suitability of the Thorlabs FDS100 photodiode, a collimating lens must be chosen and a qualified estimate of beam characteristics across the application range of 1 to 10 meters must be attained. Therefore, the next step in the optical design process is to perform geometric optics and Gaussian beam calculations to attain this estimate.

1.6.1.3 Geometric Optics and Gaussian Beam Theory

In order to approximate the behavior of the chosen VCSEL's beam across the application range of 1 – 10 meters, it is a safe starting approximation to assume the beam is Gaussian and utilize Gaussian beam theory for calculation purposes [9]. That being said, experimental results for the VCSEL will likely have some deviation from Gaussian beam theory, but it provides a realistic starting point for choosing optical components and estimating beam characteristics. Without going into the specifics of Gaussian beam theory, the equations used in the following calculations can be summarized as follows using the results depicted in Chapter 13 of Hecht's Optics – 5th edition Textbook [9]:

$$w(z) = w_0\left[1 + \left(\frac{\lambda z}{\pi w_0}\right)^2\right]^{\frac{1}{2}}$$

$$\Theta = \frac{2\lambda}{\pi w_0}$$

In these equations, w_0 refers to the laser beam waist, w(z) refers to the beam radius at a distance z, λ is the free space wavelength of the VCSEL beam, and Θ is the full beam divergence angle. For the following calculations, the beam waist will be defined as the radius of the beam as it exits the collimating lens.

In addition to Gaussian beam theory, incorporating the collimating lens into the calculations requires some geometric optics equations which follow the paraxial approximation. To simplify explaining the theory behind this topic, summarized results included in Thorlabs' Collimation Tutorial provide a bare minimum starting point. These equations are simplified to aide in choosing a lens focal length based on a chosen laser diode and a desired output collimated beam diameter [10]:

$$f = \frac{\frac{\emptyset_\perp}{2}}{tan\frac{\theta_\perp}{2}}$$

$$NA_{diode} = n * sin\frac{\theta}{2}$$

In these equations, f is the ideal focal length of the collimating lens, $\emptyset_\perp$ is the collimated beam diameter, $\theta_\perp$ is the uncollimated beam divergence angle, and NA is the numerical aperture. In order to use these equations to choose a collimating lens, a design output collimated beam diameter must be chosen. Note that since the VCSEL diode is circularly polarized, the perpendicular and parallel polarized beam diameters will be equivalent. This quantity has a profound effect on the beam characteristics in the application range. A smaller output beam

diameter will have a larger output divergence angle, whereas a larger output beam diameter will have a smaller output divergence angle. From this relationship, an optimized value can be calculated and visualized in a plot when designed for the maximum range of ten meters. Using these equations and this output beam diameter, the size of the beam at ten meters and the corresponding percentage of the beam incident on a detector area can be calculated. To perform this, the detector areas of the Thorlabs FDS100 photodiode chosen in the previous section and another example photodiode with a smaller area (OSRAM Opto Semiconductors Inc. BPX 61) were used. The result was Figure 1.6.2 as seen below which was created using MATLAB. The plot depicts the output collimated beam diameter vs the percent of the beam incident on each photodetector at ten meters. The Thorlabs FDS100 model has a side length of 3.6 mm while the OSRAM Opto Semiconductors Inc. BPX 61 has a side length of 2.65 mm. Each of the photodiodes had an optimum output collimated beam diameter of 3.29 mm which corresponds to a lens focal length of 7.74 mm, showing that this optimum value is independent of detector area. However, one can note that 75% of the beam is incident on the active area of the Thorlabs FDS100 model compared to 41.3% for the OSRAM Opto Semiconductors BPX 61 model. This relatively significant difference related to active area size makes the Thorlabs FDS100 option the better photodiode choice. However, at this point, it is unclear whether or not a concentrating lens is needed to improve this value. Proceeding with choosing a collimating lens will make this clear.

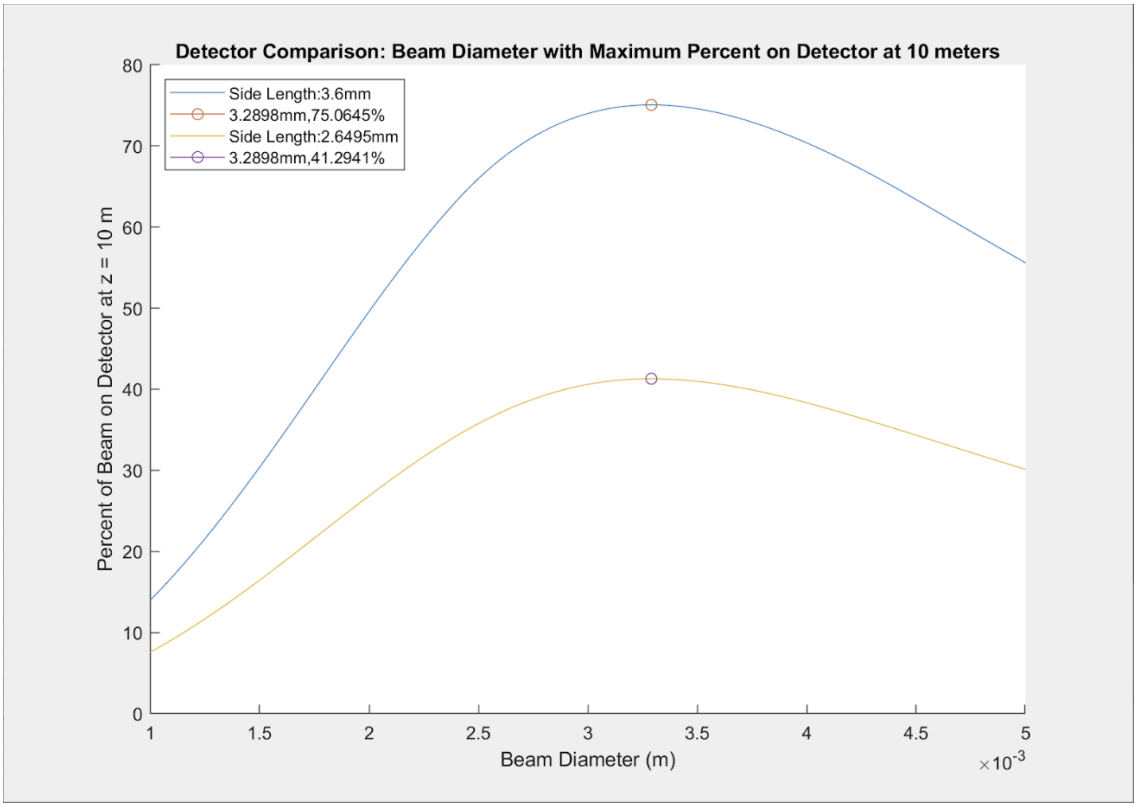

Figure 1.6.2: Optimized Output Collimated Beam Diameter

1.6.1.4 Collimating Lens Component Selection

With a focal length target value of 7.74 mm, actual available lens specifications must be chosen. Due to compatibility with existing optical mounts in the research lab which will ultimately reduce overall price, Thorlabs was chosen as the preferred lens manufacturer. From their lens options, aspheric lenses were chosen for collimation purposes due to their ability to reduce spherical aberrations and increase collimation performance relative to other lens types. The numerous focal lengths closest to 7.74 mm were compared by producing a plot showing percent of beam incident on the Thorlabs FDS100 photodiode active area across distance for the application range as shown in Figure 1.6.3. As expected, the best performing focal lengths corresponded to the values closest to the optimized focal length (7.5 mm, 8.0 mm, 6.2 mm, and 6.24 mm).

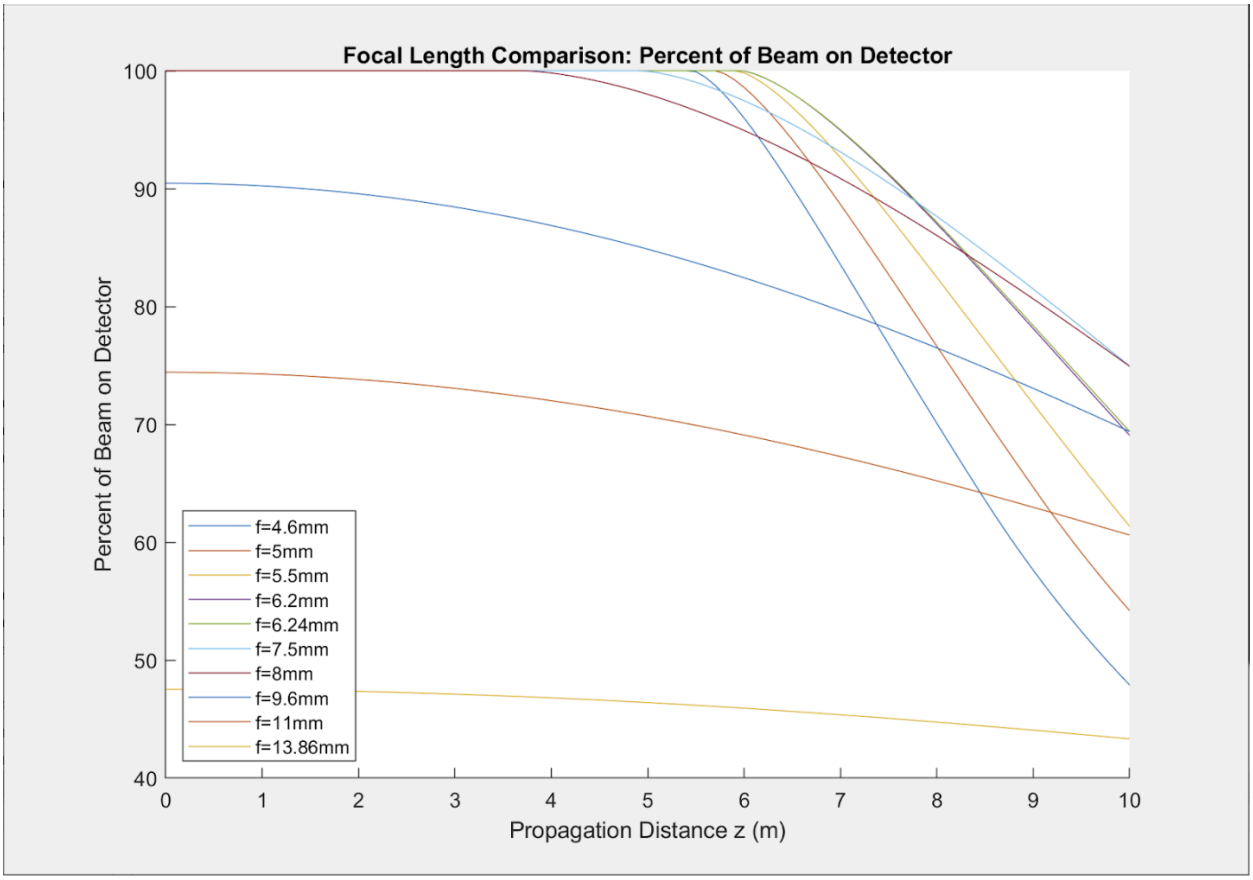

Figure 1.6.3: Focal Length Comparison – Percent of Beam on Detector

Narrowing the options down to these values, there were only a few remaining aspheric lens options on Thorlabs. However, only a few of these mounted aspheric lenses were compatible with the expensive optical lens tube mounts in the lab, including the best option - the A375TM-B with a focal length of 7.5 mm. This lens also has an anti-reflective coating for the VCSEL wavelength as well as the required numerical aperture and lens diameter. Although it was the most expensive option, lens tube mounts, lens tubes, and spanner wrenches for the other options would total over $100 additional dollars. These components are necessary for precise experimental optics measurements and will also be incorporated into the final system. With all this taken into account, the A375TM-B was chosen as the collimating lens for the optical path. With the collimating lens decided, further calculations can be conducted evaluating power levels

and beam characteristics across the application range. Also, the need for a concentrating lens can be decided.

1.6.1.5 Beam Characteristics Across Application Range with Collimating Lens

Using the output beam diameter corresponding to the focal length of the chosen collimating lens, further Gaussian beam calculations can be performed which will yield more insight into the beam characteristics across the application range. The ultimate deciding factors for determining if these beam characteristics are sufficient for the system and whether or not a concentrating lens is needed relate to tracking the power conversion through the optical path as well as estimating the physical dimensions of the beam. Using the component specifications for the chosen VCSEL and photodiode along with Gaussian beam theory, these calculations can be performed. For power conversion through the optical path, the VCSEL drive current decides the output optical irradiance of the beam which is distance dependent. The amount of this beam incident on the photodiode active area determines the incident optical power which leads to a specific photocurrent produced by the photodiode determined by its responsivity specification at the VCSEL wavelength. These conversions and the beam radius as a function of distance are summarized and labeled in Figures 1.6.4 – 1.6.8:

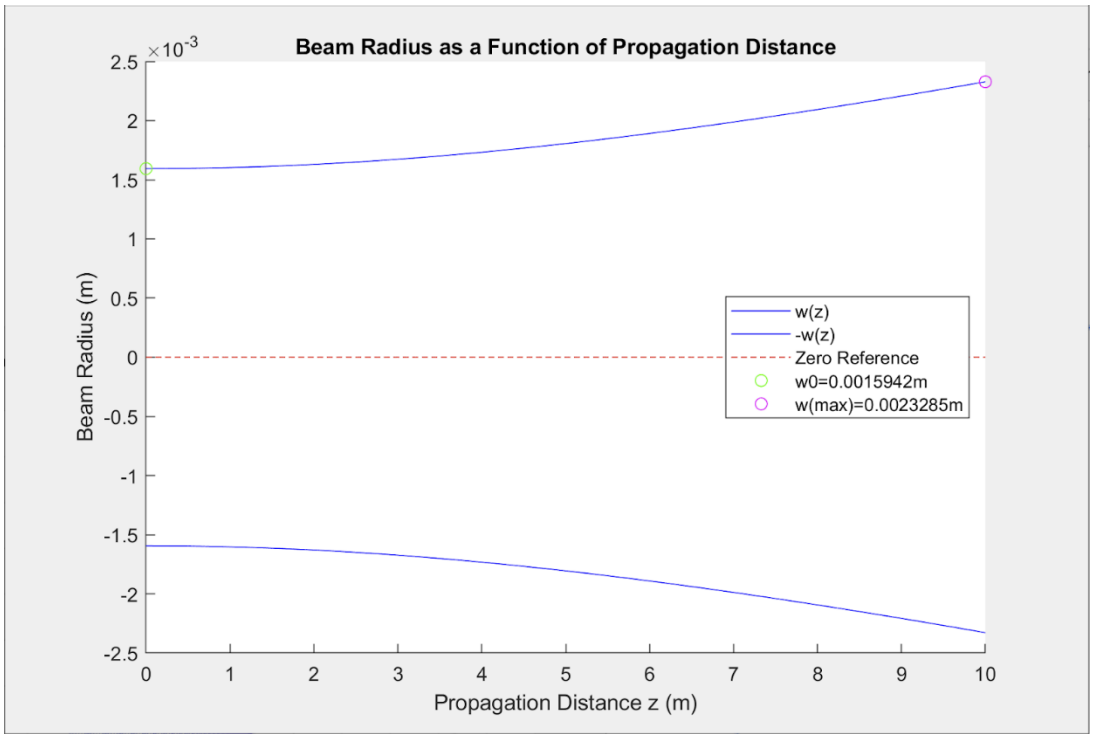

Figure 1.6.4: Beam Radius as a Function of Propagation Distance

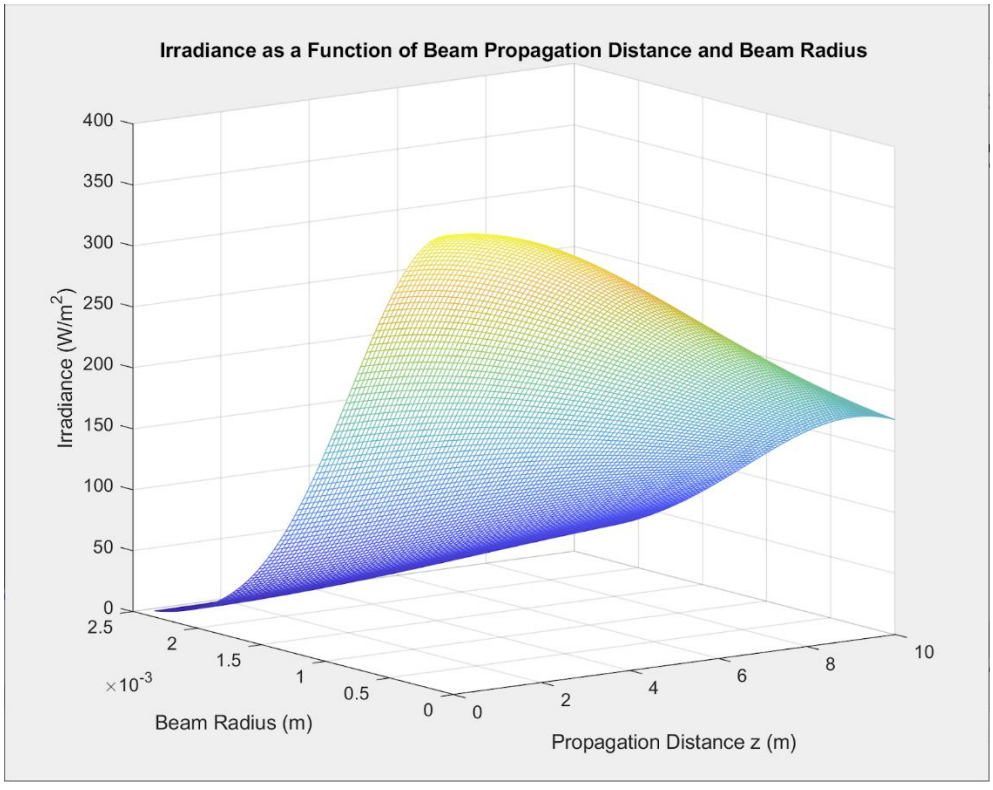

Figure 1.6.5: Irradiance as a Function of Beam Radius and Propagation Distance

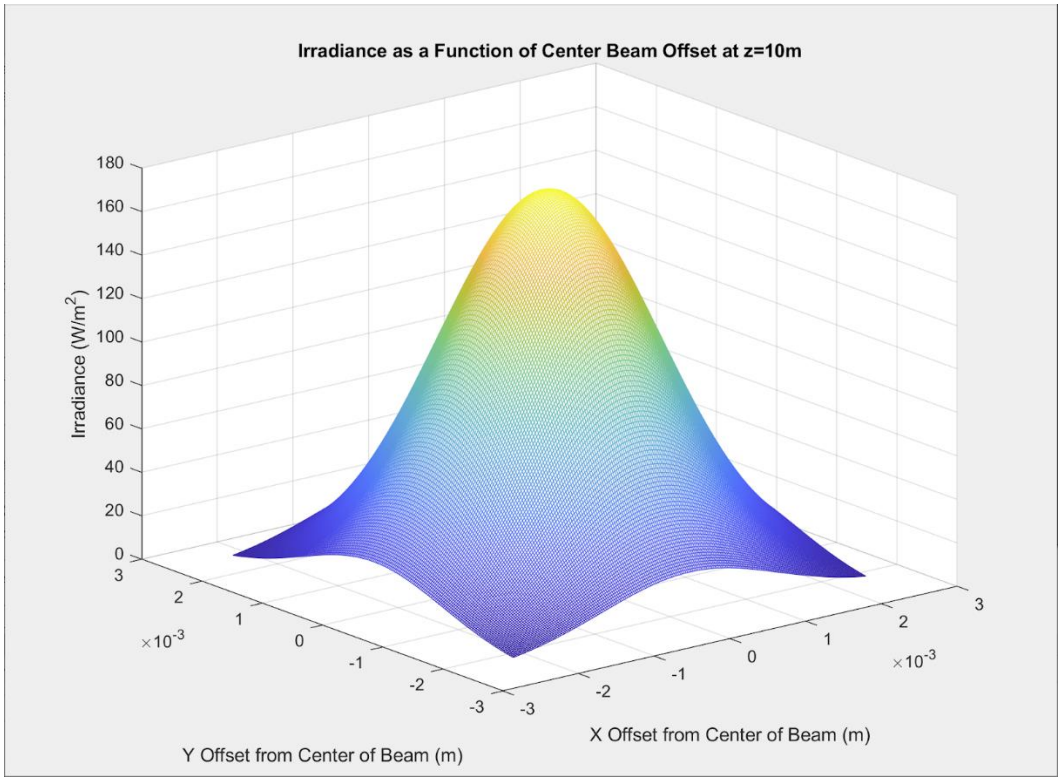

Figure 1.6.6: Irradiance as a Function of Offset from Beam Center at 10 meters

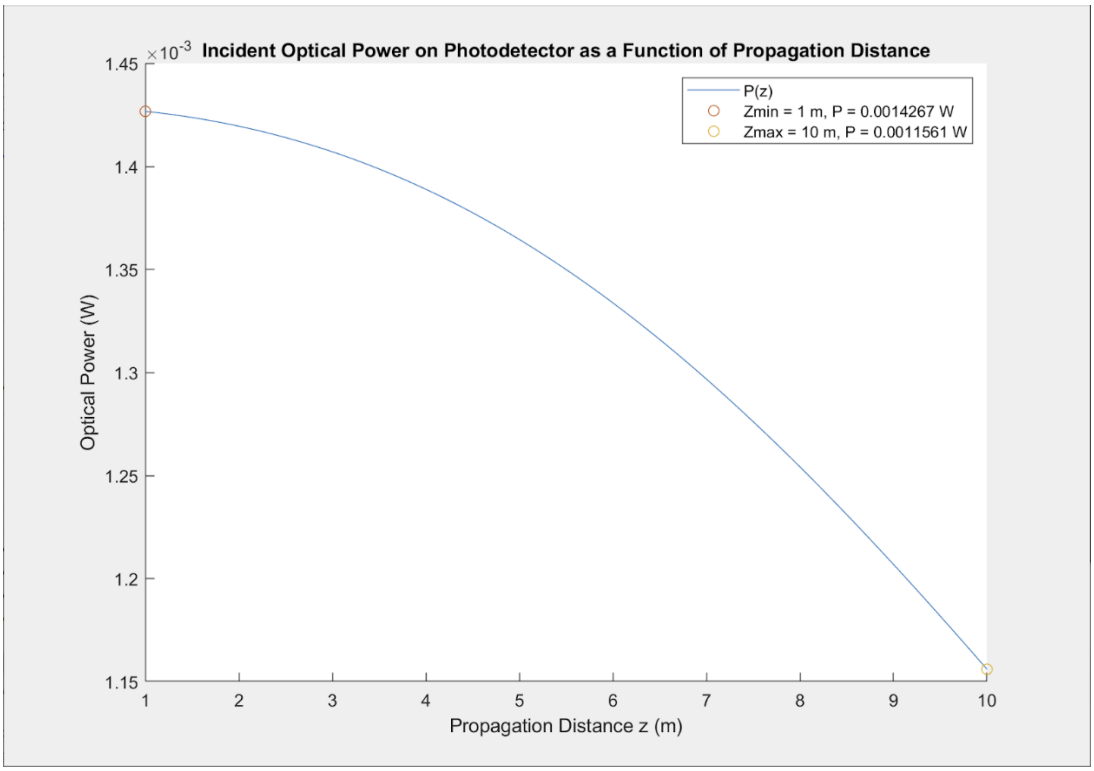

Figure 1.6.7: Incident Optical Power on Photodetector vs Propagation Distance

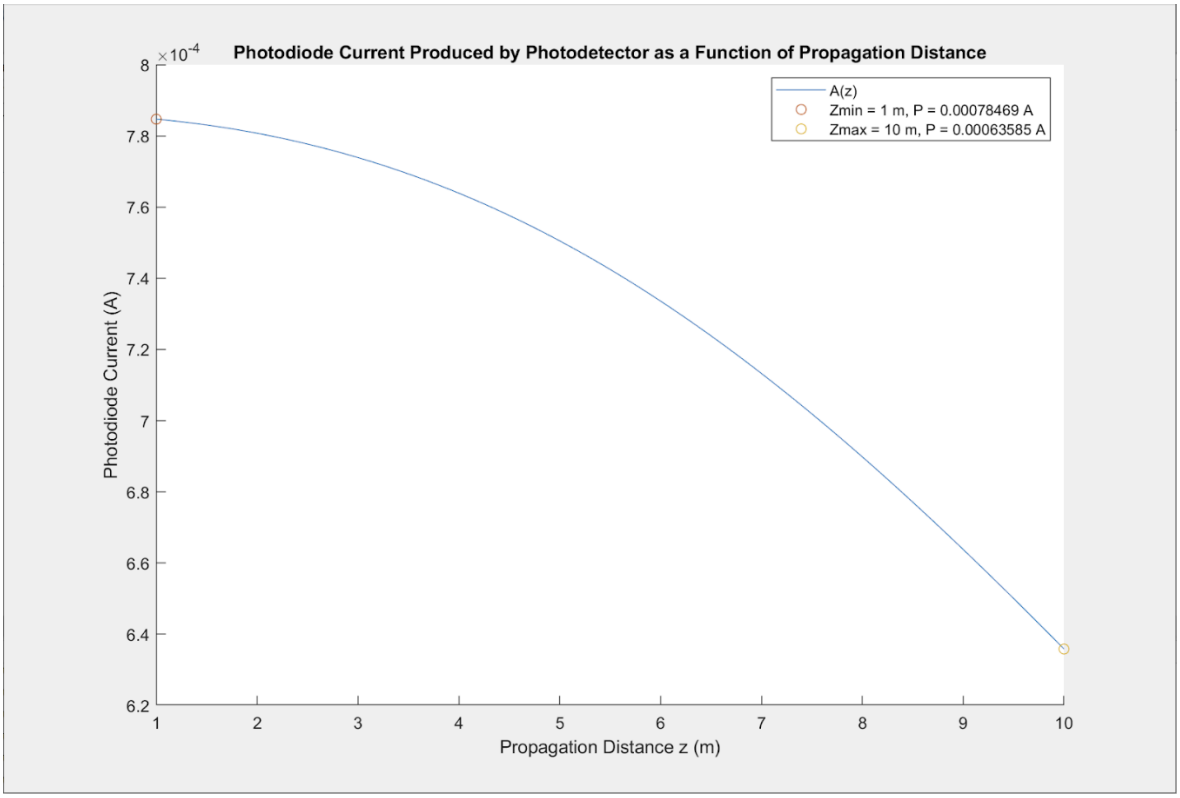

Figure 1.6.8: Photodiode Current vs Propagation Distance

Several important conclusions and assumptions can be drawn from these figures. To briefly summarize, Figure 1.6.4 shows that the beam radius is expected to go from 1.59 mm at the collimating lens to 2.33 mm at a distance of 10 meters. These results are exceptional although experimentally unlikely. However, with such good results, experimental errors will likely still produce desirable results. Similarly, Figure 1.6.8 shows a range of photocurrent from 636 μA to 785 μA depending on propagation distance. With these values produced by a simple responsivity calculation, a load resistor of 1000 Ω in a photodetector operating circuit would produce a measurable voltage in the hundreds of millivolts without any amplification or reverse bias. These results show that this collimating lens provides exceptional theoretical results that permit a wide margin of experimental error to occur before undesirable results are produced. As a result, it can

be determined that no concentrating lens is needed unless experimental results eventually show otherwise.

With the VCSEL, photodiode (PD), and concentrating lens designed, the only design component left is the PD Operating Circuit. At this point, the Link Communication Subsystem's analog to digital converter (ADC) is chosen and its input voltage ranges are known. The PD operating circuit must be designed to produce voltages within the range of zero to five volts with incident beam values being distinguishable from noise in that range. A possible PD operating circuit design utilizes a Transimpedance Amplifier (TIA) to introduce gain, reduce noise, and maximize bandwidth for the photodetector. Such a design will be needed if a simple PD operating circuit design does not produce sufficient results. This cannot be confirmed until the optical components are ordered and received. Also, testing to ensure whether or not a simple PD operating circuit will suffice compared to a TIA cannot be completed until the VCSEL is properly collimated and aligned with a lens in a lens tube.

1.6.1.6 Lab Test Equipment Overview

Before further discussion into the optical design process occurs, a brief figure depicting critical lab test equipment will be given in Figure 1.6.9. In addition to the depicted lab test equipment, the National Instruments Analog Discovery Device 2 (AD2) was used along with a myriad of other equipment including infrared sensor cards, optomechanical mounts, lens tubes, optical tables, and test laser diodes.

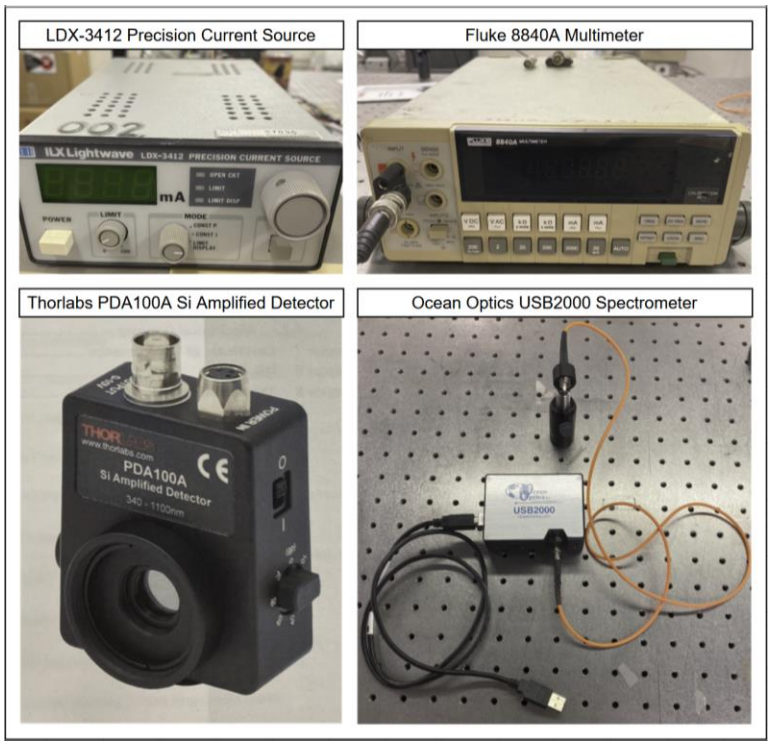

Figure 1.6.9: Lab Test Equipment

1.6.1.7 VCSEL Characterization and Collimation Process

With the OPV310 VCSEL diode received, the first steps include mounting the diode in a lens tube, characterizing its wavelength, and collimating its output beam with the collimating lens. Figure 1.6.10 depicts the output of the USB2000 Spectrometer and its corresponding Oceanview software for the VCSEL at a drive current of the recommended 7 mA produced by the precision current source in Figure 1.6.9. The resulting peak wavelength was 849.6 nm with a significant band from 844.9 nm - 850.5 nm. These values closely follow the datasheet and confirm that this physical VCSEL will behave according to the previous theoretical calculations in terms of wavelength. Figure 1.6.11 depicts the physical mounting of the VCSEL in a lens tube (left), the physical mounting of an additional lens tube with the collimating lens (middle), and the spanner wrenches used during the collimation process (right). By using this specific hardware set up, the VCSEL diode and collimating lens are perfectly aligned along the same optical axis.

Also, the spanner wrench permits fine-tuned adjustments and measurements to get the collimating lens close to the focal length away from the VCSEL diode.

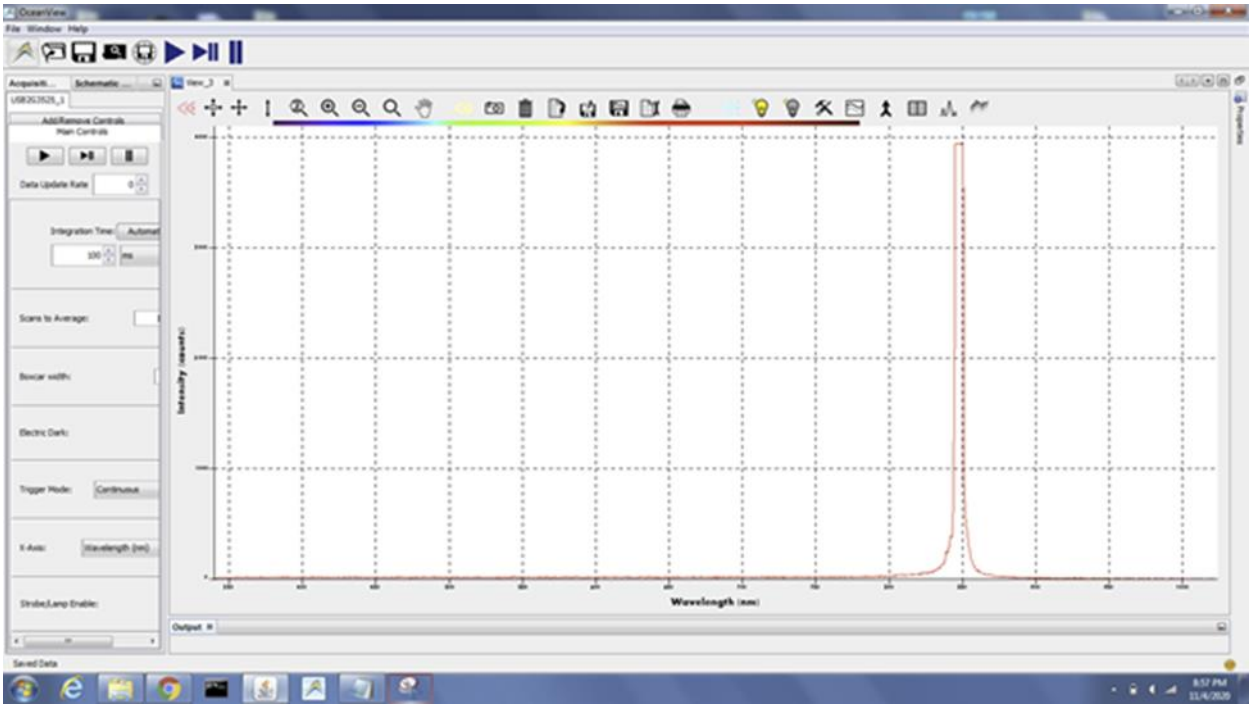

Figure 1.6.10: VCSEL Spectrometer Results

Figure 1.6.11: VCSEL and Collimating Lens Hardware Setup

The collimating process is further depicted in Figure 1.6.12. The uncollimated diode is shown on the left with a diffused, barely visible beam on the infrared sensor card. The middle photo depicts the collimating lens being added and adjusted until a compact dot was recognized. Finally, the spanner wrench was used with the Lab PD connected to the multimeter in the right photo to fine tune the collimating lens position until a maximum voltage was read at 36” (shown in the bottom table). Due to physical limitations of the lens tube and human error with using the spanner wrench for adjustments, this value was brought as close as possible to its optimal value. This concluded the collimation process and resulted in the beam spots on the infrared sensor card at one meter and ten meters depicted in Figure 1.6.13.

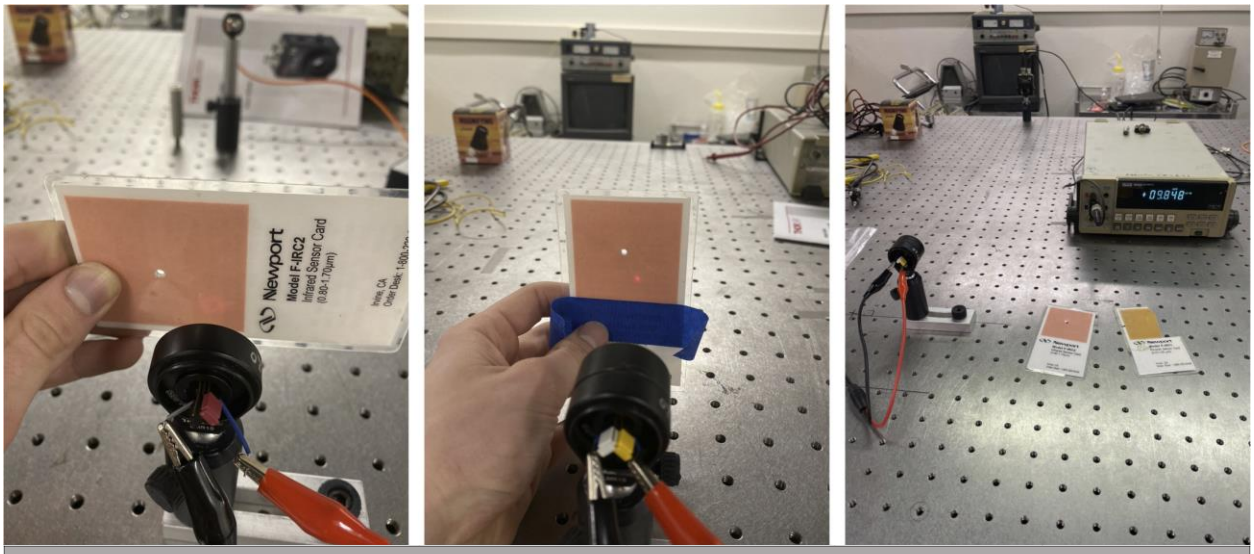

VCSEL Collimation - Photodetector Adjustment

Distance (in)	Drive Current (mA)	PD Aperture	PD Output Voltage (V)		
			Ambient Noise	Initial	Max
36	7	S1LM05	0.009856	1.8363	1.924

Figure 1.6.12: VCSEL Collimation Process

Figure 1.6.13: VCSEL Beam Patterns at One and Ten Meters Respectively

Note: the beam pattern at ten meters is larger than expected and shows an interesting irradiance distribution. This signifies some multimode behavior in the VCSEL diode that will likely lead to some differences in the experimental results compared to what was expected with Gaussian beam theory. Further analysis into this beam pattern will be discussed after validation.

1.6.1.8 PD Operating Circuit Design

With the VCSEL collimated and the Thorlabs FDS100 PD received, the PD operating circuit will be designed. As mentioned before, it must produce measurable voltages within the range of zero to five volts with beam measurements distinguishable from ambient noise. The first PD operating circuit that will be designed, breadboarded, and evaluated will be the Thorlabs recommended circuit included in the FDS100 datasheet. Provided this design is sufficient, it is favorable due to its simplicity and its ability for the FDS100 to operate in both the photovoltaic and photoconductive modes. A brief summary of these modes notes that the photovoltaic (PV) mode produces less dark current which results in more consistent but smaller magnitudes of

voltages read across the load resistor. Alternatively, the photoconductive (PC) mode applies a reverse bias which increases the depletion region, reduces junction capacitance thereby increasing speed, and has an increasingly larger responsivity as the reverse bias increases. At this point, it is difficult to note which mode would be better; however, both are possible (a reverse bias of 5 V can be applied by the Raspberry Pi supply line) and can be evaluated with this circuit. Since the reverse bias would have to be constant and set by the Raspberry Pi to be 5 volts, the only design component of this circuit would be the load resistor which sets the magnitude of the range of measured voltages. Using a test laser diode to produce a wide range of optical power, the AD2, and the multimeter as shown in Figure 1.6.14 (left), several load resistor values were tested with a breadboard and the results for the best load resistor value for the application are summarized in Table 1.6.2.

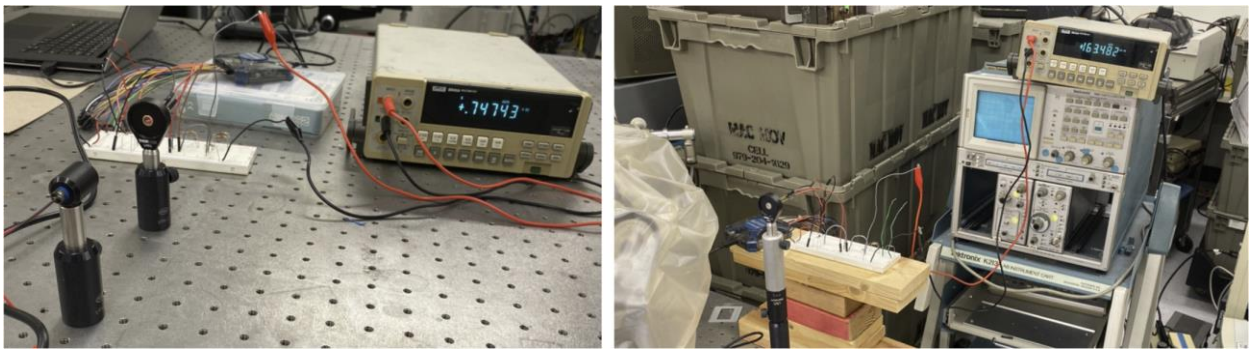

Figure 1.6.14: Breadboard Load Resistor Experimental Setup

Table 1.6.2: Load Resistor Optimized Value

Load Resistor (Ω)	Measured Resistor Value (Ω)	Test Diode Drive Current (mA)	Direct Incidence Voltage (V)	Ambient Noise (mV)
100	101.6	10	0.00047	0.21
		20	0.0371	
		30	0.0766	
1000	982	10	0.0049	2.41
		20	0.322	
		30	0.747	
5000	4930	10	0.0221	10.6
		20	1.73	
		30	3.69	
10000	9790	10	0.0437	21.1
		20	3.35	
		30	4.95	
20000	19740	10	0.0871	43.4
		20	5.15	
		30	5.22	

Therefore, as depicted in Table 1.6.2, the optimal load resistor value is 10 kΩ. A quick test of this breadboarded circuit with the OPV310 VCSEL diode at 10 meters as depicted in Figure 1.6.14 (right) showed a value of about 160 mV with beam incidence compared to 20 mV for ambient noise. Evidently, the magnitude of the measured voltage at 10 meters was within the desired range and the beam measurement was distinguishable from ambient noise. Therefore, the PD operating circuit design is seemingly sufficient to be paired with the FDS100 PD and the chosen ADC of the link communication subsystem. Sophisticated designs like a TIA may not be necessary. With this confirmation, the PD operating circuit with this load resistor was soldered onto a protoboard as shown in Figure 1.6.15. At this point, the optical path subsystem is fully designed and implemented. Extensive and exhaustive validation will have to be performed to verify that the subsystem works as intended and accomplishes its desired goals.

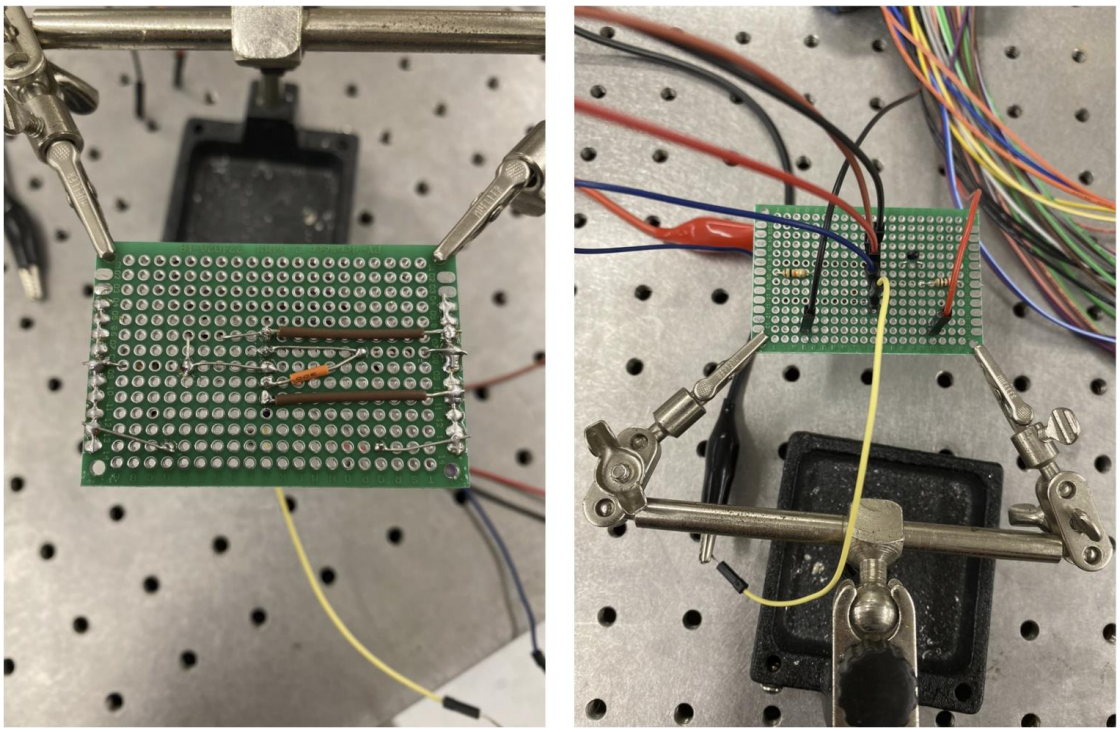

Figure 1.6.15: PD Operating Circuit Implemented on Protoboard

1.6.1.9 Optical Path Subsystem Validation Plan

The interfaces of the optical path subsystem with the other subsystems pictured in Figure 1.6.16 and the necessities behind defining the experimental beam characteristics inspired the following experimental set ups to validate the subsystem. These include noise, distance, alignment, and angular measurements as well as comparisons with a Lab PD and between different drive currents and PD modes.

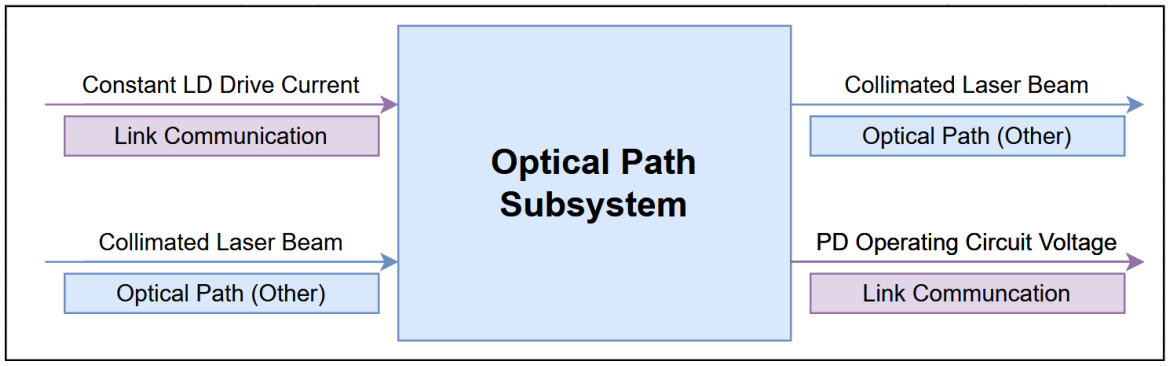

Figure 1.6.16: Optical Path Subsystem Interfaces

1.6.1.10 Ambient Noise Measurements and Validation

In order to properly detect the opposite module's beam, distinguish it from ambient noise, and have the potential for data transmission, the VCSEL diode and PD operating circuit combination must produce measurable voltages that are noticeably higher in magnitude with beam incidence than with ambient noise across the entire application range of zero to ten meters. This can be validated through a combination of ambient noise measurements for different environmental conditions for the intended application space and distance measurements focused on beam incidence. The first experimental validation will therefore be using the PD operating circuit to analyze noise values for different environmental conditions. This will be compared to values in an identical set up with the Lab PD (Thorlabs PDA100A Si Amplified Detector) to verify realistic values and also give insight into the PD operating circuits performance relative to a lab test quality photodetector. The experimental set up is depicted in Figure 1.6.17.

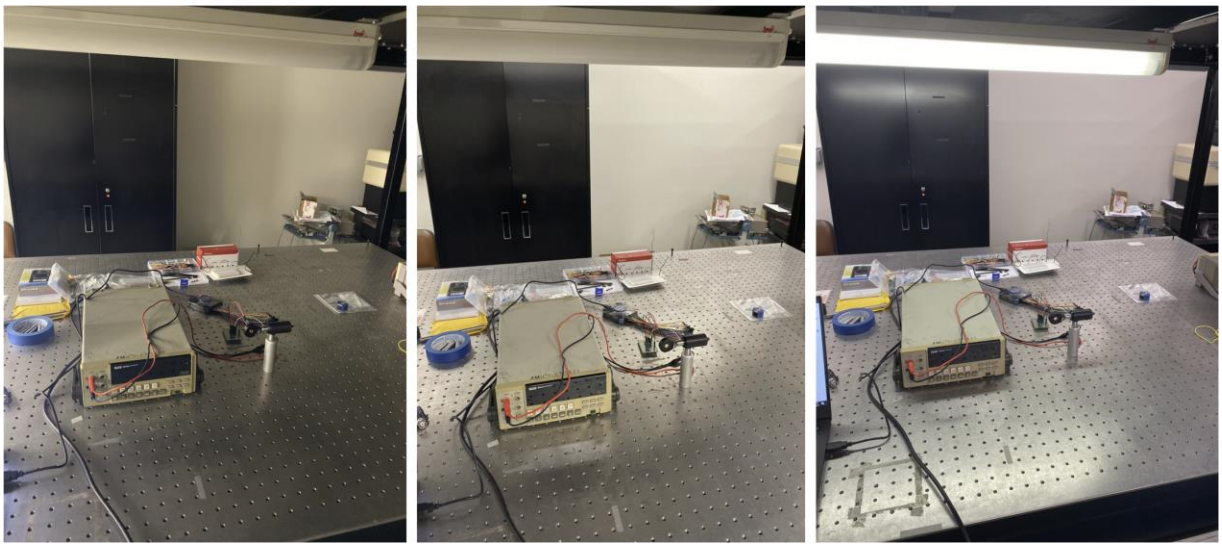

Figure 1.6.17: Noise Measurement Experimental Setup

Note that in Figure 1.6.17, the left picture corresponds to half the room lights being off (dim), the middle picture corresponds to the room lights being on but the overhead optic table

light being off (regular), and the right picture corresponds to all lights being on (bright). The PD was mounted such that it can rotated around towards and away from the lights. The Lab PD was set up in the exact same conditions.

1.6.1.11 Distance Measurements and Validation

The second experimental validation step will be to extensively measure PD operating circuit voltages relating to VCSEL diode beam incidence across the application range of one to ten meters. In order to perform these measurements, precise optomechanical mounts must be used with optical measurement tables to produce reliable results. Luckily, the Wisenbaker lab had enough optical measurement tables and space to produce the desired measurement range depicted in Figure 1.6.18. With this range of possible measurements, several key distances were chosen. Figure 1.6.19 depicts the experimental set up for the FDS100 PD operating circuit and the Lab PD distance measurements followed a similar setup. Figure 1.6.20 depicts an actual example of one of the first measurements for the PD operating circuit.

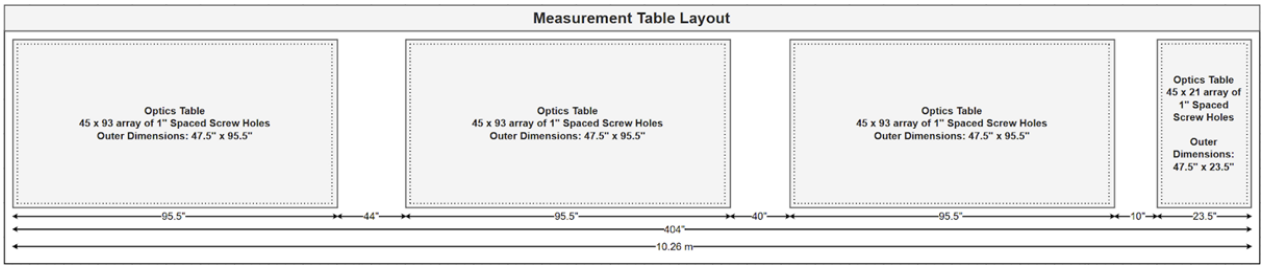

Figure 1.6.18: Optical Measurement Table Layout

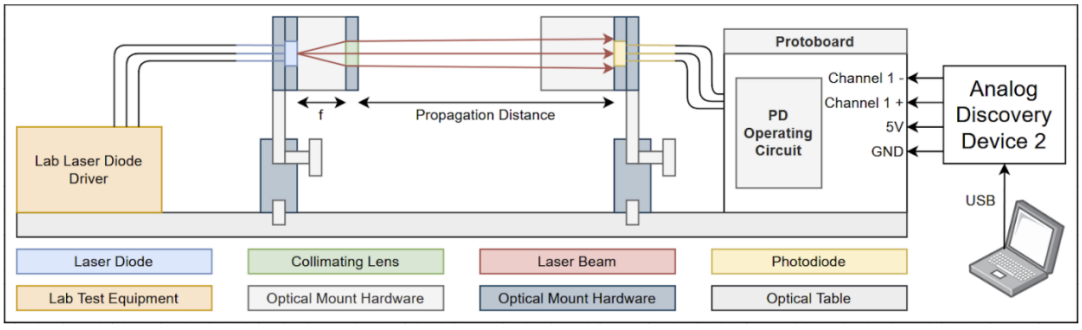

Figure 1.6.19: FDS100 Distance Measurement Experimental Setup

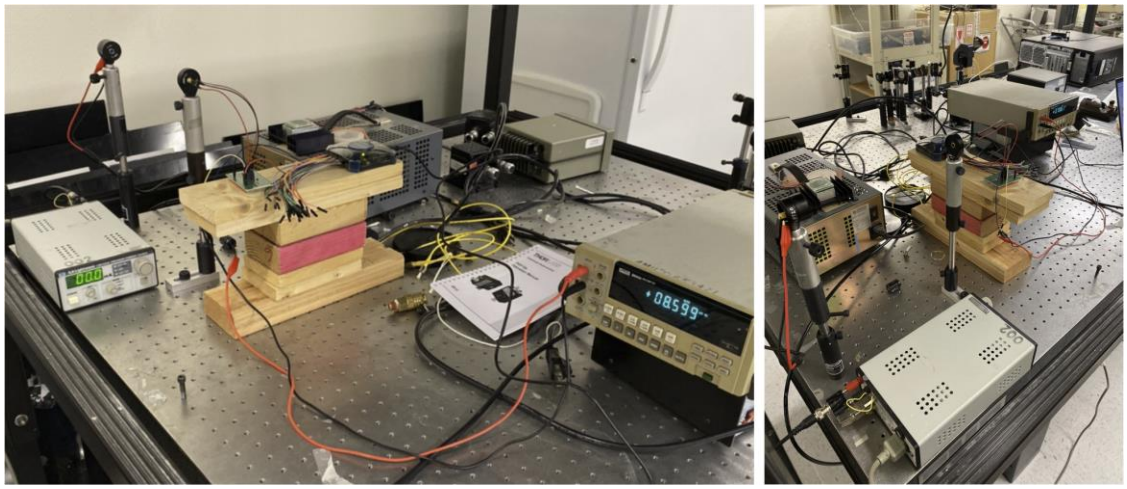

Figure 1.6.20: Actual Experimental Setup for PD Operating Circuit

With this setup, several different measurements will be taken for various reasons. First off, at each distance and specific setting, the measurement ambient noise will be recorded. This will likely not be near maximum noise values as the PDs will not be pointing at a room light source and the lights will be dimmed anyway to facilitate visual beam alignment. For the Lab PD, like in the noise measurements, each measurement will be taken with the standard aperture of 100 mm2 and the limited aperture of 13 mm2 to provide additional comparison to the FDS100 PD operating circuit. For the FDS100 PD operating circuit, each measurement will be conducted in both photoconductive and photovoltaic modes in order to define and compare the performance of each mode. Each measurement will also be conducted with VCSEL diode drive currents of 6 mA, 7 mA, and 8 mA in order to see how the drive current affects the measurement results. Finally, each measurement will be conducted with the beam centered on the photodetector area and with the beam centered on the edge of the photodetector area. This will be done to gain more insight into how precise alignment will eventually need to be as well as to gather information relating to the difference in these values as the beam radius and propagation distance increase. For clarification, this is depicted in Figure 1.6.21, but note that the beam radius will span from

being much smaller than depicted in the figure to much larger. As a result, there will be some interesting results as this change occurs. Also, the non-Gaussian irradiance pattern at ten meters shown in Figure 1.6.13 will likely produce some interesting results with these measurements.

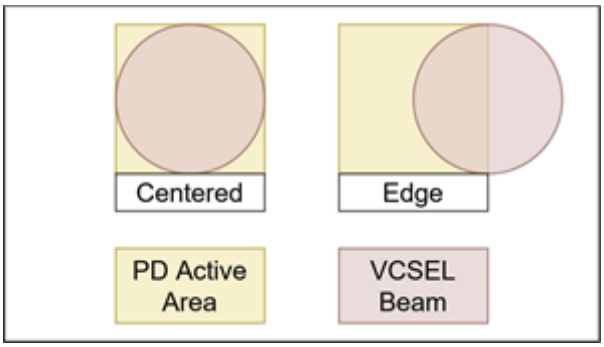

Figure 1.6.21: PD Measurement Alignment Key

1.6.1.12 Alignment Sweep Measurements and Validation

After seeing the effects beam alignment on the active area of the PD had on the above distance measurements, additional validation was planned. Additional alignment cases were measured at one, five, and ten meters for both PV and PC modes to gain additional insight. The updated alignment key is included in Figure 1.6.22.

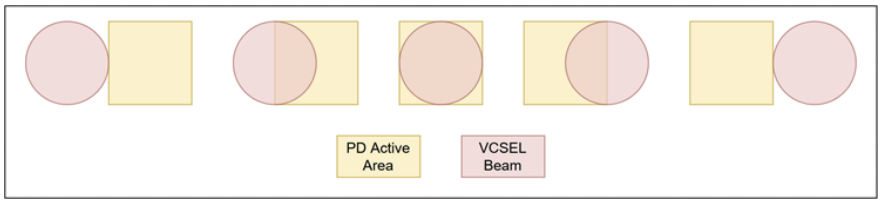

Figure 1.6.22: PD Alignment Sweep Key

1.6.1.13 Incident Angle Measurements and Validation

When the optical path subsystem is integrated into the full system, there is a chance that perfect orientational alignment permitting normal incidence of the VCSEL diode beam on to the PD operating circuit detector areas may not be exact. For instance, the beam may be incident at small angles. To account for this, the optical path subsystem must still be able to detect the beam

and distinguish the corresponding measurement voltage from noise. Luckily, irradiance has a pretty clear relationship with incident angles explained by the following simple equation:

$$I = I_0 * cos\theta$$

Where I_0 is the maximum irradiance corresponding to normal incidence and θ is the incident angle relative to the detector surface normal. This cosine relationship shows that relatively small incident angles will have very little impact on the irradiance magnitude detected by the PD. However, for the sake of completeness, this was validated using an experimental setup as shown in Figure 1.6.23. Both PV and PC modes were measured and the beam was centered on the detector.

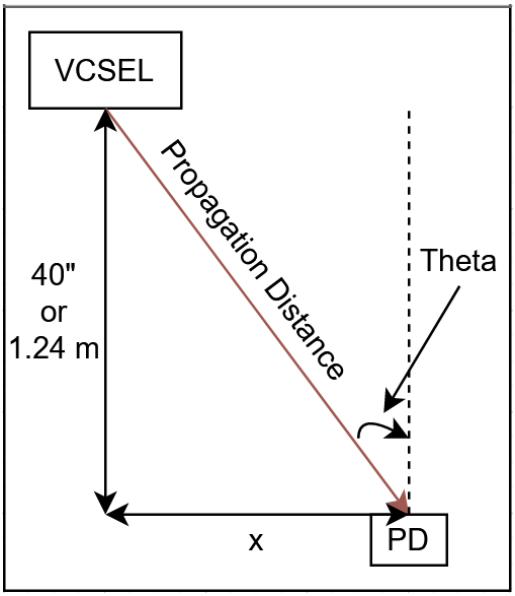

Figure 1.6.23: Angle Measurement Setup

These measurements were taken for a propagation distance of approximately one meter using a drive current of 7 mA. Assuming a massive alignment error resulting in a maximum incident angle of 15°, the following measurement cases were considered:

1. x = 11”, theta = 15.4 degrees, Propagation Distance = 41.5” compared to Directly Incident Value at 41”
2. x = 7”, theta = 9.93 degrees, Propagation Distance = 40.6” compared to Directly Incident Value at 41”
3. x = 4”, theta = 5.71 degrees, Propagation Distance = 40.2” compared to Directly Incident Value at 40”

Note: There are slight approximations in these measurements, however, the resulting minimal difference in values is all that is desired.

1.6.2 Optical Path Subsystem Results

This section includes the results of the optical path subsystem validation tests conducted as described in the Optical Path Subsystem Methods section.

1.6.2.1 Ambient Noise Measurements and Validation Results

By collecting noise data for different rotations of the PDs for each case of dim, regular, and bright lighting, the data shown in Table 1.6.3 was collected. Note that the PD operating circuit was measured while in the photoconductive mode as this would produce a higher noise value relative to the photovoltaic mode. The resulting data shows that the maximum ambient noise conditions measured for both photodetectors was around 40 mV, with the PD operating circuit having an exact maximum value of 38.5 mV in these conditions. It is fair to assume that regular room lighting conditions as defined by the intended application of the system will not exceed an ambient noise value of 40 mV. This ambient noise measurement will likely be much smaller the measured voltages for the VCSEL diode beam due to the wavelength dependent responsivity of the photodiodes and the broadband ambient light sources in a room compared to

the very narrowband VCSEL diode. However, these assumptions must be proven through exhaustive distance measurements completed in the next validation phase.

Table 1.6.3: PD Noise Measurement and Validation Data

Orientation	Lighting	Lab PDA100A Photodetector		FDS100 Operating Circuit - PC (mV)
		Aperture	Voltage (mV)	
N/A	Covered (None)	Standard (100 mm^2)	9.09	0.2
		Limited (13 mm^2)		
Parallel to Table Forward	Dim	Standard (100 mm^2)	10.19	1.18
		Limited (13 mm^2)	9.11	
Parallel to Table Forward	Regular	Standard (100 mm^2)	29.66	22.3
		Limited (13 mm^2)	9.35	
Parallel to Table Forward	Bright	Standard (100 mm^2)	30.57	22.8
		Limited (13 mm^2)	9.39	
Parallel to Table Backward	Dim	Standard (100 mm^2)	9.87	0.916
		Limited (13 mm^2)	9.09	
Parallel to Table Backward	Regular	Standard (100 mm^2)	15.92	8.42
		Limited (13 mm^2)	9.2	
Parallel to Table Backward	Bright	Standard (100 mm^2)	17.15	13.5
		Limited (13 mm^2)	9.23	
Tilted 45° Up Forward	Dim	Standard (100 mm^2)	10.38	0.727
		Limited (13 mm^2)	9.12	
Tilted 45° Up Forward	Regular	Standard (100 mm^2)	31.89	18.7
		Limited (13 mm^2)	10.84	
Tilted 45° Up Forward	Bright	Standard (100 mm^2)	32.59	25.5
		Limited (13 mm^2)	10.87	
Tilted 45° Down Forward	Dim	Standard (100 mm^2)	9.64	0.677
		Limited (13 mm^2)	9.1	
Tilted 45° Down Forward	Regular	Standard (100 mm^2)	18.1	10.9
		Limited (13 mm^2)	9.37	
Tilted 45° Down Forward	Bright	Standard (100 mm^2)	19.02	13.4
		Limited (13 mm^2)	9.39	
Tilted 45° Up Backward	Dim	Standard (100 mm^2)	9.76	0.855
		Limited (13 mm^2)	9.09	
Tilted 45° Up Backward	Regular	Standard (100 mm^2)	14.73	9.08
		Limited (13 mm^2)	9.22	
Tilted 45° Up Backward	Bright	Standard (100 mm^2)	38.7	31.5
		Limited (13 mm^2)	9.28	
Tilted 45° Down Backward	Dim	Standard (100 mm^2)	9.34	0.359
		Limited (13 mm^2)	9.09	
Tilted 45° Down Backward	Regular	Standard (100 mm^2)	12.41	5.47
		Limited (13 mm^2)	9.19	
Tilted 45° Down Backward	Bright	Standard (100 mm^2)	16.89	10.12
		Limited (13 mm^2)	9.25	
Tilted 90° Up	Dim	Standard (100 mm^2)	9.39	0.804
		Limited (13 mm^2)	9.09	
Tilted 90° Up	Regular	Standard (100 mm^2)	15.5	9.69
		Limited (13 mm^2)	9.13	
Tilted 90° Up	Bright	Standard (100 mm^2)	40.79	35.2
		Limited (13 mm^2)	9.22	
Tilted 90° Down	Dim	Standard (100 mm^2)	9.35	0.201
		Limited (13 mm^2)	9.09	
Tilted 90° Down	Regular	Standard (100 mm^2)	13.47	5.82
		Limited (13 mm^2)	9.14	
Tilted 90° Down	Bright	Standard (100 mm^2)	17.87	9.18
		Limited (13 mm^2)	9.32	
Aimed at Light (Until Max Value)	Bright	Standard (100 mm^2)	40.89	38.5
		Limited (13 mm^2)	11.61	

1.6.2.2 Distance Measurements and Validation Results

The resulting data for the validation described in 1.6.1.11 are included in Table 1.6.4.

Table 1.6.4: PD Distance Measurement Results

Distance (in)	Distance (m)	OPV310 Drive Current (mA)	Lab PDA100A Photodetector				FDS100 Operating Circuit			
			Aperture	Beam Centered on Detector Edge (V)	Beam Centered on Detector (V)	Ambient Noise (mV)	Power Supply	Beam Centered on Detector Edge (V)	Beam Centered on Detector (V)	Ambient Noise (mV)
10	0.254	6	Standard (100 mm^2)	0.073	2.38	Standard: 9.38 Limited: 9.09	Off	0.195	0.473	Power Supply Off: 0.630 Power Supply On: 0.631
			Limited (13 mm^2)	0.0948	2.26		On (5V)	0.191	5.02	
10	0.254	7	Standard (100 mm^2)	0.102	2.94		Off	0.302	0.479	
			Limited (13 mm^2)	0.14	2.7		On (5V)	0.392	5.03	
10	0.254	8	Standard (100 mm^2)	0.159	3.43		Off	0.326	0.485	
			Limited (13 mm^2)	0.201	3.13		On (5V)	0.55	5.04	
20	0.508	6	Standard (100 mm^2)	0.371	2.21	Standard: 15.45 Limited: 9.31	Off	0.387	0.465	Power Supply Off: 0.581 Power Supply On: 0.590
			Limited (13 mm^2)	0.811	1.74		On (5V)	1.92	5	
20	0.508	7	Standard (100 mm^2)	0.498	2.55		Off	0.395	0.469	
			Limited (13 mm^2)	0.956	1.93		On (5V)	2.27	5.01	
20	0.508	8	Standard (100 mm^2)	0.629	2.91		Off	0.401	0.472	
			Limited (13 mm^2)	1.12	2.11		On (5V)	2.7	5.02	
30	0.762	6	Standard (100 mm^2)	0.207	1.95	Standard: 14.66 Limited: 9.28	Off	0.396	0.453	Power Supply Off: 0.589 Power Supply On: 0.608
			Limited (13 mm^2)	0.555	0.988		On (5V)	2.42	4.98	
30	0.762	7	Standard (100 mm^2)	0.281	2.22		Off	0.4	0.458	
			Limited (13 mm^2)	0.642	1.08		On (5V)	2.67	4.99	
30	0.762	8	Standard (100 mm^2)	0.363	2.46		Off	0.404	0.46	
			Limited (13 mm^2)	0.712	1.15		On (5V)	2.96	4.99	
40	1.016	6	Standard (100 mm^2)	0.198	1.69	Standard: 14.19 Limited: 9.29	Off	0.38	0.446	Power Supply Off: 0.642 Power Supply On: 0.650
			Limited (13 mm^2)	0.616	1.06		On (5V)	1.65	4.96	
40	1.016	7	Standard (100 mm^2)	0.257	1.88		Off	0.385	0.449	
			Limited (13 mm^2)	0.695	1.16		On (5V)	1.8	4.97	
40	1.016	8	Standard (100 mm^2)	0.329	2.05		Off	0.386	0.452	
			Limited (13 mm^2)	0.758	1.22		On (5V)	1.94	4.97	
60	1.524	6	Standard (100 mm^2)	0.491	1.32	Standard: 14.03 Limited: 9.33	Off	0.395	0.43	Power Supply Off: 0.827 Power Supply On: 0.836
			Limited (13 mm^2)	0.583	0.738		On (5V)	2.14	4.87	
60	1.524	7	Standard (100 mm^2)	0.57	1.45		Off	0.396	0.435	
			Limited (13 mm^2)	0.648	0.81		On (5V)	2.33	4.91	
60	1.524	8	Standard (100 mm^2)	0.667	1.53		Off	0.397	0.436	
			Limited (13 mm^2)	0.715	0.862		On (5V)	2.41	4.92	
80	2.032	6	Standard (100 mm^2)	0.391	1.06	Standard: 13.69 Limited: 9.18	Off	0.382	0.416	Power Supply Off: 11.4 Power Supply On: 11.5
			Limited (13 mm^2)	0.339	0.496		On (5V)	1.66	3.71	
80	2.032	7	Standard (100 mm^2)	0.447	1.16		Off	0.385	0.421	
			Limited (13 mm^2)	0.378	0.552		On (5V)	1.79	4.08	
80	2.032	8	Standard (100 mm^2)	0.515	1.25		Off	0.386	0.422	
			Limited (13 mm^2)	0.455	0.632		On (5V)	1.86	4.24	
90	2.286	6	Standard (100 mm^2)	0.305	1	Standard: 16.91 Limited: 9.17	Off	0.382	0.403	Power Supply Off: 10.1 Power Supply On: 10.2
			Limited (13 mm^2)	0.333	0.397		On (5V)	1.67	2.7	
90	2.286	7	Standard (100 mm^2)	0.345	1.1		Off	0.385	0.408	
			Limited (13 mm^2)	0.368	0.435		On (5V)	1.82	3.03	
90	2.286	8	Standard (100 mm^2)	0.396	1.17		Off	0.387	0.409	
			Limited (13 mm^2)	0.418	0.467		On (5V)	1.89	3.12	
140	3.556	6	Standard (100 mm^2)	0.345	0.72	Standard: 9.87 Limited: 9.19	Off	0.357	0.36	Power Supply Off: 1.02 Power Supply On: 1.04
			Limited (13 mm^2)	0.165	0.165		On (5V)	0.973	1.04	
140	3.556	7	Standard (100 mm^2)	0.378	0.795		Off	0.36	0.365	
			Limited (13 mm^2)	0.179	0.179		On (5V)	1.04	1.15	
140	3.556	8	Standard (100 mm^2)	0.409	0.837		Off	0.362	0.366	
			Limited (13 mm^2)	0.214	0.217		On (5V)	1.09	1.18	
160	4.064	6	Standard (100 mm^2)	0.341	0.648	Standard: 9.82 Limited: 9.17	Off	0.352	0.346	Power Supply Off: 0.898 Power Supply On: 0.910
			Limited (13 mm^2)	0.125	0.113		On (5V)	0.88	0.786	
160	4.064	7	Standard (100 mm^2)	0.377	0.715		Off	0.357	0.354	
			Limited (13 mm^2)	0.139	0.123		On (5V)	0.976	0.938	
160	4.064	8	Standard (100 mm^2)	0.407	0.751		Off	0.358	0.353	
			Limited (13 mm^2)	0.157	0.13		On (5V)	0.997	0.896	
200	5.08	6	Standard (100 mm^2)	0.286	0.469	Standard: 9.40 Limited: 9.19	Off	0.34	0.314	Power Supply Off: 7.42 Power Supply On: 7.51
			Limited (13 mm^2)	0.0828	0.0679		On (5V)	0.681	0.421	
200	5.08	7	Standard (100 mm^2)	0.313	0.517		Off	0.343	0.328	
			Limited (13 mm^2)	0.0899	0.0775		On (5V)	0.732	0.506	
200	5.08	8	Standard (100 mm^2)	0.333	0.536		Off	0.346	0.322	
			Limited (13 mm^2)	0.11	0.0996		On (5V)	0.771	0.461	
230	5.842	6	Standard (100 mm^2)	0.348	0.333	Standard: 9.29 Limited: 9.17	Off	0.316	0.286	Power Supply Off: 5.65 Power Supply On: 5.73
			Limited (13 mm^2)	0.0565	0.0519		On (5V)	0.464	0.335	
230	5.842	7	Standard (100 mm^2)	0.384	0.376		Off	0.324	0.305	
			Limited (13 mm^2)	0.0621	0.0598		On (5V)	0.513	0.403	
230	5.842	8	Standard (100 mm^2)	0.422	0.408		Off	0.325	0.297	
			Limited (13 mm^2)	0.0856	0.0829		On (5V)	0.531	0.372	
280	7.112	6	Standard (100 mm^2)	0.238	0.212	Standard: 9.72 Limited: 9.14	Off	0.248	0.201	Power Supply Off: 0.830 Power Supply On: 0.843
			Limited (13 mm^2)	0.0539	0.0389		On (5V)	0.26	0.206	
280	7.112	7	Standard (100 mm^2)	0.266	0.241		Off	0.264	0.232	
			Limited (13 mm^2)	0.0564	0.0443		On (5V)	0.287	0.24	
280	7.112	8	Standard (100 mm^2)	0.286	0.272		Off	0.275	0.224	
			Limited (13 mm^2)	0.0592	0.0511		On (5V)	0.306	0.231	
320	8.128	6	Standard (100 mm^2)	0.184	0.159	Standard: 9.19 Limited: 9.14	Off	0.239	0.16	Power Supply Off: 0.505 Power Supply On: 0.511
			Limited (13 mm^2)	0.0447	0.0329		On (5V)	0.249	0.163	
320	8.128	7	Standard (100 mm^2)	0.202	0.182		Off	0.256	0.198	
			Limited (13 mm^2)	0.0463	0.037		On (5V)	0.272	0.202	
320	8.128	8	Standard (100 mm^2)	0.238	0.218		Off	0.262	0.174	
			Limited (13 mm^2)	0.0473	0.038		On (5V)	0.282	0.177	
360	9.144	6	Standard (100 mm^2)	0.147	0.127	Standard: 9.35 Limited: 9.15	Off	0.196	0.125	Power Supply Off: 0.340 Power Supply On: 0.345
			Limited (13 mm^2)	0.0371	0.0286		On (5V)	0.2	0.127	
360	9.144	7	Standard (100 mm^2)	0.16	0.141		Off	0.211	0.162	
			Limited (13 mm^2)	0.0389	0.031		On (5V)	0.216	0.164	
360	9.144	8	Standard (100 mm^2)	0.175	0.159		Off	0.216	0.136	
			Limited (13 mm^2)	0.0399	0.0342		On (5V)	0.221	0.138	
395	10.033	6	Standard (100 mm^2)	0.106	0.099	Standard: 9.21 Limited: 9.10	Off	0.189	0.095	Power Supply Off: 0.168 Power Supply On: 0.170
			Limited (13 mm^2)	0.0266	0.0231		On (5V)	0.193	0.0965	
395	10.033	7	Standard (100 mm^2)	0.118	0.1134		Off	0.204	0.119	
			Limited (13 mm^2)	0.0267	0.0261		On (5V)	0.209	0.121	
395	10.033	8	Standard (100 mm^2)	0.123	0.12		Off	0.215	0.103	
			Limited (13 mm^2)	0.03	0.0284		On (5V)	0.221	0.105	

The results shown in Table 1.6.4 are best described when visualized in to data plots. Many plots highlighting different information from this data can be generated, but only a few will be shown here. Results from the plots not included show that the Lab PD performed similarly to the photoconductive mode of the FDS100 PD operating circuit when it had the standard aperture; however, the limited aperture brought measurement values close to noise at 10 meters. Overall, comparison with the Lab PD shows that the FDS100 PD operating circuit performed exceptionally well and is more favorable to use in the optical path subsystem. Looking more specifically into the FDS100 PD operating circuit performance, Figure 1.6.24 shows the results for the photovoltaic mode, Figure 1.6.25 shows the results for the photoconductive mode, and Figure 1.6.26 shows an overlayed comparison of the two modes looking only at a drive current of 7 mA. Note that around four meters for both plots the beam centered at detector edge measurements become larger in magnitude than the beam centered on detector measurements. The data points corresponding to this crossover are highlighted in blue in Table 1.6.4. Also, note that this same phenomenon occurred with the Lab PD. As expected, this is a direct result of the multimode beam profile of the VCSEL diode exhibiting a slightly non-Gaussian irradiance pattern at larger distances. This phenomenon and its effects on the system will be discussed in the Optical Path Subsystem Conclusions section. Some brief observations which can be drawn from Figures 1.6.24 – 1.6.26 and will also be expanded upon later include the relatively close measurement values with changing drive current, the disparity in Photoconductive (PC) and Photovoltaic (PV) values from zero to seven meters, and the similarity in PC and PV values from seven meters to ten meters. Also, all the beam-related distance measurements showed a clear distinction from the maximum ambient noise value.

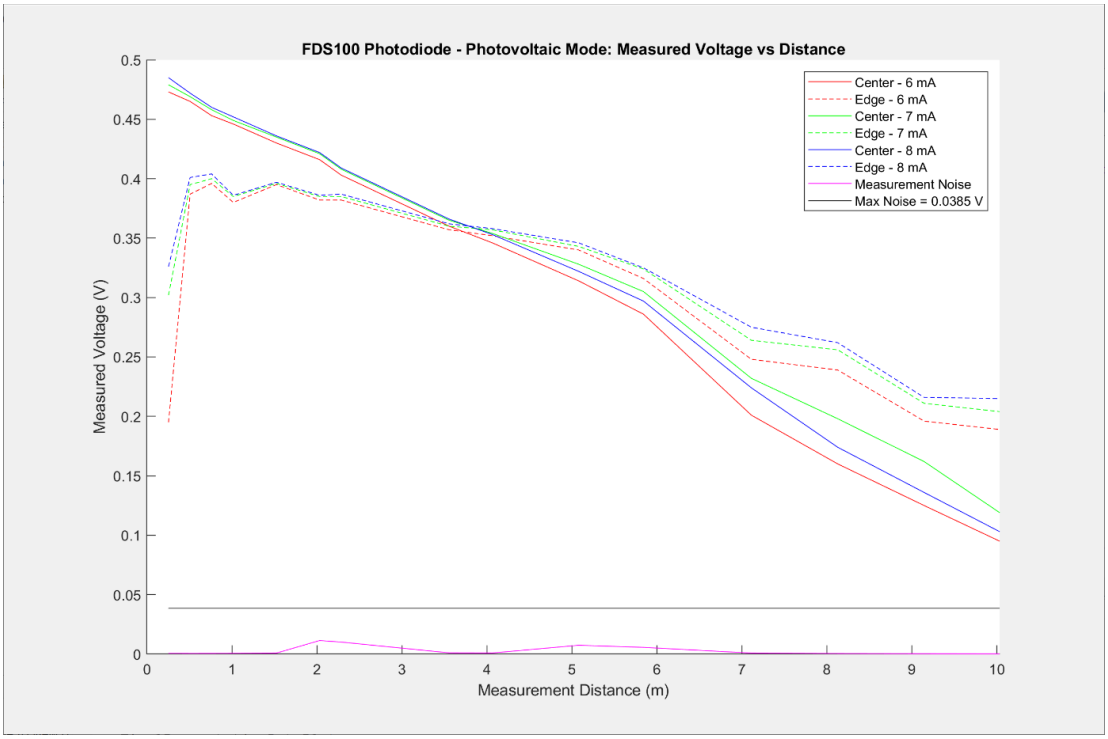

Figure 1.6.24: FDS100 PD Operating Circuit Distance Measurements – Photovoltaic Mode

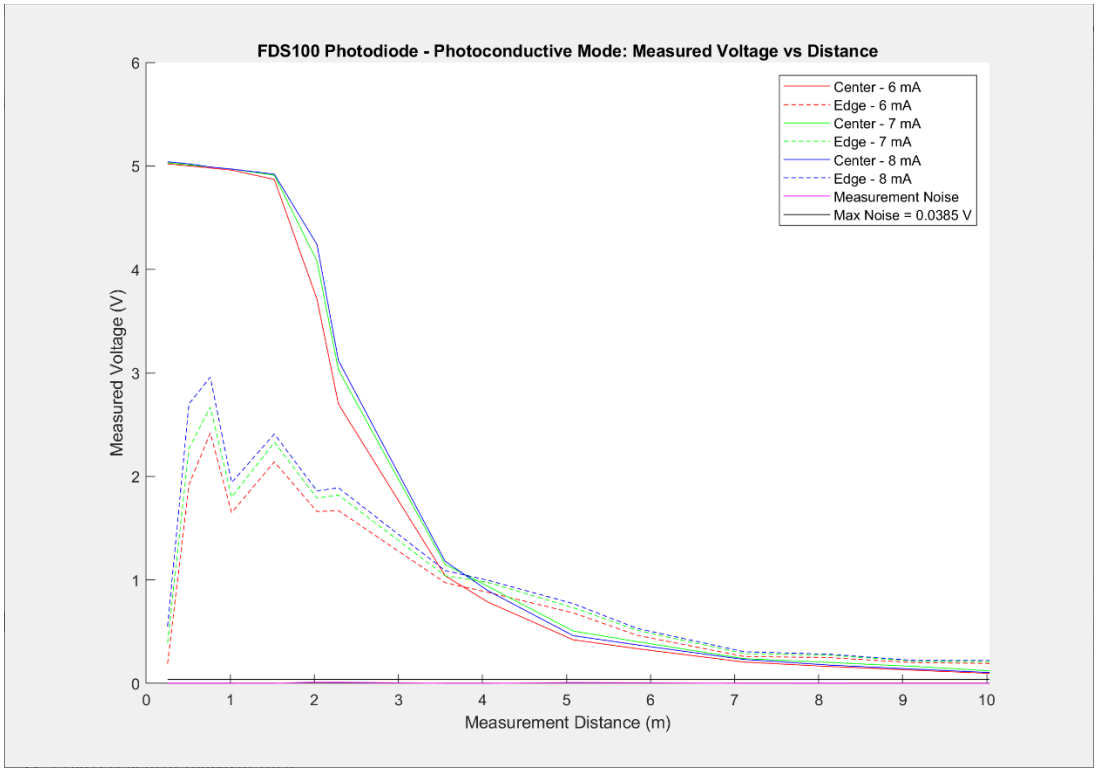

Figure 1.6.25: FDS100 PD Operating Circuit Distance Measurements – Photoconductive Mode

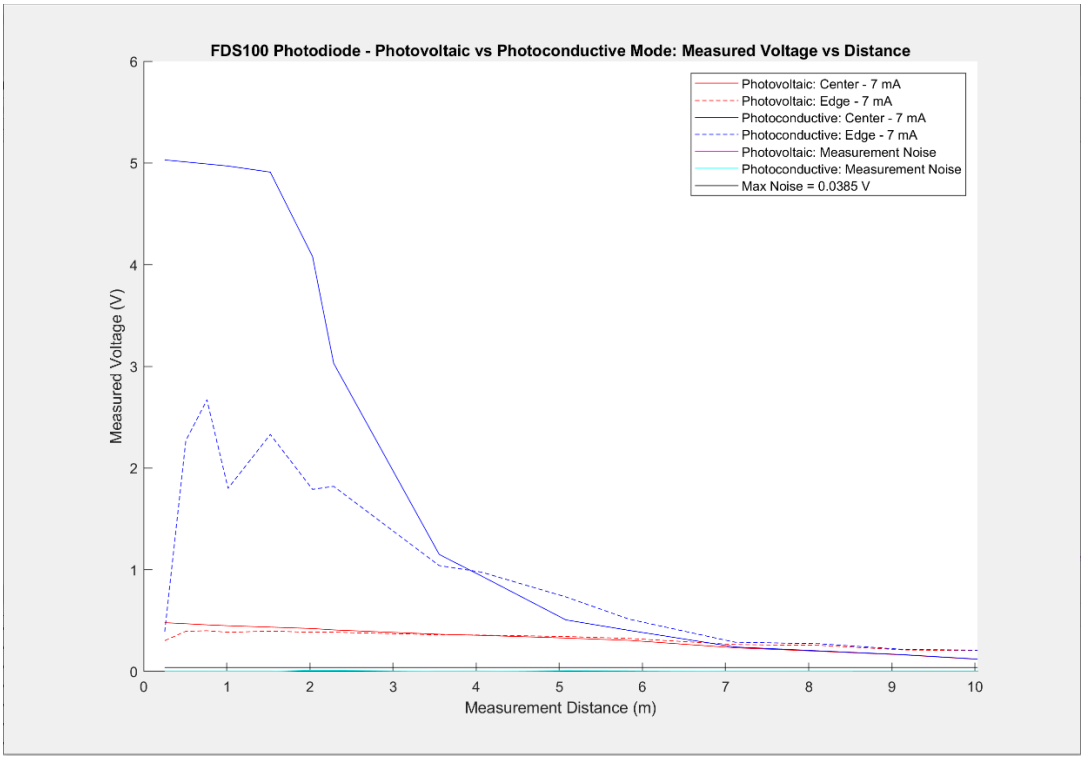

Figure 1.6.26: FDS100 PD Operating Circuit: PV vs PC Mode Distance Measurements

1.6.2.3 Alignment Sweep Measurements and Validation Results

The resulting data from the measurements and validation described in 1.6.1.12 is included in Table 1.6.5. This data further examines and confirms the non-Gaussian irradiance pattern for the VCSEL diode at distances larger than four meters for the PD operating circuit. For this irradiance pattern, the resulting data shows that a peak value occurs for the “Beam Centered at Detector Edge” case which decreases with the “Beam Centered on Detector” cases and decreases further for the “Beam Edge on Detector Edge” cases. Also, it seemed the peaks were not uniform for each beam side with the first edge cases having larger magnitudes than the second edge cases.

Table 1.6.5: PD Operating Circuit Alignment Sweep

Distance (in)	Distance (m)	OPV310 Drive Current (mA)	FDS100 Operating Circuit						
			Power Supply	Beam Edge on 1st Detector Edge (V)	Beam Centered on 1st Detector Edge (V)	Beam Centered on Detector (V)	Beam Edge on 2nd Detector Edge (V)	Beam Centered on 2nd Detector Edge (V)	Ambient Noise (mV)
40	1.016	7	Off	0.343	0.388	0.449	0.387	0.346	0.573
			On (5V)	0.58	1.32	4.96	1.12	0.772	0.578
200	5.08	7	Off	0.118	0.334	0.318	0.309	0.0826	0.301
			On (5V)	0.119	0.605	0.473	0.412	0.0844	0.306
395	10.033	7	Off	0.0334	0.181	0.121	0.132	0.0243	0.163
			On (5V)	0.0339	0.184	0.123	0.137	0.0247	0.168

1.6.2.4 Incident Angle Measurements and Validation Results

The results for the measurements and validation described in 1.6.1.13 are shown in Table 1.6.6. The values were essentially unchanged as incident angle was increased and the ambient noise values were quite similar as well. As expected, incident angles of this range have miniscule effects on the PD Operating circuit measurements.

Table 1.6.6: FDS100 PD Operating Circuit Angled Measurement Results

Distance (in)	Distance (m)	OPV310 Drive Current (mA)	FDS100 Operating Circuit			
			Incident Angle	Power Supply	Beam Centered on Detector (V)	Ambient Noise (mV)
40	1.016	7	0°	Off	0.448	6.43
				On (5V)	4.97	6.51
			5.71°	Off	0.446	6.38
				On (5V)	4.96	6.46
41	1.0414	7	0°	Off	0.448	6.47
				On (5V)	4.97	6.55
			9.93°	Off	0.447	6.38
				On (5V)	4.96	6.45
			15.4°	Off	0.446	6.39
				On (5V)	4.96	6.46

1.6.3 Optical Path Subsystem Conclusions

The 1.6.2 Optical Path Subsystem Results section contains a large amount of information which upon further analysis can lead to a variety of conclusions being drawn about the performance of the optical path subsystem. These conclusions will be organized into sections relating to certain validation measurements or topics, and then overall conclusions of subsystem performance and considerations will be evaluated at the interface level.

1.6.3.1 Ambient Noise

Ambient noise, referring to other optical sources in the intended application environment, is an important consideration for the optical path subsystem. Anything from typical room lighting to sunlight present a potential optical source that can contribute to measured voltages coming from the PD operating circuit. In order to facilitate data transmission, the detected VCSEL diode beam must be distinguishable in terms of measured voltage from this ambient noise. During the ambient noise measurements and validation included in 1.6.2.1 (see Table 1.6.3 and Figure 1.6.17), it was determined that the maximum amount of noise that would likely be encountered in the intended application space would result in a measured voltage of around 40 mV across the load resistor of the PD operating circuit operating in PC mode. This value corresponded to a large amount of diffuse light in the room and the PD being aimed directly at a broadband, powerful light source. During the distance measurement and validation in the Validation section (see Table 1.6.4 and Figures 1.6.24-1.6.26), it became evident that the VCSEL beam was clearly distinguishable from the maximum noise value across the application range of one to ten meters and independently from drive current and PD mode. The closest observed value to the maximum noise was a measurement of 95 mV taken at ten meters, in PV mode, centered on the detector, with less than a millivolt of ambient noise, and with a drive current of 6 mA – all of which are parameters being those that decrease the measured voltage. This value is still more than twice the maximum noise value of nearly 40 mV. Evidently, it can safely be concluded that beam alignment will produce measured voltages clearly distinguishable from ambient noise in the intended application of the system regardless of whichever measurement parameters are chosen. Theoretically, this can be explained by the higher responsivity of the PD

at the VCSEL diode wavelength and the relative irradiance of the beam compared to the broadband, diffused light sources in a typical room.

1.6.3.2 Distance Measurements

As mentioned in the distance measurements and validation part of the 1.6.2 (see Figures 1.6.24-1.6.26), several important observations and conclusions can be drawn from the data plots. These include the relatively close measurement values with changing drive current, the disparity in Photoconductive (PC) and Photovoltaic (PV) values from zero to seven meters, and the similarity in PC and PV values from seven meters to ten meters. Primarily, the differences visible in Figures 1.6.24 and 1.6.25 relating to the VCSEL diode drive current show a beneficial consistency. Throughout the application range of one to ten meters, the difference in VCSEL diode drive current did not produce any significant change in PD operating circuit measured voltage relative to the ability to distinguish the beam from ambient noise. Indeed, there are differences in the values, but the overall effect on the subsystem is negligible. Therefore, two conclusions can be drawn: the recommended drive current target of 7 mA is sufficient and any drive current in the range of 6 mA to 8 mA is thoroughly validated across the application range and will operate as required. This reduces the necessary accuracy and requirements of the laser diode controller of the link communication system and its corresponding interface by simplifying the necessary drive current and its relative consistency. Next is the discussion between the performance of the PD operating circuit when operating in PC vs PV mode. Figure 1.6.26 clearly shows that the PC data starts an order of magnitude higher than the PV data for the first several meters but then closely tracks the PV data from seven to ten meters with both staying above the maximum ambient noise value the whole time. Figure 1.6.26 also clearly depicts the relative consistency of the measured voltages for the PV data when compared to the PC data. Since the

large variation in measured voltages seen in the PC data does not produce any benefit to the system (and could possibly introduce issues later on with the link communication interface), the PC mode introduces the need for a reverse bias supplied by the Raspberry Pi for no productive reason. Therefore, the PV mode will be the initial PD operating circuit mode used for system integration to ensure subsystem interface performance and reduce the need to pull power for a reverse bias from the Raspberry Pi. Not only will this reduce complexity relating to the link communication interface, but it will also prevent a hard to measure power from being drawn from the Raspberry Pi which could potentially exceed certain limits and harm the device.

1.6.3.3 Incident Angle Measurements

The incident angle measurements included in the Validation section (see Figure 1.6.23 and Table 1.6.6) clearly prove the negligible effect VCSEL diode beam incidence angles on the PD active area have on the PD operating circuit measured voltages when kept below 15° which is a massive alignment tolerance. Even beyond this angle, however, the optical path subsystem will likely perform as required. Following the theory presented in 1.6.1.13, any significant change would have to result in a drop in beam irradiance by more than half which corresponds to an incident angle of over 60°. Such an incident angle would imply that the other module has not even attempted alignment.

1.6.3.4 VCSEL Far Field Pattern and Beam Alignment with PD

Experimental results often deviate from theory and assumptions aren't always dependable, this topic is a clear example of such a case. In 1.6.1, Gaussian beam theory was used to estimate beam characteristics and choose optical components. The exceptional results left a wide margin for experimental error, which luckily was not exceeded. Figure 1.6.6 depicts a classic Gaussian beam irradiance distribution given the VCSEL diode specifications and a

propagation distance of 10 meters. Moreover, Figure 1.6.4 claims the expected collimated beam radius at 10 meters would only be 2.33 mm. However, after the collimation process, the clear deviation from these theoretical expectations is realized. Figure 1.6.13 shows the beam on an infrared sensor card at one meter and ten meters respectively. While the one-meter image follows expectations, the ten-meter image clearly shows a non-Gaussian irradiance distribution of a much larger beam radius. This is indicative of some multimode behavior of the VCSEL diode which is not significantly or detectably different from Gaussian beam behavior until a certain distance. The distance measurement plots (Figures 1.6.24-1.6.26) shed some more light on this phenomenon. At a distance of approximately four meters, the beam centered at detector edge measurements become larger in magnitude than the beam centered on detector measurements. This phenomenon is independent of the drive currents tested as well as the PD operating circuit mode. Also, the same phenomenon was noticed with the Lab PD. The difference in magnitude between these two differently aligned measurements increased with distance, leading to an eventual nearly 100% difference at 10 meters. Another interesting phenomenon would be that the beam centered on the detector measurement for a drive current of 7 mA became larger than that for a drive current of 8 mA after the same four-meter crossover mark. This indicates a slight dependence of drive current on the deviation between the beam centered at detector edge and beam centered on detector measurements. The alignment sweep measurements and validation (see Figure 1.6.22 and Table 1.6.5) further characterizes the non-Gaussian irradiance distribution. Nevertheless, this phenomenon, interesting as it is, will not negatively impact the subsystem performance. All the distance measurements are still clearly distinguishable from the ambient noise of the application environment which is the prerequisite to the facilitation of OWC data transmission. As long as a portion of the beam is detectable, however exactly aligned that

may be, data transmission would be feasible. Note that LiFi systems designed with broad LED sources make use of this principle to cover a wide steradian range for data transmission without the need for tracking or alignment (but suffer from worse data transmission performance as mentioned in the introduction).

1.6.3.5 Link Communication / Optical Path Interface – Performance and Considerations

As mentioned above, the expected drive current from the link communication subsystem's laser diode controller need only fall within the range of 6 mA – 8 mA to fall under the validated range of measurements shown above. As long as the current is not sustained continuously at a value above 12 mA, the VCSEL diode will not be harmed. That being said, even drive currents between 8 mA – 12 mA, which will produce higher measured voltages and thus still be distinguishable from noise, would be acceptable. Therefore, this heavily simplifies the necessary output current characteristics of the laser diode controller and can allow a much simpler, cheaper, and more easily implementable design to be used. Such a design is discussed in the Link Communication Subsystem section. Regardless, as long as these interface requirements are met, the optical path subsystems for each module will operate successfully.

1.6.3.6 Optical Path / Link Communication Interface – Performance and Considerations

With the validation data collected and the conclusion drawn above that the favorable PD operating circuit mode to use is the photovoltaic (PV) mode, the interface with the link communication subsystem will operate successfully. The range of measured voltages across the application range (0 to a maximum of around 500 mV) for the PV data definitely fall within the required voltage range for the link communication subsystem's analog to digital converter. Moreover, the need for a 5 V supply from the Raspberry Pi to provide a reverse bias for the PC mode is not necessary which can avoid potentially harmful power draws from the Raspberry Pi.

Also, there is now a well-defined distance-based range of data for different beam alignments which can be combined with distance measurements from the module search subsystem to make more accurate decisions regarding how to interpret measured voltages from the PD operating circuit using the link communication subsystem's analog to digital converter when giving commands to the motor control subsystem for module/photodetector alignment.

1.6.3.7 Optical Path Interface Between Modules – Performance and Considerations

With the validation data obtained and analyzed related to the beam which will travel between the system modules, it can be concluded that a sufficient amount of optical power can be transferred/emitted and received/detected between modules. Moreover, the beam characteristics related to the specific optical components are well-defined and can be used to influence design decisions in the future for integration between subsystems.

1.7 Link Communication Subsystem

The link communication subsystem acts as a bridge between the functionality of the other subsystems. It connects the analog and optical components of the optical path subsystem with the digital and mechanical components of the module search and motor control subsystems. The functionality of this subsystem is divided into two main necessary capabilities each focused on a different end of the optical path subsystem: controlling the laser diode and measuring the output power of the photodetector. These capabilities facilitate the representative stationary link alignment process through programming scripts on the Raspberry Pi and are implemented physically with a laser diode controller (LDC) and an analog-to-digital converter (ADC). The chosen ADC is an Adafruit ADS1115.

1.7.1 Link Communication Subsystem Methods

1.7.1.1 ADC Code Logic

The following flowchart in Figure 1.7.1 shows implementation of the ADC in Python. The script currently runs on the Raspberry Pi independently of other subsystems. An actual LED is used in conjunction with the code to signal to the opposing module that the loop has been closed, but all other subsystem interfaces are represented by text output.

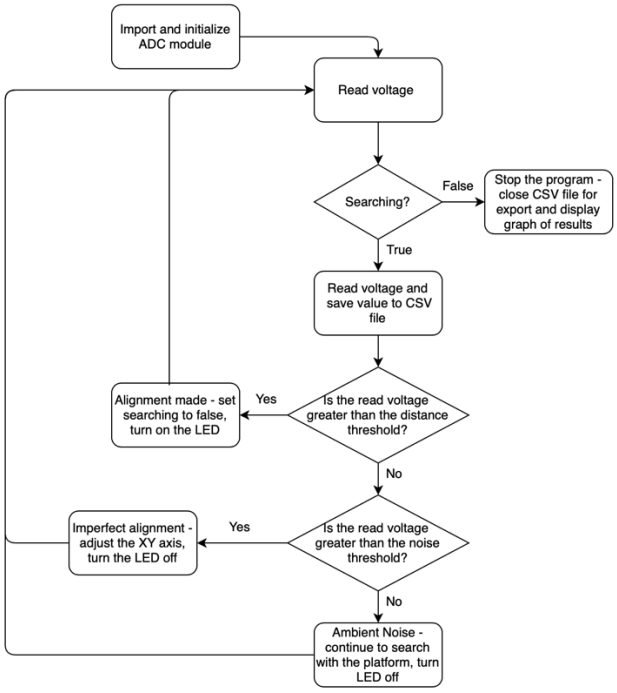

Figure 1.7.1: ADC Voltage Measurement Code Logic Flowchart

1.7.1.2 Laser Diode Controller Methods

The laser diode controller (LDC) is a necessary functionality of the link communication subsystem which is used to turn off and on the VCSEL diode of the optical path subsystem by supplying its drive current when deemed necessary by the system alignment process. This controller must reliably turn on and off the VCSEL diode when needed. It also must provide a sufficient drive current to ensure enough output optical power, but not too much drive current

that it will harm the diode. The beginning step for this process will be examining the chosen VCSEL diode's datasheet for key specifications.

The chosen VCSEL diode (see Section 1.6) is the TT Electronics OPV310 VCSEL diode. Through examining the diode's datasheet specifications with input from the optical path subsystem, the following design requirements for the LDC are as follows:

- The Maximum Forward Peak Current (also referred to as drive current elsewhere) must not exceed 12 mA in order to avoid damage to the diode.
- The standard operating conditions for the VCSEL diode include a forward current of 7 mA which will be the target value for the laser diode controller drive current (unless the optical path subsystem necessitates a different drive current down the road).
- The maximum forward voltage across the diode at the target drive current of 7 mA is 2.2 V and the minimum is 1.60 V.
- The threshold current for turning the diode on and emitting power is 1.5 mA. Therefore, the laser diode controller must have an output drive current less than this value when the VCSEL must be off.

Following these requirements, the LDC will be implemented in the form of a Constant Current Source (CCS). While avoiding complicated and expensive Integrated Circuits (ICs), simple active components come to mind when designing constant current sources. Specifically, Metal Oxide Semiconductor Field Effect Transistors (MOSFETs) are cheap and readily available transistors which are easily implementable in designs for constant current sources. Due to cost considerations and prior experience, the ON Semiconductor 2N7000 NMOS transistor was chosen to be utilized in these designs.

Figure 1.7.2 introduces the design for a simple constant current source which utilizes an NMOS transistor along with a source resistor to produce a constant drain current through the transistor which is set by the supply voltage, gate voltage, and the resistor at the source. The pictured schematic was generated in the Multisim software program. The gate voltage is set to 3.3 V to represent the GPIO pin coming from the Raspberry Pi which will turn on and off the diode. The load resistor value of 315Ω is meant to represent the maximum forward voltage across the VCSEL diode (2.2 V) at the target drive current of 7 mA. The source resistor value was determined using a parameter sweep until the DC operating point value pictured in Figure 1.7.3 was found to be close to 7 mA while still having a resistance that could be implemented with existing resistor values. Note: Multisim is using the default transistor parameters for the NMOS 2N7000. The resulting schematic must be robust to supply voltage variations in order to qualify as a CCS for the LDC's specific purposes. Therefore, a DC sweep of the source voltage was performed and produced Figure 1.7.4. Note that the current, in the simulated world of Multisim, stayed nearly the same across supply voltage variations.

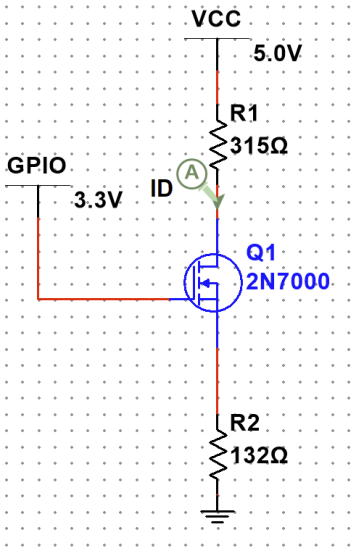

Figure 1.7.2: Simple Constant Current Source - Multisim Schematic

Simple Constant Current Source
DC Operating Point Analysis

	Variable	Operating point value
1	-I(R1:2) | I(ID)	7.01986 m

Figure 1.7.3: Simple Constant Current Source - DC Operating Point at Drain Node

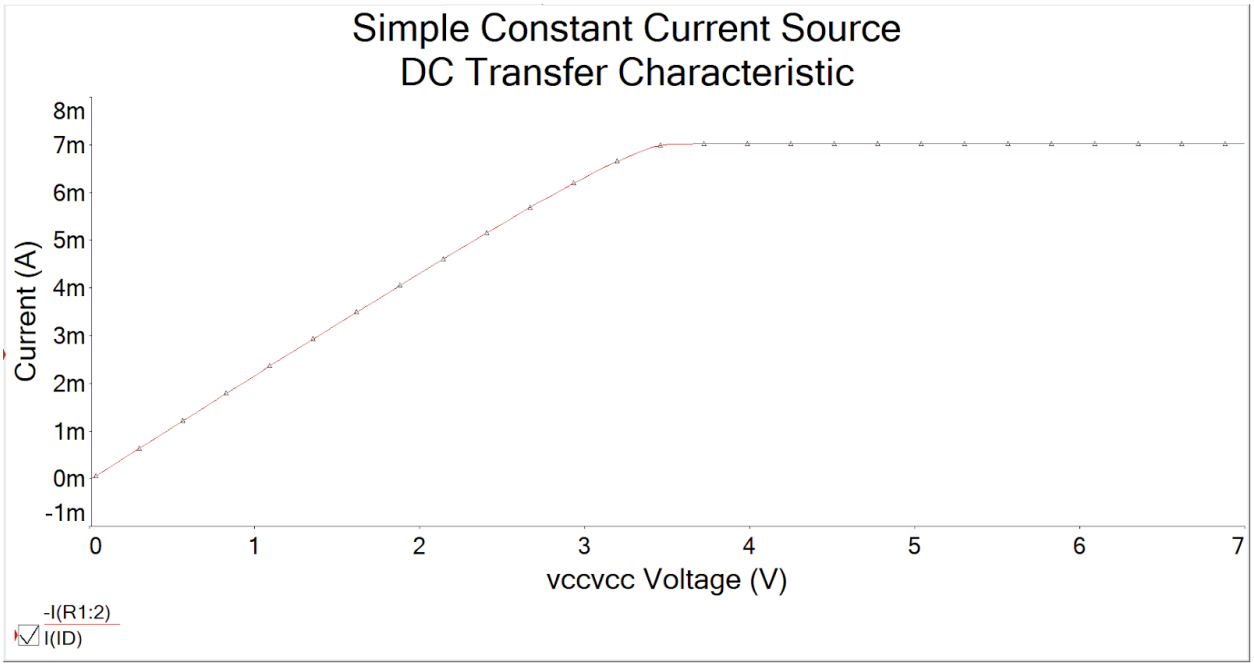

Figure 1.7.4: Simple Constant Current Source – Supply Voltage vs Drain Current

1.7.2 Link Communication Subsystem Results

1.7.2.1 ADC Results

The ADC precision was tested for 28 distinct voltages in a range of 0 to 5 volts. An Analog Discovery 2 device connected to a laptop was used to feed the varying voltages across a 10 kiloohm resistor. The ADS1115 in differential mode compared the perceived voltage difference from pin zero's ground to pin 1's high voltage and recorded this value for 300 samples. To account for variability and inconsistencies in the Analog Discovery 2, the average of these samples was recorded as the final result of each individual test. Measurements were concentrated around the predicted noise threshold (about 40 mV) and distance link threshold

(about 100 mV) since precision near these thresholds will dictate the efficacy of state transitions in the code. The results are shown below in Table 1.7.1 on the following page.

The far-left column of the above table denotes the voltage set by the laptop, while the column titled “Confirmed Voltage Given by Voltmeter” lists the actual measured voltage that the Analog Discovery 2 output across the resistor. The Analog Discovery 2’s internal resistance and loss accounted for an offset about 10 mV below the expected voltage. This finding did not impact the accuracy of the test, since the ADC’s measurements were compared directly to the voltmeter reading rather than the value displayed on the laptop.

Table 1.7.1: Discrete Value DC Voltage Readings

Voltage Fed by Source (V)	Confirmed Voltage Given by Voltmeter (V)	Recorded Average Voltage over 300 samples (1 V)	Percent Different
0.01	-0.009	0.00183	-120.33%
0.02	0.001	0.001027	2.70%
0.03	0.011	0.0205	86.36%
0.04	0.022	0.029	31.82%
0.06	0.043	0.048	11.63%
0.08	0.062	0.0659	6.29%
0.1	0.082	0.0843	2.80%
0.12	0.102	0.103	0.98%
0.15	0.132	0.131	-0.76%
0.2	0.182	0.18	-1.10%
0.25	0.232	0.229	-1.29%
0.3	0.285	0.278	-2.46%
0.4	0.384	0.374	-2.60%
0.5	0.485	0.469	-3.30%
0.6	0.585	0.566	-3.25%
0.7	0.683	0.66	-3.37%
1	0.985	0.946	-3.96%
1.5	1.487	1.421	-4.44%
2	1.988	1.893	-4.78%
2.5	2.489	2.369	-4.82%
3	2.989	2.837	-5.09%
3.5	3.489	3.304	-5.30%
3.8	3.789	3.58	-5.52%
4	3.99	3.78	-5.26%
4.2	4.189	3.936	-6.04%
4.5	4.492	4.243	-5.54%
4.7	4.691	4.421	-5.76%
5	4.993	4.638	-7.11%

In addition to reading voltages accurate, the ADC must read a constantly changing waveform and toggle an LED as a desired threshold is crossed. This functionality was confirmed by using the Analog Discovery 2 device connected through a laptop waveform generator to send a continuous and varying waveform over a 10 kiloohm resistor. The ADS1115 in differential mode compared and recorded the difference between pins zero and one straddling the resistor. The continuous test logged every state change in a .txt file, recording the toggling state of the LED as thresholds were crossed with time stamps. The sampled voltage values were recorded in their own csv until an external user quit the program, prompting an export of the file and graphical display of the ADC's recordings.

Four unique tests recorded the ADC's response to ramp up, ramp down, sin wave, and variable waveform functions. Shown in Figure 1.7.5 are the graphical visualization for the variable waveform and the corresponding text log documenting state changes. The test began with a ramp down function, which was changed to a ramp up around 5.5 seconds into the test. The ramp up was changed to a sin wave around 9 seconds, and the period was doubled around 11 seconds into the test.

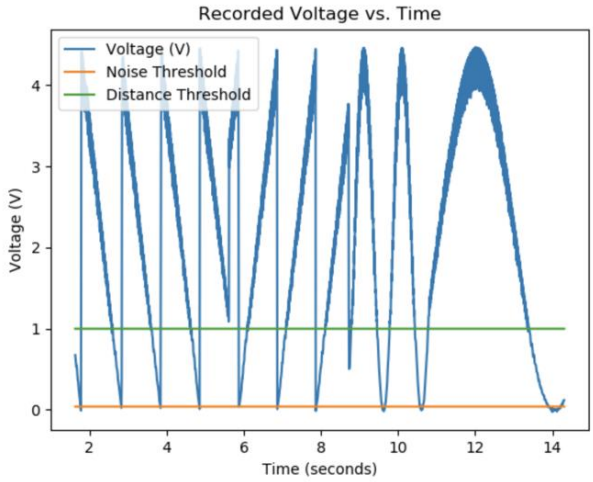

Figure 1.7.5: Graph of Variable Waveform Test

1.7.2.2 LDC Results

The first step to proceeding with the LDC design based on a CCS will be to characterize the specific NMOS 2N7000 transistor that will be used. Then, the simple constant current source can be designed and implemented. Using a standard NMOS transistor characterization process, a physical NMOS 2N7000 was characterized. The resulting data from this procedure was loaded into MATLAB and used to produce Figure 1.7.6.

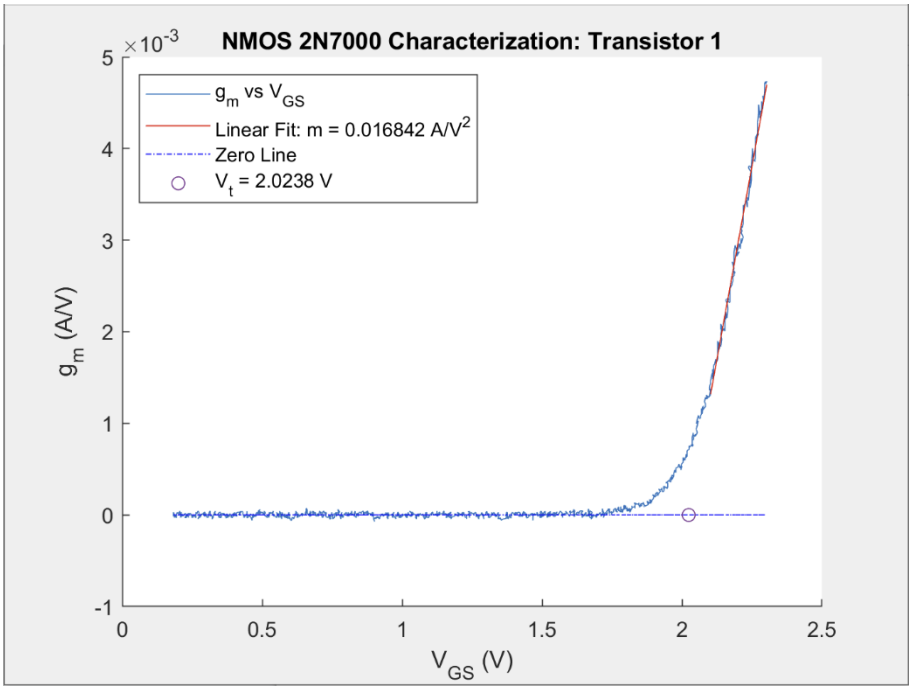

Figure 1.7.6: NMOS 2N7000 Transistor Characterization

In this Figure 1.7.6, g_m represents the transconductance of the transistor and V_t is the threshold voltage. Both of these values are necessary to estimate certain transistor characteristics that can be used in calculations to finalize the CCS design. In order to physically implement the simulated CCS which produced desirable results, updated component values were calculated using MATLAB with the following equation for the drain current in an NMOS transistor acting in the active region:

$$I_D = \frac{k_n'}{2}\frac{W}{L}(V_{GS} - V_{Tn})^2$$

Using this classic transistor equation, various voltages can be manipulated by changing the value of the source resistor. The newly calculated source resistor value was around 50 Ω. Using this value, the circuit was implemented onto a breadboard and tested using the Analog Discovery Device 2 and its corresponding software Waveforms. In order to mimic the DC sweep shown in Multisim, a ramp waveform depicted in Figure 1.7.7 (Left) was used with the breadboard circuit in Figure 1.7.7 (right) to produce a similar supply voltage vs drain current plot as seen in Figure 1.7.4. The AD2 scopes were then used to measure the appropriate nodes to produce Figure 1.7.8. Unfortunately, the drain current was not near 7 mA which likely resulted from some experimental error during the NMOS characterization process. Adjusting the source resistor value until a magnitude near 7 mA for the drain current was seen led to a source resistance of 105 Ω with Transistor 1. Exporting the data and using MATLAB to generate the plot, Figure 1.7.9 was produced and shows desirable behavior for the LDC. Transistor 2 with its different values was producing much different results, and transistor 1 had some variation in repeated measurements due to components shifting in the breadboard. At this point, it was decided to implement the simple constant current source onto a prototype board in order to remove this variation and perform further validation. For the sake of brevity, the many plots generated and small changes in source resistance to get to this point are not included. Figure 1.7.10 depicts the simple constant current source design implemented onto the protoboard.

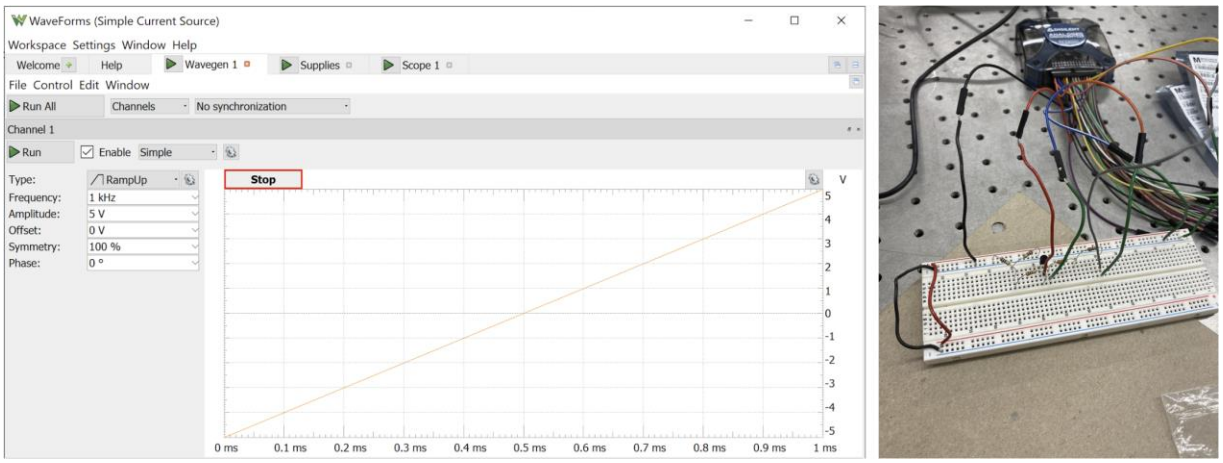

Figure 1.7.7: Simple Constant Current Source – Ramp Signal and Breadboard Setup

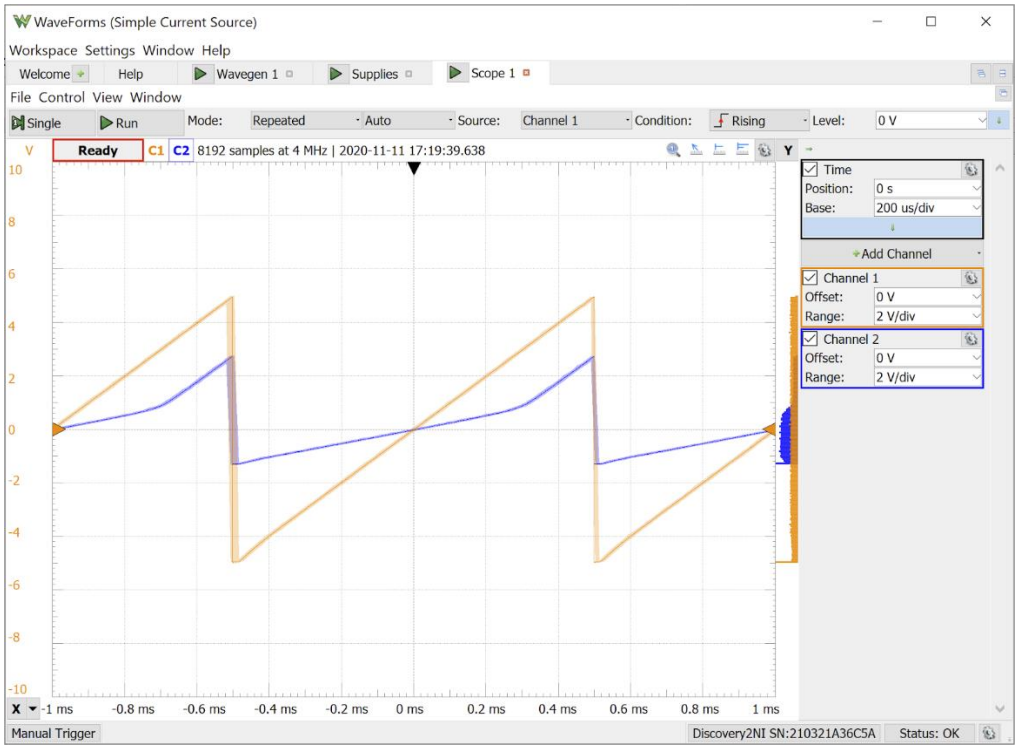

Figure 1.7.8: Simple Constant Current Source Ramp Waveforms from Scopes

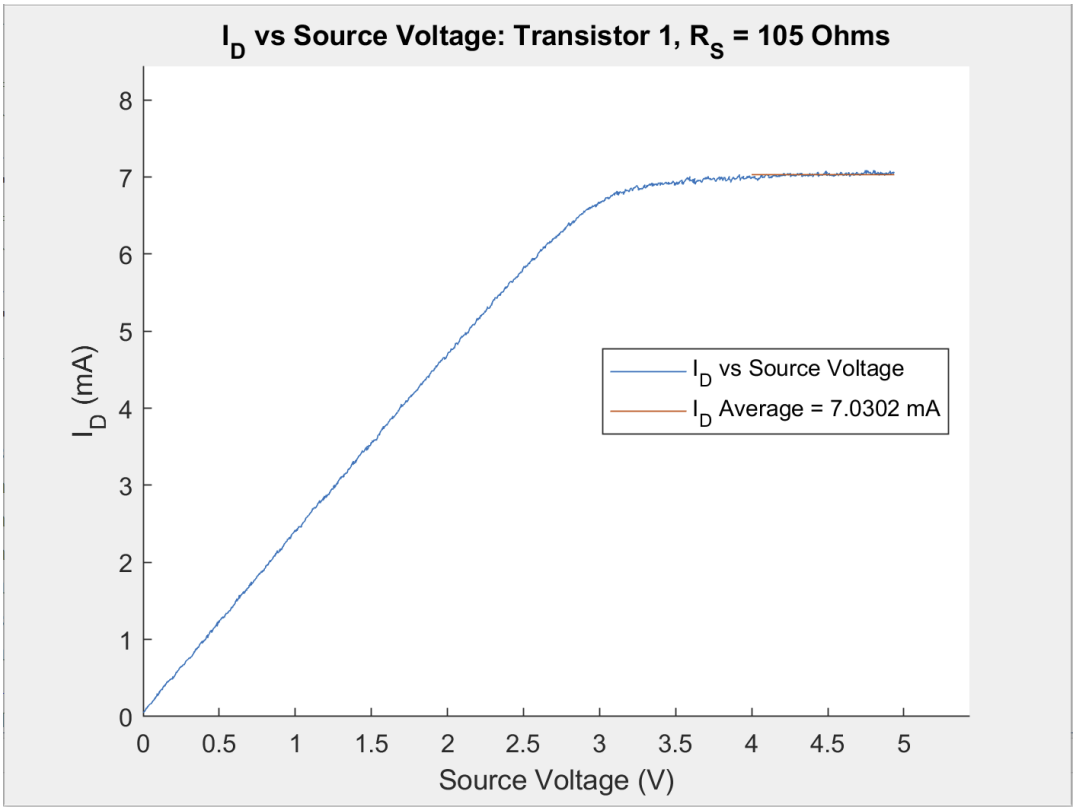

Figure 1.7.9: Breadboard Results for Simple Constant Current Source

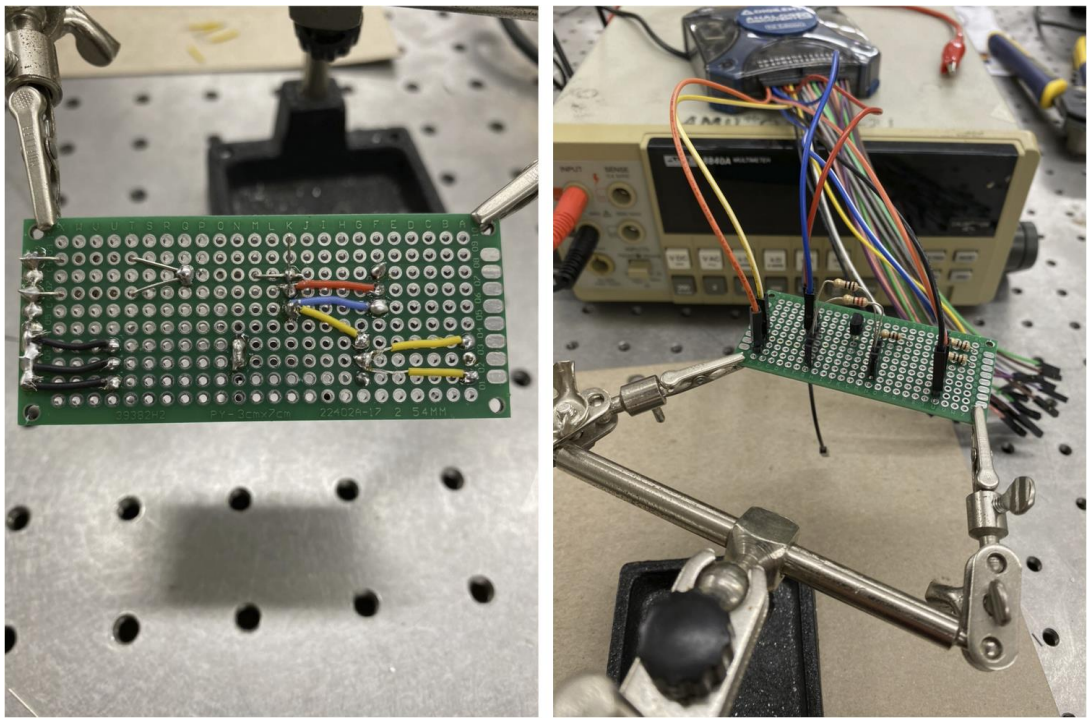

Figure 1.7.10: Simple Constant Current Source Implemented on Protoboard

By the time the simple constant current source was implemented on the protoboard, the optical path subsystem validation finalized the requirements for the LDC. Distance measurements produced results which showed little variation with a lab test equipment derived constant current of 6 mA – 8 mA. This solidifies the fact that the LDC can simply provide a current within this range that is able to stay within this range depending on variations in voltage supplies. This is further explained in the 1.7. Evidently, the simple constant current source circuit design will likely be sufficient for the requirements needed for the LDC based on insight gained from the breadboarding process. Therefore, the simple current source was brought to the validation phase to confirm this. Other LDC CCS designs will only be considered if this design is not sufficient.

The validation process performed on the simple constant current source implemented on a protoboard depicted in Figure 1.7.10 included the following:

1. Running a ramp signal through the supply voltage of the design as shown in Figure 1.7.7 to produce a plot similar to Figure 1.7.9 with a load resistance of 320 Ω.
2. Running a Square Wave at the supply voltage to simulate the LDC being turned on and off. This step will be performed for load resistance values of 220 Ω, 267 Ω, and 320 Ω to simulate the min, middle, and max voltage drops corresponding to the forward voltage range of the VCSEL diode at the target drive current of 7 mA.

These validations sufficiently exemplify the conditions the LDC will be under when providing the current to the optical path subsystem. They incorporate variations in load forward voltage, variations in supply voltage, and conditions when the LDC is being turned on and off. The waveforms mentioned in steps 1 and 2 are depicted in Figure 1.7.11. When running these waveforms, the scopes produce measurements that are exported to MATLAB to have the

corresponding figures produced. Figure 1.7.12 and 1.7.13 depict the results of applying the aforementioned waveforms to the simple constant current source implemented on the protoboard.

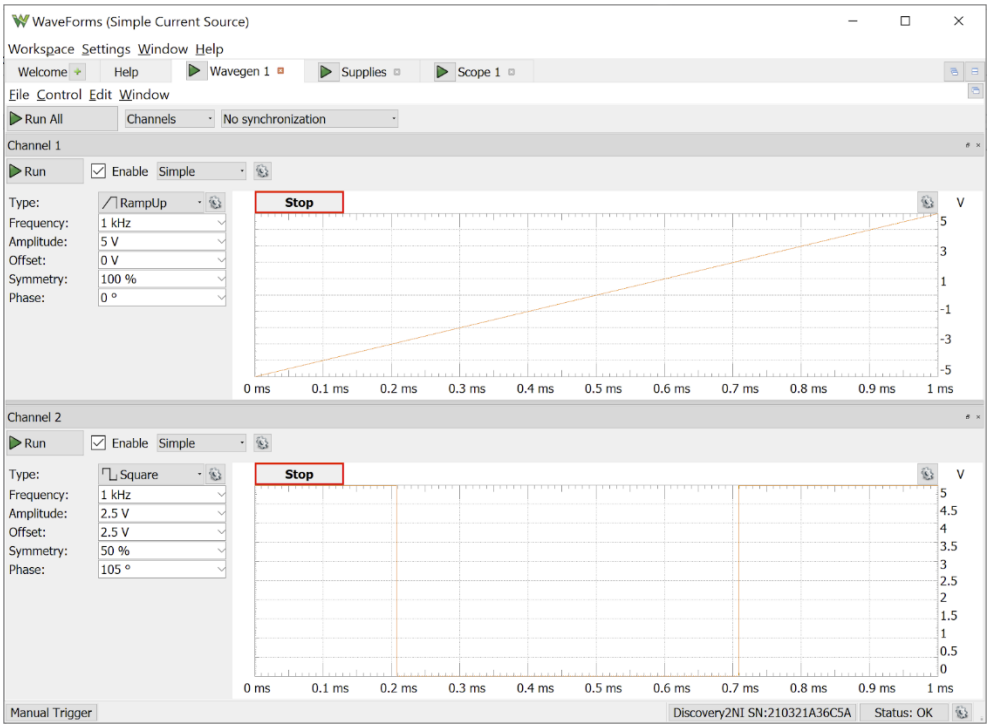

Figure 1.7.11: Simple Constant Current Source Validation Waveforms

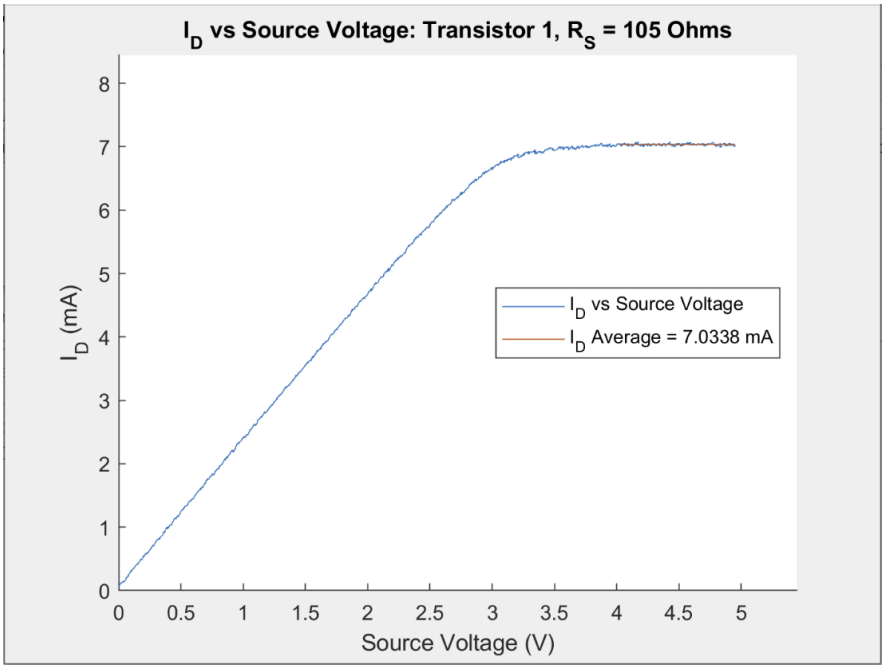

Figure 1.7.12: Protoboard Simple Constant Current Source Ramp Response

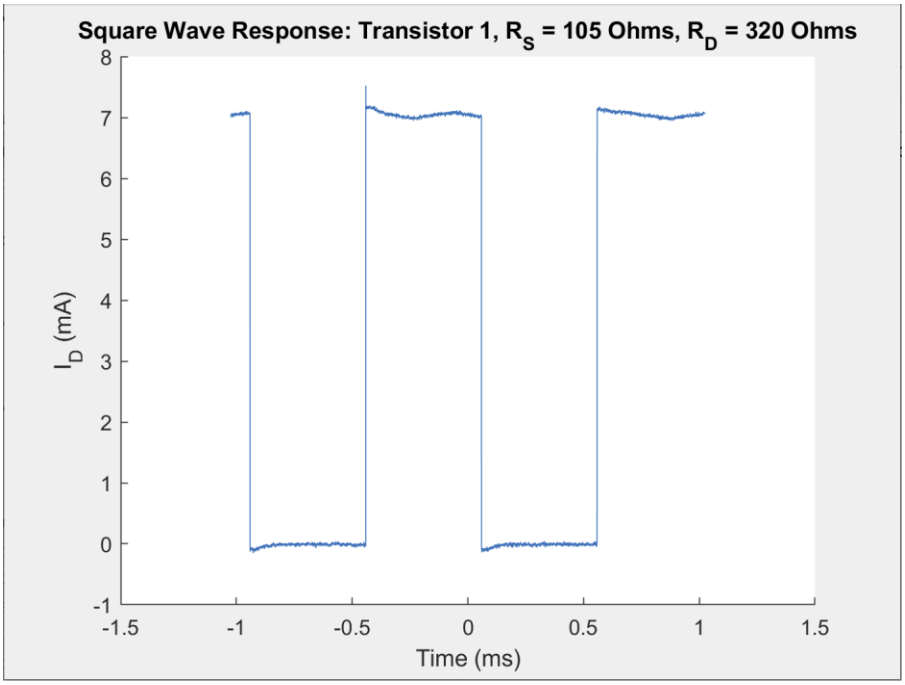

Figure 1.7.13: Protoboard Simple Constant Current Source Square Wave Response – 320 Ohms

Note: that all the validation instances depict an output LDC drive current near 7 mA that never exits the range of 6 mA – 8 mA despite supply voltage variations and the LDC being turned On and Off.

1.7.3 Link Communication Subsystem Conclusions

1.7.3.1 ADC Conclusions

As shown by the Discrete DC Voltage and Continuous Waveform tests, the ADC complies with all requirements and expectations established. It can measure with minimal error distinct values when averaged over time and can track a continuous input to trigger an LED upon the crossing of a set threshold value.

1.7.3.2 LDC Conclusions

The expected drive current from the link communication subsystem's laser diode controller need only fall within the range of 6 mA – 8 mA to fall under the validated range of measurements from the optical path subsystem. As long as the current is not sustained

continuously at a value above 12 mA, the VCSEL diode will not be harmed. That being said, even drive currents between 8 mA – 12 mA, which will produce higher measured voltages and thus still be distinguishable from noise, would be acceptable.

Based on this information, the validated results shown in Figures 1.6.12-1.6.13 verify the successful operation of the simple constant current source LDC implemented on the protoboard. As depicted in these figures, this circuit produces a sufficient drive current value close to 7 mA that stays within the range of 6 mA – 8 mA despite changes in forward load voltage, variations in the supply voltages, and during the process of being turned on and off. Therefore, this LDC is sufficient to be used in the interfaces with the optical path subsystems to supply a drive current to the VCSEL diode. An additional benefit of this circuit is its relatively simple and cheap design which would improve the manufacturability of the overall system and reduce costs.

2. METHODS

With the subsystems designed and validated, the integration of the subsystems is the subsequent phase. Methods leading to the completion of this phase are outlined in the following sections, with their results being included in the Results section. After subsystem integration, system level validation will be conducted to verify the system meets all defined requirements. Also, specific system capabilities and limitations will be thoroughly defined, tested, and validated.

2.1 Module Connectivity and Power Up

Module Connectivity and Power Up consists of the physical integration of the various subsystems on to both the stationary base module and the mobile module (as defined in figure 1.3.1 in the System Overview section). This phase is critical to setting the stage for system level tests and validations as all physical components must be integrated onto their respective module and retested before software level integration can begin. Such tests and procedures are outlined in the following sections and include physical component mounting, electrical wire connection, and power supply verification.

2.1.1 Stationary Base Module

The stationary base module acts as the transmitting component of the system, as depicted and described in Figure 1.3.1 and section 1.3. This module contains a physically constructed base which facilitates the range of movements necessary for the motors to be able to scan the whole steradian application range. This base structure is pictured in Figure 2.1.1 (left). Attached to the structure are the motors, gears, and motor drivers as described in section 1.4. The stationary base module also contains a Raspberry Pi to act as the brain of the device by controlling all of the

components. In order to facilitate alignment, the stationary base module contains a Raspberry Pi Camera to locate the mobile module and an LED Tracking Target to be recognized by the mobile module's equivalent Raspberry Pi Camera (as described in section 1.5). Finally, the stationary base module contains the VCSEL and LDC which are used to control and emit the transmitting beam to form the RSL (as described in sections 1.6 and 1.7). All of the aforementioned components were connected to the base structure and are pictured in Figure 2.1.1 (right). Each of these components were individually connected, tested, and validated as described in the following sections with Results included in the Results section.

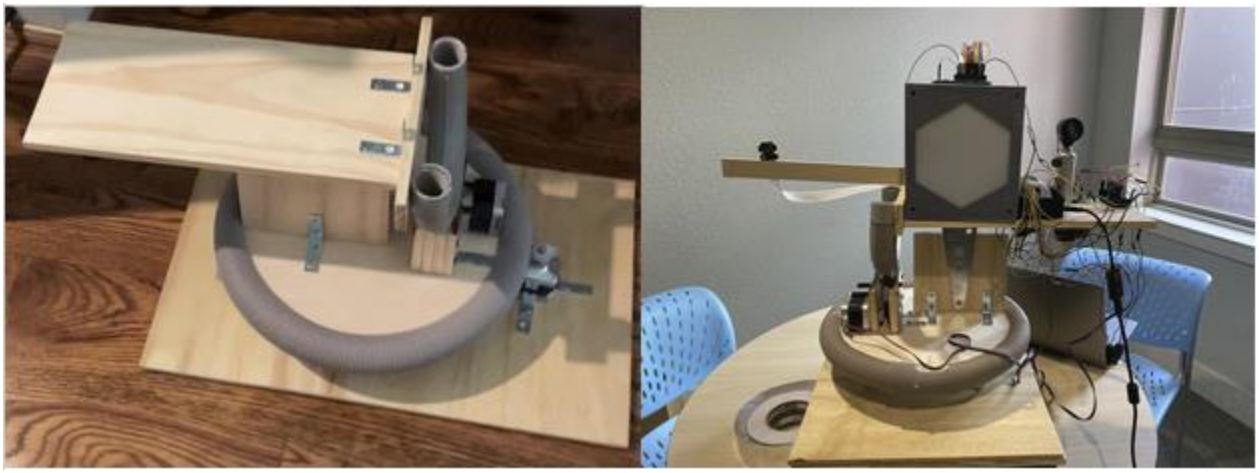

Figure 2.1.1: Stationary Base Module – Base Structure and Integrated Physical Components

2.1.1.1 Raspberry Pi and Pi Camera

Space constraints on the modules necessitated careful planning in the placement of the Raspberry Pi board and camera. On the stationary module, the board is centered directly between the tracking target and the VCSEL diode. This middle location grants all powered electronics easy access to their respective GPIO pins needed for controls and power. The Pi camera is placed on an arm extending from the module. This allows the photodetector on the mobile module and the VCSEL diode on the stationary module to physically be aligned when the tracking target of

the mobile module is aligned in the center frame of the stationary Pi camera. Both the Raspberry Pi board and camera are shown in Figure 2.1.1 (right).

The stationary Raspberry Pi is responsible for providing power to the VCSEL diode and LDC and will be powered by a wall outlet. This was tested after the stationary module was physically integrated and assembled by powering the Pi and confirming that the VCSEL diode, LDC and stepper motors activated.

Before any control algorithms could be tested, the stationary Pi had to be updated and equipped with the most current versions of Python 3 and the Open CV, Adafruit 1x115, and Pandas libraries. Following the updates, control of the LED tracking target, camera, stepper motors, VCSEL diode, and LDC was tested by running code on the Pi written for each independent component. Each component is controlled by a different set of GPIO pins varying based on required inputs. For example, the motor drivers require 25 GPIO pins for control while the LED tracking target only requires 1. Each of these pins is referenced and initialized in code on the Pi. Proper functionality would be verified by the expected behavior of each independent component. Finally, once fully assembled and physically placed, the independent functionality of each component was tested once more to verify that the module placement did not interfere with the independent functionality.

2.1.1.2 Motors, Motor Drivers, and Motor Protoboard

After the connection of the tracking target, VCSEL, VCSEL mounting hardware, power protoboard, motor drivers, Raspberry Pi, and LDC, the stationary base module adopted a substantially heavier load. This load led to the need for retesting of the module's accuracy, which is further defined below.

The stationary base module's capability to land on a coordinate with the new load shall be verified in order for the system to maintain the highest degree of accuracy possible. The past version of the coordinate tracking software shall be run on the stationary base module to ensure that the module still functions as anticipated.

The stationary base module's ability to perform a 180 degree rotational sweep and 90 degree tilting sweep shall be performed in order to show that the module is still capable of sweeping a room and stopping at the target opposing it.

The motor drivers' and stepper motors' ability to be fully powered from wall voltage shall be assessed in order to certify that the system can operate with the needed level of power. Furthermore, successful power connection to the motor protoboard shall be examined for an optimization of cabling.

2.1.1.3 LED Tracking Target

The LED Tracking Target contains both the green backlit hexagon as well as the blue feedback LED which will facilitate the module search subsystem tracking functionality as described in section 1.5.

The LED tracking target was mounted near the center of the main platform on the stationary base module as pictured in Figure 2.1.1. This location was chosen to permit the proper placement of the VCSEL and the Raspberry Pi as well as to align the target nearly across from the Raspberry Pi Camera of the mobile module when both modules are aligned.

In order to verify that the LED Tracking Target was properly connected and has maintained its functionality through integration onto the stationary base module, a validation test will be performed. Using the Raspberry Pi to control the relevant GPIO pins and a wall 5V power supply, the LED tracking target will first have its green hexagon illuminated independent

of the blue LED. Then, when given a separate command through the Raspberry Pi, the blue feedback LED will turn on. Finally, both will demonstrate the ability to turn off. The results of this test will be included in the Results section.

2.1.1.4 VCSEL and LDC

The VCSEL and LDC combination connect to the Raspberry Pi which controls and powers them to produce the transmitting optical beam. Alternatively, the 5 V power supply can be used to supply the voltage for the LDC. As mentioned in sections 1.6 and 1.7, the current requirements of the VCSEL and LDC are quite low, so either option is fine.

The VCSEL and LDC were mounted adjacent to the Raspberry Pi on the right side of the stationary base module platform. The VCSEL placement was important: when both modules are perfectly aligned, the beam should inherently point at the central location of the PD X-Y axis frame. This will allow for corrective degrees of error in every X-Y direction. The resulting mounting of the VCSEL and LDC is depicted in Figure 2.1.2. Note that the optomechanical hardware mounts permit vertical and horizontal adjustments, which may be necessary during additional distance and alignment testing in subsequent sections.

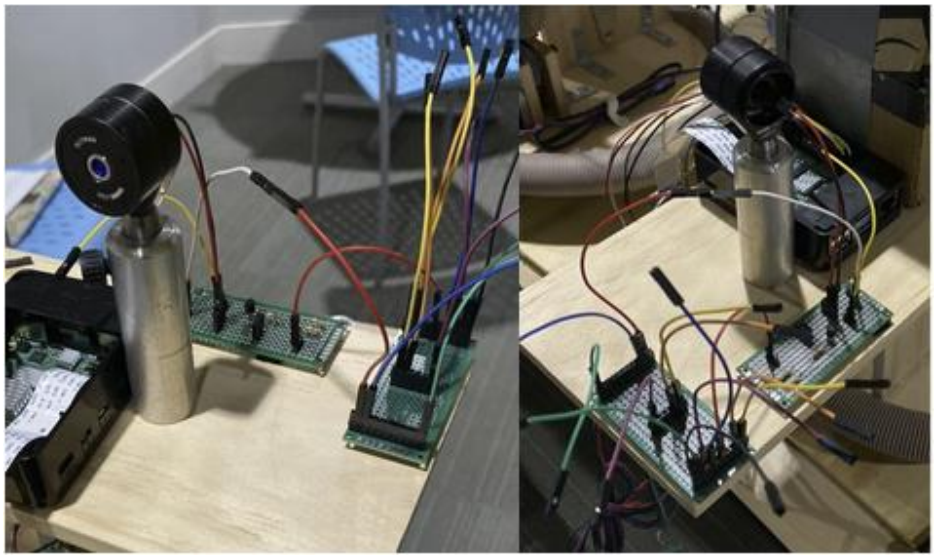

Figure 2.1.2: Mounting of VCSEL and LDC on Stationary Base Module

In order to verify that the VCSEL and LDC were properly connected and have maintained their functionality through integration onto the stationary base module, a validation test will be performed. Using the Raspberry Pi to control the relevant GPIO pins and a wall 5V power supply, the LDC will be turned on and off. This will be visually verified by using an infrared sensor card. The results of this test are included in the Results section.

2.1.2 Mobile Module

The mobile module acts as the receiving component of the system, as depicted and described in Figure 1.3.1 and section 1.3. This module contains a physically constructed base which facilitates the range of movements necessary for the motors to be able to scan the whole steradian application range. Also, the base structure contains an X-Y frame which enables the adjustment of the PD to facilitate the establishment of a RSL. This base structure is pictured in Figure 2.1.3 (left). Attached to the structure are the motors, gears, and motor drivers as described in section 1.4. The mobile module also contains a Raspberry Pi to act as the brain of the device by controlling all of the components. In order to facilitate alignment, the mobile module contains a Raspberry Pi Camera to locate the mobile module and an LED Tracking Target to be recognized by the stationary base module's equivalent Raspberry Pi Camera (as described in section 1.5). Finally, the mobile module contains the PD, PD operating circuit, and ADC which are used to detect and measure incident optical power on the PD. These components permit the distinguishment of the VCSEL beam from ambient noise (as described in sections 1.3, 1.6, and 1.7). All of the aforementioned components were connected to the base structure and are pictured in Figure 2.1.3 (right). Each of these components were individually connected, tested, and validated as described in the following sections with Results included in the Results section.

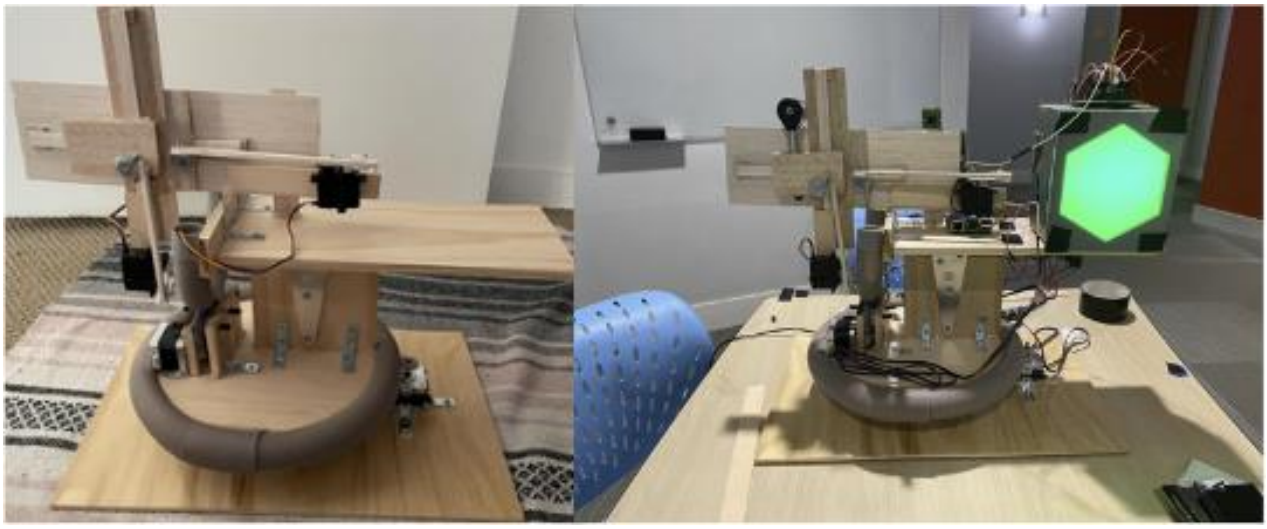

Figure 2.1.3: Mobile Module – Base Structure and Integrated Physical Components

2.1.2.1 Raspberry Pi and Pi Camera

Similar to the stationary module, significant space constraints imposed restrictions on the placement of components. The mobile module board is centered on the tilting platform and tucked under the XY axis in an unobtrusive location that places GPIOs and power within wireable reach of components. The Pi camera's location directly beside the XY axis is motivated by similar rationale as the stationary module. When the opposite tracking target is physically centered in the camera center frame, the photodetector and VCSEL diode are physically aligned. This placement is shown in Figure 2.1.3 (right).

The mobile module Raspberry Pi is responsible for providing power to the photodetector and ADC and will be powered by a portable 5 V battery. This portable battery will also power the servo motors of the X-Y axis and the tracking target. This was tested after assembly first by powering the Pi via a wall outlet and later with the portable 5 V battery.

Like the stationary module, the mobile Pi had to undergo updates to Python 3 and the Open CV, Adafruit 1x115, and Pandas libraries. The mobile module controls an LED tracking target, camera, stepper motors, servo motors, photodetector, and ADC with physical GPIO pins

initialized in code. Running each component's code first independently of physical placement and then again once integrated onto the module tested first functionality and subsequently that modular placement did not invalidate the shown capabilities.

2.1.2.2 Motors, Motor Drivers, Motor Protoboard, and Batteries

The load contribution on the mobile module system also increased significantly after the addition of the tracking target, photodiode, photodiode hardware, power protoboard, X-Y axis frame, motor drivers, Raspberry Pi, and ADC. Following the stationary module, the retesting of the mobile module was also necessary in ensuring mirrored accuracy of the overall system. Further description of the required testing is detailed below.

Similarly to the stationary module, the previous coordinate targeting software from the subsystem design section shall be used to test the mobile module's capacity to move towards a provided coordinate with a heavier load. Given that the load of the mobile module is heavier than that of the stationary module, adjustments may need to be made to the system metrics.

Following the stationary module, the mobile module shall also be capable of performing a 180 degree rotational sweep and 90 degree tilting sweep until the target is acquired on the opposite side.

The servo motors shall be capable of performing corrective grid-like motions while maintaining the load of the photodiode. The level of accuracy must be held to the same standard, even with the additional load.

The mobile module shall be capable of being powered by a mobile source(s). Devices that require such powering, with respect to the motor control subsystem, include the stepper motors, motor drivers, and servo motors. The approach of a lithium-ion polymer battery, as shown in Fig. 2.1.4, will be used to power the motor drivers and stepper motors with a constant

level of power. Contrastingly, a traditional rechargeable battery will be used to power the servo motors on the X-Y axis frame (as mentioned in the previous section as a portable 5 V battery).

Figure 2.1.4: Lithium-Ion Polymer Battery

2.1.2.3 LED Tracking Target

The LED Tracking Target contains both the green backlit hexagon as well as the blue feedback LED which will facilitate the module search subsystem tracking functionality as described in section 1.5.

The LED tracking target was mounted all the way to the right on the mobile module as pictured in Figure 2.1.3. This location was chosen mostly due to space limitations on the mobile module platform due to the X-Y axis frame. Placing it here permitted the use of the remaining space for the other components. In order to align the target nearly across from the Raspberry Pi Camera of the stationary base module when both modules are aligned, an arm extension for the Raspberry Pi Camera had to be added to the stationary base module as pictured in Figure 2.1.1.

In order to verify that the LED Tracking Target was properly connected and has maintained its functionality through integration onto the mobile module, a validation test will be performed. Using the Raspberry Pi to control the relevant GPIO pins and a wall 5V power supply, the LED tracking target will first have its green hexagon illuminated independent of the blue LED. Then, when given a separate command through the Raspberry Pi, the blue feedback LED will turn on. Finally, both will demonstrate the ability to turn off. The results of this test will be included in the Results section.

2.1.2.4 PD, PD Operating Circuit, and ADC

The PD, PD operating circuit, and ADC are used to measure input optical power on the PD and are connected to the Raspberry Pi to determine when the VCSEL beam is incident on the PD and to distinguish it from ambient noise (as described in sections 1.6 and 1.7).

In order to facilitate the proper use of the X-Y axis frame on the mobile module, the PD was directly attached to the main moving plane on the front side. The PD operating circuit and ADC protoboard were mounted on the backside of the X-Y axis away from any moving parts. This enabled the circuits to be in close proximity to the PD and the Raspberry Pi. Note: an optomechanical one inch diameter lens tube (from Thorlabs) was fixed to the back of the PD mount to protect the diode pins and solder joints during movement of the module and X-Y axis. The mounting of these components onto the mobile module is depicted in Figure 2.1.5. To confirm the functionality of these mounting locations, the X-Y axis frame will run its full range of motion to verify that no components are limiting the movement or losing functionality. The results of this test will be included in the Results section.

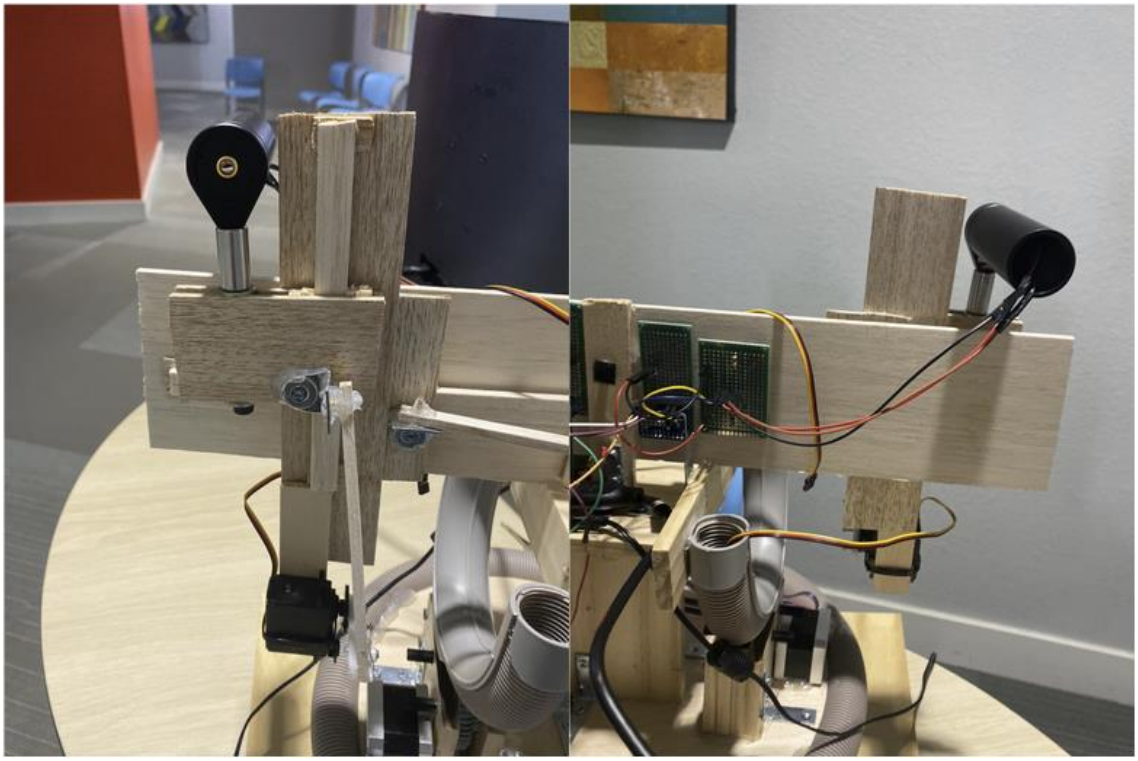

Figure 2.1.5: Mounting of PD, PD Operating Circuit, and ADC on Mobile Module

In order to verify that the PD, PD operating circuit, and ADC were properly connected and have maintained their functionality through integration onto the mobile module, a validation test will be performed. Using the Raspberry Pi to control the relevant GPIO pins and supply power to the ADC, a sample light source (cell phone LED) will be waved in front of the PD while a test Raspberry Pi program is measuring and recording voltages using the PD operating circuit and the ADC. The results of this test are included in the Results section.

2.2 Module Location and Alignment

Module Location and Alignment consists of developing and implementing the necessary algorithms in code for both the Stationary Module and Mobile Module to align themselves with one another using their tracking targets and Raspberry Pi Cameras. This phase also includes any additional hardware updates to the modules necessary to facilitate this process. Following these

updates, the functionality of the modules to locate and align with one another will be tested, the methods by which will be included in this section while the results will be included in section 3.2. The algorithms implemented and tested for Module Location and Alignment follow the explanations given in section 1.5 for the Module Search Subsystem and include any necessary updates.

2.2.1 Module Location and Alignment Algorithms

Following the algorithms and functionality mentioned in section 1.5, the modules must be able to perform the following actions to satisfy the requirements of Module Location and Alignment:

1. Modules can rotate and scan steradian space
2. Modules can locate and identify the other module's tracking target
3. Modules can determine necessary spherical coordinate information (z, phi, theta) from tracking targets and align accordingly

In order to satisfy these requirements, several processes needed to be implemented in code on the Raspberry Pi of each module. These processes are best described through the use of flow charts, some of which were included in section 1.5. These will be updated and repeated here. Figure 2.2.1 describes the overall location and alignment process. Figure 2.2.2 describes the sweeping process in detail. Figure 2.2.3 explains the process by which the OpenCV is used to analyze the mask and recognize the tracking target. Finally, Figure 2.2.4 outlines the process by which the spherical coordinates are calculated to direct the motors towards alignment.

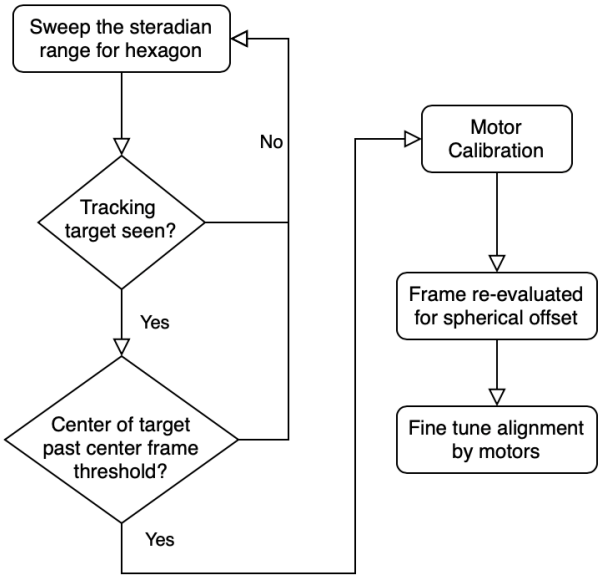

Figure 2.2.1: Module Location and Alignment Overall Process

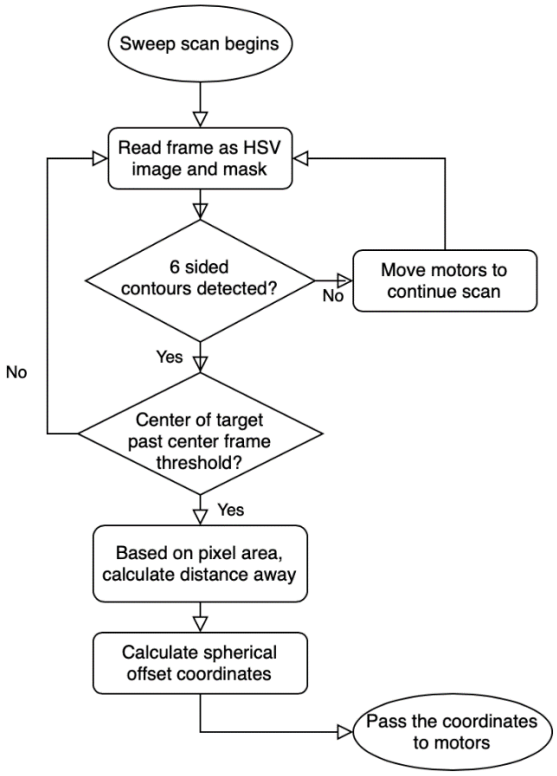

Figure 2.2.2: Module Location and Alignment Sweep Process

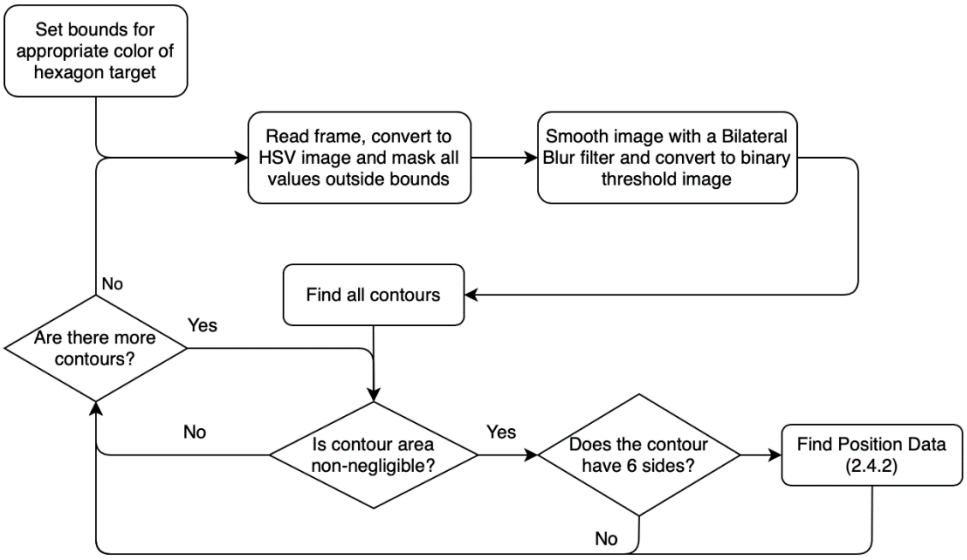

Figure 2.2.3: Module Location and Alignment Tracking Target Recognition Process

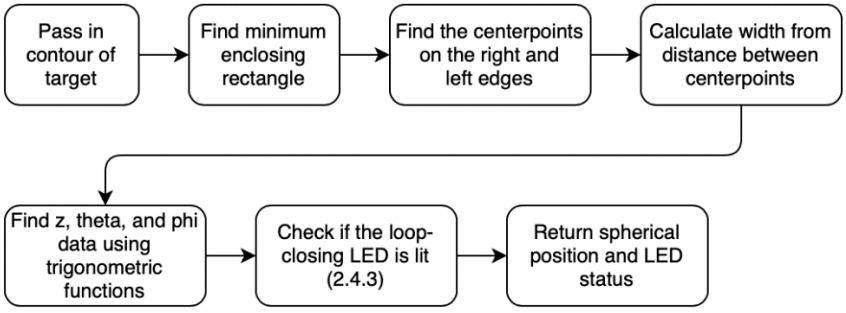

Figure 2.2.4: Module Location and Alignment Spherical Coordinate Calculation Process

2.2.2 Raspberry Pi Camera Mounting Updates

During the Module Connectivity and Power Up phase, the Raspberry Pi Cameras were mounted on each module in order to be centered with respect to the opposite module's tracking target. However, this was a preliminary mounting and will likely need updating. As the functionality described in section 2.2.1 is implemented, any discovered necessary changes to the

Raspberry Pi Camera mounting on each module will be made and outlined in section 3.2.2 of the Results section.

2.2.3 Module Location and Alignment Testing

Once the necessary code of section 2.2.1 and physical changes of section 2.2.2 have been completed, the Module Location and Alignment functionality needs to be tested and verified. For the operational range of one to ten meters, this will constitute tests at 1, 5, and 10 meters for each module. For each of these tests, only one module's location and alignment code will be running, and the other module will only have its tracking target on. The other module will be located in a random location within the module under test's steradian range. The time needed for alignment will be noted to provide insight into future functionality of the system. The results of these tests will be displayed in section 3.2.3 of the Results Section.

2.3 Establishing RSL and Inter-Module Power Transfer

The Establishing RSL and Inter-Module Power Transfer phase concerns three major components. The first is confirming the beam characteristics of the collimated VCSEL mounted on the Stationary Module. Next, the optical path distance measurements completed in section 1.6 need to be reproduced for the integrated system. This also includes updating the physical mounting and alignment of the VCSEL optomechanical mount with respect to other Stationary Module components. Finally, the feedback mechanisms and remaining processes leading up to establishing the Representative Stationary Link (RSL) need to be implemented in code. Following these components, the functionality of the Establishing RSL and Inter-Module Power Transfer phase will be tested, the methods by which will be included in this section while the results will be included in section 3.3.

2.3.1 VCSEL Beam Check

Since attaching the VCSEL diode and collimating lens to the Stationary Module using optomechanical mounts, it is possible that the beam characteristics determined in section 1.6 regarding the collimated VCSEL beam pattern and the distance-dependent measured voltages by the PD on the Mobile Module have changed. Therefore, both of these measurements need to be confirmed. In this section, the VCSEL beam will be recollimated and its beam characteristics at 10 meters will be examined. Primarily, the beam pattern, differences between an aligned beam and ambient noise, and the differences between the 5V wall power supply and the Raspberry Pi's 5V supply pin powering the LDC will be examined. The setup and results of these examinations will be included in the Results section in section 3.3.1.

2.3.2 Distance Measurements and Physical Alignment

After the recollimation and measurements completed in section 2.3.1, it will be necessary to conduct distance measurements throughout the 1-to-10-meter operational range to determine the updated range of distance-dependent and alignment-dependent measured voltages of the VCSEL beam by the PD on the Mobile Module. Moreover, the physical mounting and alignment of the VCSEL optomechanical mount with respect to other Stationary Module components needs to be updated as mentioned is section 2.1. Therefore, at each measurement distance, the VCSEL optomechanical mount will be physically adjusted such that the VCSEL beam is directly incident on the manually aligned Mobile Module's PD when the PD is in the center of the X-Y axis' range of motion. Then, with the Mobile Module recording the measured voltages, the X-Y axis will sweep left, back to middle, right, back to middle, up, back to middle, down, and back to middle. This will provide a range of measured voltages at each distance which correspond to varying levels of alignment. Finally, the Stationary Module will use its Raspberry Pi Camera to

measure the width of the hexagon on the Mobile Module's tracking target in order to update the pixel-width vs distance measurements. The setup and results of these measurements are included in the Results section in section 3.3.2.

2.3.3 Establishing RSL Feedback Algorithm

Following the algorithms and functionality mentioned in section 1.5, the modules must be able to perform the following actions to satisfy the feedback requirements for establishing a RSL:

1. Stationary Module turns on VCSEL beam and feedback blue LED after it completes its alignment
2. Mobile Module recognizes the Stationary Module's feedback blue LED and begins monitoring PD measured voltages and moves PD X-Y axis accordingly after alignment
3. Mobile Module is able to locate and distinguish VCSEL beam from ambient noise and turns on its own feedback blue LED once the PD has found and aligned itself with the VCSEL beam
4. Stationary Module recognizes the feedback blue LED of the Mobile Module signifying that a RSL has been established.

In order to satisfy these requirements, several processes needed to be implemented in code on the Raspberry Pi of each module. These processes are best described through the use of a flow chart. Figure 2.3.1 describes the overall feedback process between the modules that is needed to establish a RSL.

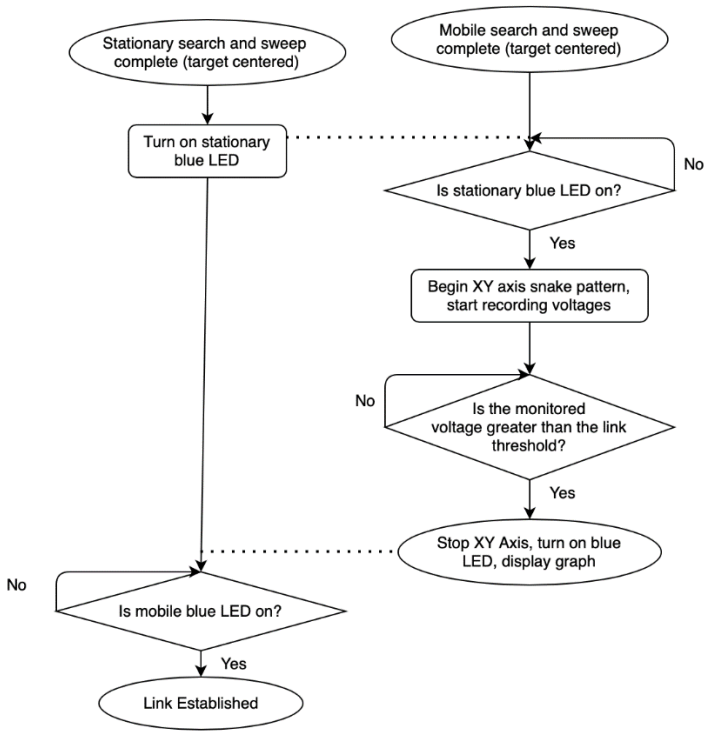

Figure 2.3.1: Establishing RSL Feedback Process

2.3.4 Establishing RSL and Inter-Module Power Transfer Test

Following the implementation of the code outline in section 2.3.3, the functionality will be tested. At a distance of 1 meter, the Stationary Module and Mobile Module will complete the full process of establishing a RSL verifying that the beam is incident on the PD and that all feedback mechanisms activated at only the correct times and were recognized by the opposite module appropriately. The results of this test will be included in the Results section in section 3.3.4.

2.4 Restoring a Broken RSL

The Restoring a Broken RSL phase involves implementing functionality to ensure the robust establishment of an initial RSL and then introduce functionality by which to restore a broken RSL. As mandated by the system description outlined in section 1.3, the modules must be

able to restore a broken RSL after mobile module movement. According to the scope and operational description of the system as described in sections 1.1, the system does not need to establish or restore a broken RSL in the event that an obstacle is left in the optical path for an extended period of time. However, an obstacle temporarily breaking the RSL and then being removed will be addressed by enabling the modules to restore the broken link. These processes can be implemented in code by following the processes outlined in the flow chart depicted in Figure 2.4.1. The processes depicted in this figure will be tested with the methods being in the subsequent sections and the results included in section 3.4.

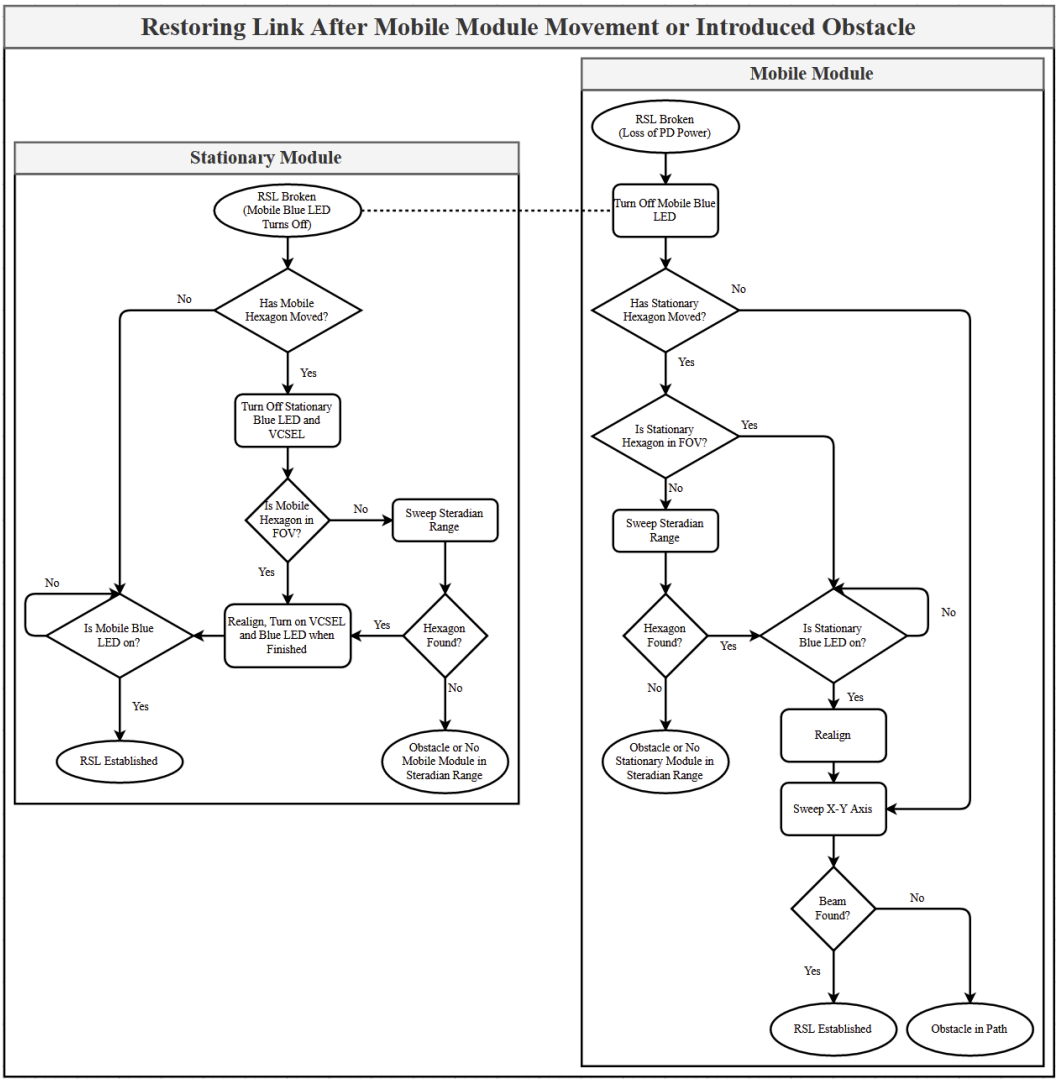

Figure 2.4.1: Restoring a Broken RSL Process

2.4.1 Failure Propagation

Figure 2.4.1 contains several processes which can lead to error messages signaling a failure to restore a RSL. Functionally, these processes entail checking certain cases where it is impossible to restore the RSL in the scope of the system. One such case involves sweeping the entire steradian range and not finding any tracking target, meaning there was no other module and an empty steradian range. Another case involves the PD being snaked through the entire X-Y axis range of motion on the Mobile module without finding any VCSEL beam. These cases are also important to identifying failures in the initial establishment of the RSL. As such, they will need to be implemented in code and tested.

2.4.1.1 Empty Steradian Range

When no tracking target (meaning no module) is in the steradian range of the searching module, that module's steradian range is empty. In order to prove this is the case, the searching module would have to sweep its entire steradian range with its Raspberry Pi Camera and verify that no tracking target is present. Therefore, to test for an empty steradian range, an exhaustive sweep function must be implemented in code. This requires knowledge of the Raspberry Pi Camera's horizontal and vertical field of views. Once these values are obtained, the module can be swept in each direction until the edge of the Raspberry Pi Camera's field of view touches the edge of the steradian range. As a reminder, the steradian range is defined as a full horizontal 180° and vertical 90° centered with respect to the module for an operational range of 1 to 10 meters. To ensure the empty steradian range case can be checked, the horizontal and vertical fields of view of the Raspberry Pi Camera will be determined and then functionality to sweep the steradian range will be implemented and tested. The results of this test will be included in section 3.4.1.1.

2.4.1.2 No VCSEL Beam in X-Y Axis Range

When there is no detectable VCSEL Beam in the X-Y axis range, the Mobile Module must be able to recognize the issue. This issue can be due to a persistent obstacle blocking only the beam or an error in the alignment process. This can be tested by developing code functionality to snake the PD through the entire X-Y axis range while measuring the voltages of the PD. Since the results of the distance measurements in section 3.3.2 show that the VCSEL beam is sufficiently distinguishable from ambient noise, if the PD snakes through the whole range without measuring a voltage above the link threshold value, there is no VCSEL beam to detect in that area. Code functionality to test for this case will be implemented and the results will be included in section 3.4.1.2.

2.4.2 Simultaneous Alignment

Up until this point, all alignment processes were completed with only one module doing the process at a time. In order for the system to operate as expected and described in section 1.3, the modules must be able to simultaneously align without causing location, alignment, or feedback errors. This is a key functionality to test at this point in order to move forward with the Restoring a Broken RSL phase, so tests to locate and address current errors in the code will be performed. The results of these tests will be included in section 3.4.2.

2.4.3 Restoring a RSL Temporarily Broken by an Obstacle

In the event that an obstacle temporarily breaks a RSL, both modules must be able to restore the link. To clarify, if an obstacle breaks the link and remains in the way of the optical path, both modules will recognize that the RSL has been broken. After this, as shown in Figure 2.4.1, the modules will attempt to restore the link. If the obstacle still remains and the Mobile Module is not moved, it will not be possible for the link to be restored. Therefore, if the tracking

targets are also blocked, the modules will recognize this occurrence through the Empty Steradian Range Failure Propagation mode discussed in section 2.4.1.1. If, however, the obstacle is only blocking the VCSEL beam and the tracking targets are still visible to the modules, the modules will recognize this occurrence through the No VCSEL Beam in X-Y Axis Range Failure Propagation mode discussed in section 2.4.1.2. Finally, if the obstacle is removed entirely (or the Mobile Module is moved to a location with an unobstructed path), the modules will be able to restore the link. Code functionality to test for these cases will be implemented as outlined in Figure 2.4.1 and the results will be included in section 3.4.3.

2.4.4 Restoring a RSL After Mobile Module Movement

As mentioned in sections 1.1 and 1.3, the system is defined such that the Mobile Module, as the name suggests, can be moved. Both modules must be able to recognize that the RSL has been broken (implying a potential movement of the Mobile Module) and be able to work to restore the lost RSL. Sections 1.1 and 1.3 also describe that the RSL need only be restored when the Mobile Module is moved to locations where both modules are still within one another's steradian and operational ranges. Movements to locations outside of these ranges are outside the scope of the presented system and the broken RSL will not be restored; however, covering such circumstances may only need changes to the code algorithm. Therefore, if the Mobile Module is moved properly within the steradian and operational ranges of both modules, the RSL will be restored. However, if the Mobile Module is moved outside of these ranges, the Empty Steradian Range Failure Propagation mode discussed in section 2.4.1.1 will notify the user. Code functionality to test for these cases will be implemented as outlined in Figure 2.4.1 and the results will be included in section 3.4.4.

2.5 Full Steradian and Operational Range Tests and Validation

The Full Steradian and Operational Range Tests and Validation phase consists of extending and verifying proper and consistent operation of the system throughout the entire steradian and operational range. Up until this point, system functionality for the earlier phases was tested at a distance of one meter and with only slight variation in the initial module unalignment. As mentioned in sections 1.1 and 1.3, the modules must be able to form and restore a RSL between one another whenever each module is in one another's steradian and operational range. As a reminder, the steradian range is defined as a full horizontal 180° and vertical 90° centered with respect to the module for an operational range of 1 to 10 meters. To validate system operation within the steradian and operational range, a series of tests covering the operational range at distances around one, five, and ten meters will be performed along with varying initial module unalignments corresponding to edge cases within the steradian range. At each distance, initial RSL and RSL restoration tests will be performed and the time durations for each of these RSL establishments will be recorded. The results of these tests will be included in section 3.5.

3. RESULTS

With the subsystems designed and validated, the integration of the subsystems is the subsequent phase. Methods leading to the completion of this phase are outlined in the Methods section with their results being included in the following sections. After subsystem integration, system level validation will be conducted to verify the system meets all defined requirements. Also, specific system capabilities and limitations will be thoroughly defined, tested, and validated.

3.1 Module Connectivity and Power Up

Module Connectivity and Power Up consists of the physical integration of the various subsystems on to both the stationary base module and the mobile module (as defined in figure 1.3.1 in the System Overview section). This phase is critical to setting the stage for system level tests and validations as all physical components must be integrated onto their respective module and retested before software level integration can begin. Such tests and procedures are outlined in the Methods section and include physical component mounting, electrical wire connection, and power supply verification. The results of these tests and procedures are included in the following sections.

3.1.1 Stationary Base Module

3.1.1.1 Raspberry Pi and Pi Camera

The stationary Raspberry Pi powered on when plugged into the wall outlet. Additionally, the Pi was shown to provide adequate power to the VCSEL diode and LDC both independent of physical integration and once mounted on the module.

Both independent of physical integration and after module mounting, the LED tracking target, camera, stepper motors, VCSEL diode, and LDC were each shown to behave as expected when controlled by the Pi. The LED tracking target is capable of toggling on and off based on user input representative of the command passed in the full code sequence. The camera runs with the newest version of OpenCV and can take continuous video for image processing. The stepper motors can receive calibration sequences as well as information to rotate either clockwise or counterclockwise a specified number of ticks. The VCSEL diode can be toggled on and off by the LDC given user input representative of the command passed in the full code sequence. These results verified that the Pi could digitally control the behavior of each component and granted procedure towards full algorithmic implementation and testing.

3.1.1.2 Motors, Motor Drivers, and Motor Protoboard

The stationary base module is able to accurately move to a given target with the addition of a substantial load. There appears to be no loss of accuracy during preliminary testing, but further evaluation will be performed during the software integration with the module search subsystem.

With the additional load, the stationary base module is fully capable of performing a rotating and tilting sweep motion of 180 degrees and 90 degrees, respectively, until the target is within the necessary view.

The stepper motors and motor drivers can both be sufficiently powered through the motor protoboard. The wall voltage plug of 12V/2A is sufficient in maintaining the proper amount of power for the stepper motors and motor drivers.

3.1.1.3 LED Tracking Target

Included in this section are the results for the stationary base module LED tracking target methods included in section 2.1.1.3.

The goal of the LED tracking target being centered around the Raspberry Pi camera of the mobile module when the two modules are aligned was mostly met. There is a slight vertical offset that can be corrected through slight physical adjustments (explained further in section 2.2).

The successful operation of the LED tracking target was confirmed through the execution of the test described in the Methods section. Figure 3.1.1 (top) depicts the tracking target green hexagon being independently illuminated. Figure 3.1.1 (bottom) then depicts the addition of the blue feedback LED being turned on. As depicted, both functionalities of the LED tracking target are independently operational and properly controlled by the Raspberry Pi and powered by the 5 V wall power supply.

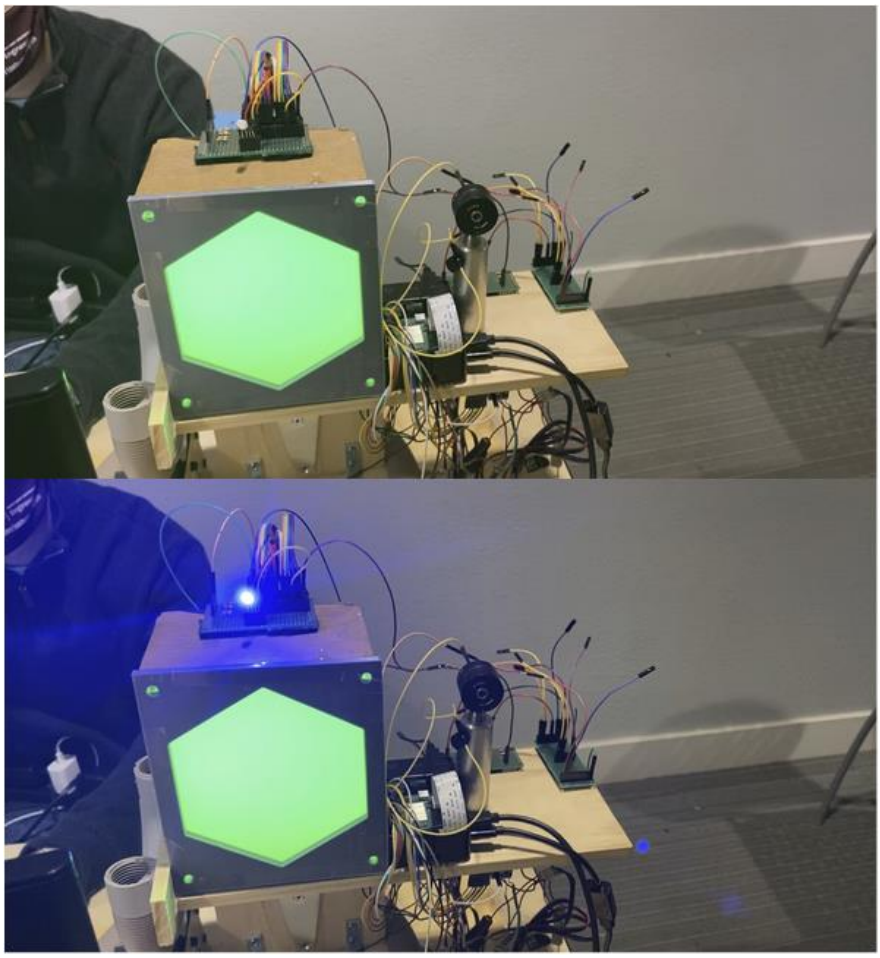

Figure 3.1.1: Stationary Base Module LED Tracking Target Connectivity and Power Up Test

3.1.1.4 VCSEL and LDC

Verification of the VCSEL diode mounting location resulting in the beam being inherently incident on the center of the PD X-Y axis when there is perfect alignment will be confirmed in section 2.3 and 3.3. This is due to the need for adjustment of the optomechanical hardware during future tests.

The successful operation of the VCSEL and LDC was confirmed through the execution of the test described in the Methods section. Figure 3.1.2 (left) depicts the VCSEL diode in the "off" state where there is no voltage applied to the gate of the LDC from the Raspberry Pi GPIO

pin. Figure 3.1.2 (right) depicts the VCSEL diode in the “on” state where the Raspberry Pi GPIO pin is supplying a gate voltage to the LDC which supplies the drive current to power the VCSEL.

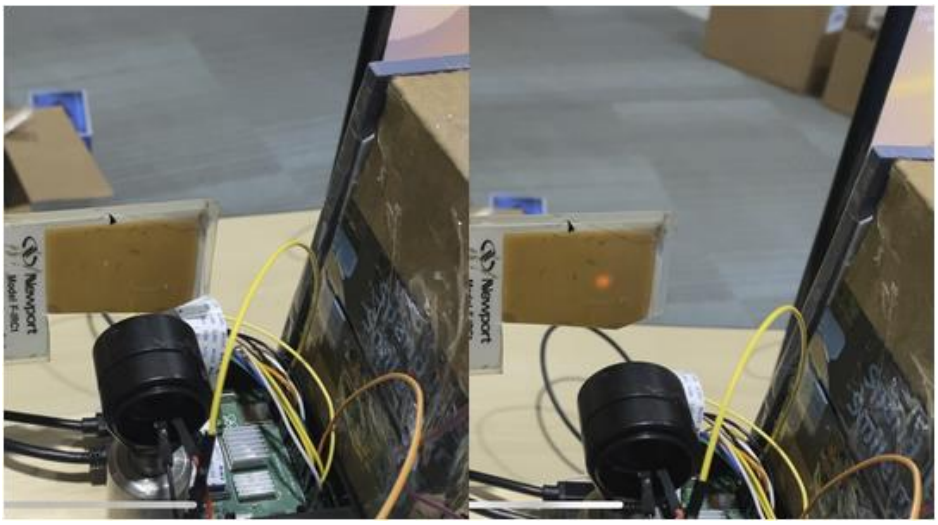

Figure 3.1.2: Stationary Base Module VCSEL and LDC Connectivity and Power Up Test

3.1.2 Mobile Module

3.1.2.1 Raspberry Pi and Pi Camera

The mobile Raspberry Pi powered on when plugged into the wall outlet. Additionally, the Pi was shown to provide adequate power to the photodetector and ADC both independent of physical integration and once mounted on the module. When using the portable 5 V battery to power the Raspberry Pi, the same results were obtained.

As described with the stationary module, the mobile Raspberry Pi was shown to control the LED tracking target, camera, stepper motors, servo motors, photodiode, and ADC both before and after physical placement on the module. The LED tracking target can toggle on and off based on user input representative of the intercode command. The camera runs the most up to date version of OpenCV and can capture video for image processing. The stepper motors can rotate clockwise and counterclockwise a given number of ticks and can receive calibration sequences. The photodiode and ADC can begin and stop measuring and recording voltages based

on user input. The behavior of each component verified that the Pi controls each component as expected even once physically on the module. These results enabled progression towards more comprehensive, system-level testing and validation.

3.1.2.2 Motors, Motor Drivers, Motor Protoboard, and Batteries

The mobile module is capable of effectively positioning towards an opposing given coordinate with the addition of a load. Initially, one of the motors was having issues with oscillating windings; the motor was replaced and the system appears to work as expected again. As with the stationary module, more testing will be performed after software integration has been incorporated.

Similarly to the stationary module, the mobile module is fully able to perform the necessary rotating and tilting motions until the target is within the proper frame. The addition of the load did not inhibit the module from maintaining its level of mobility.

The servo motors can sufficiently move in a grid-like motion after the addition of the photodiode load to the X-Y axis frame. The results for this section will deepen as the X-Y axis frame software is integrated alongside the photodiode software.

The servo motors can be sufficiently powered with a 5V/1A traditional rechargeable battery; the range of motion of the servo motors did not appear to be affected. However, the lithium-ion polymer battery DC to DC boosters depicted in Figure 2.1.4 was unable to safely power the mobile module stepper motors. This is due to the fact that the motor drivers used are not current-limited, meaning an exceedingly large amount of current ends up being pulled from the battery. This results in immediate overheating and potential damage of the electrical hardware. In order to solve this problem, alternative motor drivers or lower voltage stepper

motors could be used (see Section 4.2). However, for this system, the 12V/2A wall power supply will be used with an extension cord for the mobile module.

3.1.2.3 LED Tracking Target

Included in this section are the results for the mobile module LED tracking target methods included in section 2.1.2.3.

The goal of the LED tracking target being centered around the Raspberry Pi camera of the stationary base module when the two modules are aligned was met. This was mostly due to the specific design of the Raspberry Pi Camera extension arm mount added to the stationary base module. There are still slight offsets that can be corrected through physical adjustments made during future tests (explained further in section 2.2).

The successful operation of the LED tracking target was confirmed through the execution of the test described in the Methods section. Figure 3.1.3 (left) depicts the tracking target green hexagon being independently illuminated. Figure 3.1.3 (right) then depicts the addition of the blue feedback LED being turned on. As depicted, both functionalities of the LED tracking target are independently operational and properly controlled by the Raspberry Pi and powered by the 5 V wall power supply.

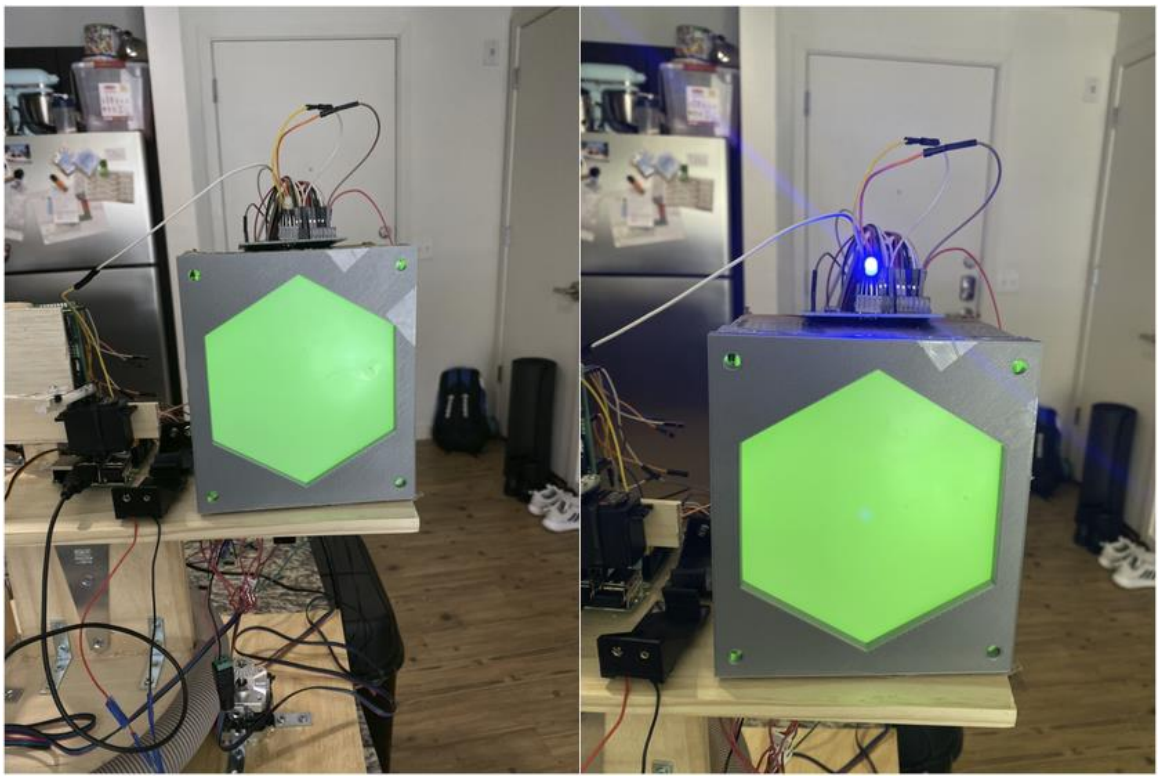

Figure 3.1.3: Mobile Module LED Tracking Target Connectivity and Power Up Test

3.1.2.4 PD, PD Operating Circuit, and ADC

The successful mounting of the PD, PD operating circuit, and ADC was confirmed through the testing of the range of motion of the X-Y axis plane. The PD as able to move through the full range of motion without physically limiting the function of the motors. Also, all wired connections were maintained and posed no problems. Therefore, functionality was maintained throughout the movement.

Successful operation of the PD, PD operating circuit, and ADC was confirmed through the execution of the test described in the Methods section. Figure 3.1.4 depicts the graph produced by the Raspberry Pi test program that measured the cell phone LED being waved directly in front of the PD. The variations in measured voltages reflect the random movements of the phone LED and confirm that the PD, PD operating circuit, and ADC have maintained their

functionality and are able to measure and record incident optical power on the PD properly. Note that the physical mounting of the hardware on to the mobile module is assumed to have no effect on the measurement accuracy (which was confirmed in Section 1.7).

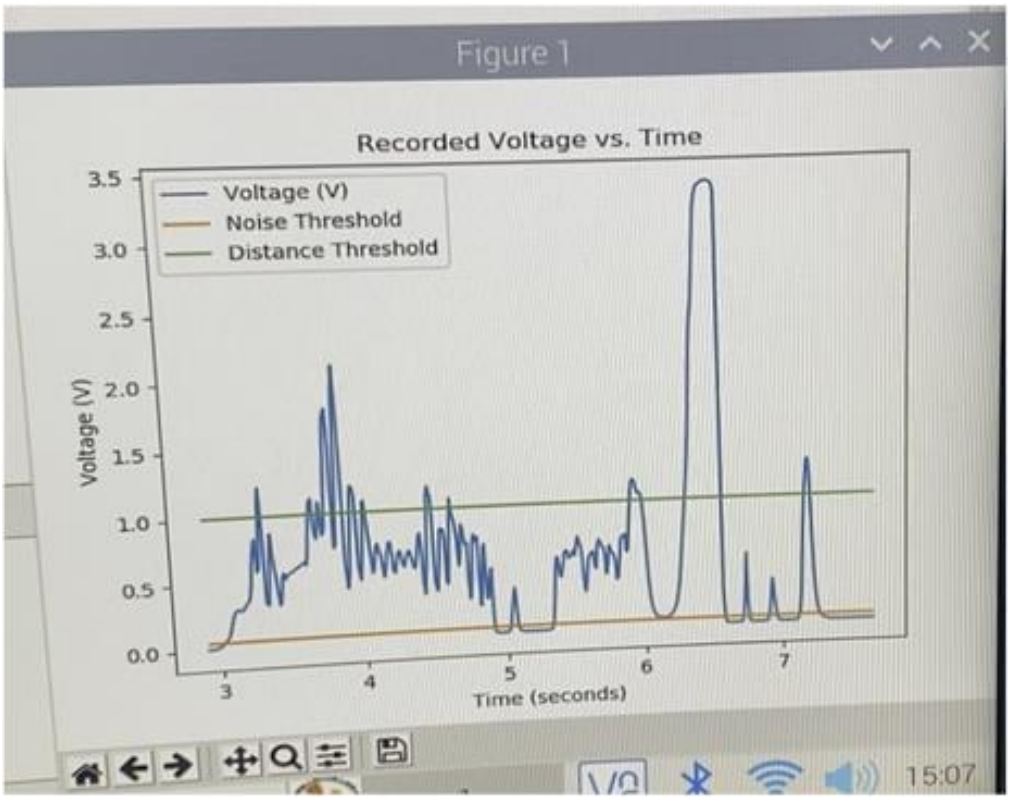

Figure 3.1.4: Measured Voltages from PD, PD Operating Circuit, and ADC During Functionality Test

3.2 Module Location and Alignment

Module Location and Alignment consists of developing and implementing the necessary algorithms in code for both the Stationary Module and Mobile Module to align themselves with one another using their tracking targets and Raspberry Pi Cameras. This phase also includes any additional hardware updates to the modules necessary to facilitate this process. Following these updates, the functionality of the modules to locate and align with one another will be tested, the methods by which will be included in section 2.2 while the results will be included in this section.

3.2.1 Module Location and Alignment Algorithms

The Module Location and Alignment Algorithms as described by the processes depicted in the flow charts of section 2.2.1 were implemented on the Raspberry Pi of each module. In the process of completing this, the necessary physical changes to Raspberry Pi Camera mounting described in section 3.2.2 were discovered.

3.2.2 Raspberry Pi Camera Mounting Updates

In the process of implementing the Module Location and Alignment Algorithms described in section 2.2.1, necessary updates to the Raspberry Pi Camera mounting were discovered. Primarily, it became clear that the plane of the Raspberry Pi Cameras transverse to the optical path between the modules needs to be aligned closely to the plane of the tracking targets. Any deviation in this regard can result in slight misalignments. That is, deviations can result in the opposite tracking target being centered in the Raspberry Pi Camera's field of view, but the actual module remains misaligned. In order to solve this problem, it was necessary to manually adjust the tilt of the Raspberry Pi Cameras using physical mounting materials. Additionally, it was discovered the Raspberry Pi Camera mounting on the Mobile Module was not well centered, and a new mounting location on the front of the X-Y axis frame rather than the back of the X-Y axis frame was decided. These updates are shown for the Stationary Module in Figure 3.2.1 and for the Mobile Module in Figure 3.2.2.

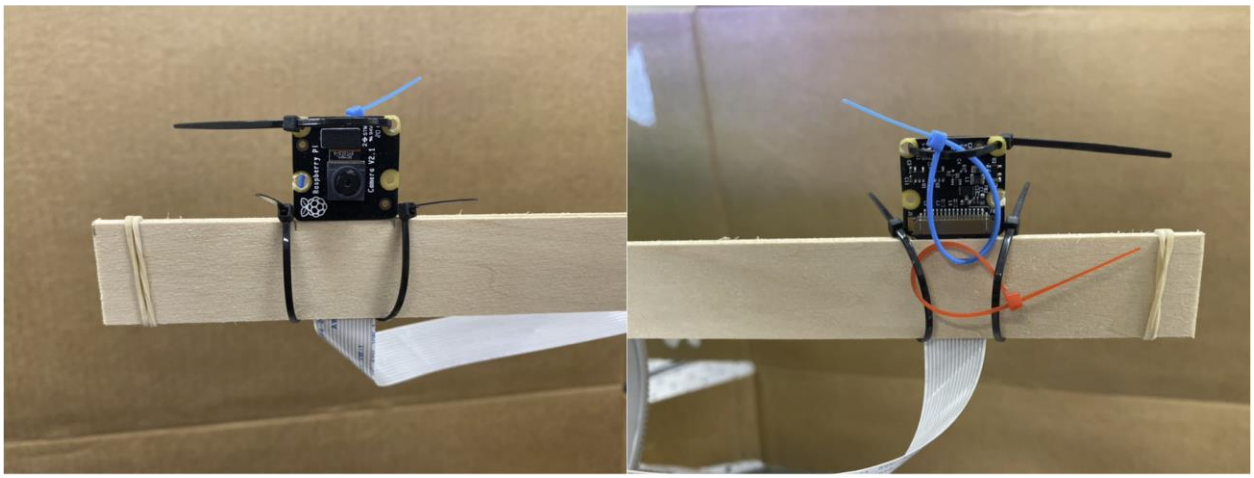

Figure 3.2.1: Stationary Module Raspberry Pi Camera Mounting Update

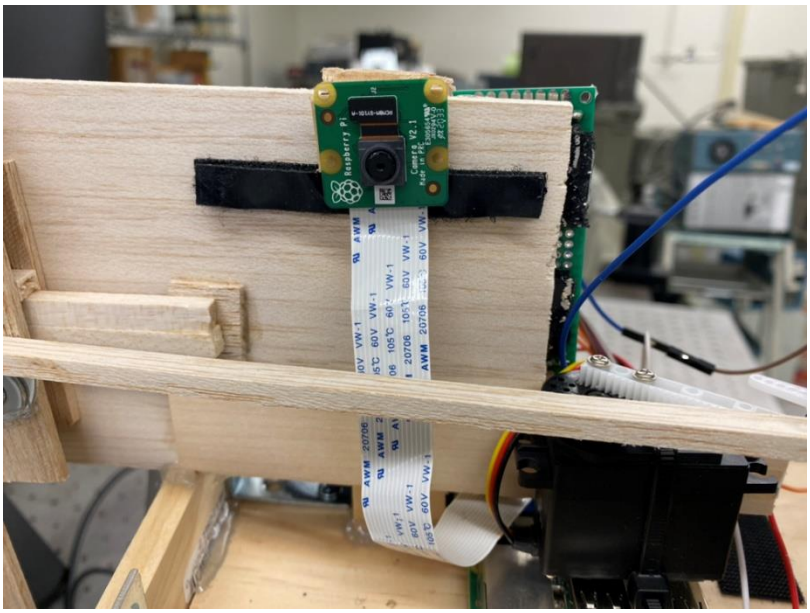

Figure 3.2.2: Mobile Module Raspberry Pi Camera Mounting Update

3.2.3 Module Location and Alignment Testing

After performing the tests outlined in section 2.2.3, the functionality of the implemented Module Location and Alignment algorithms and updated Raspberry Pi Camera mounting was confirmed. An additional test at a distance of 3.7 meters was included for the mobile module.

The results of these tests are included in Table 3.2.1. Note that these tests include a calibration sequence for the stepper motors which adds a considerable amount of time.

Table 3.2.1: Module Location and Alignment Test Results

Module Search and Alignment Tests			
Module	Distance (m)	Alignment Time (s)	Pass/Fail
Stationary	1	148	Pass
Stationary	5	194	Pass
Stationary	10	211	Pass
Mobile	1	189	Pass
Mobile	3.7	164	Pass
Mobile	5	203	Pass
Mobile	10	142	Pass
Success Criteria: Module centers opposite module's tracking target in its Pi Camera's FOV			

To give insight into the general test setup, some pictures from one of the test cases will be provided. For the Stationary Module test at 5 meters, Figure 3.2.3 (top) shows the initially unaligned modules. Figure 3.2.3 (middle) then shows the modules after alignment. Finally, Figure 3.2.3 (bottom) shows the tracking target of the Mobile Module centered with in that Stationary Module's Raspberry Pi Camera's field of view. It also shows the calculated spherical coordinate offsets from the center (exhibiting milliradian accuracy). These results sufficiently demonstrate the satisfaction of the requirements for Module Location and Alignment as described in section 2.2. That is, each module can consistently center the opposite module's tracking target in its Raspberry Pi Camera's field of view. With these results, movement into the Establishing RSL and Inter-Module Power Transfer phase will begin. Noted improvements to test in future phases will include updating the pixel-width vs distance function, testing how both modules handle simultaneous alignment, and handling failure propagation cases like sweeping an empty steradian range and notifying the user.

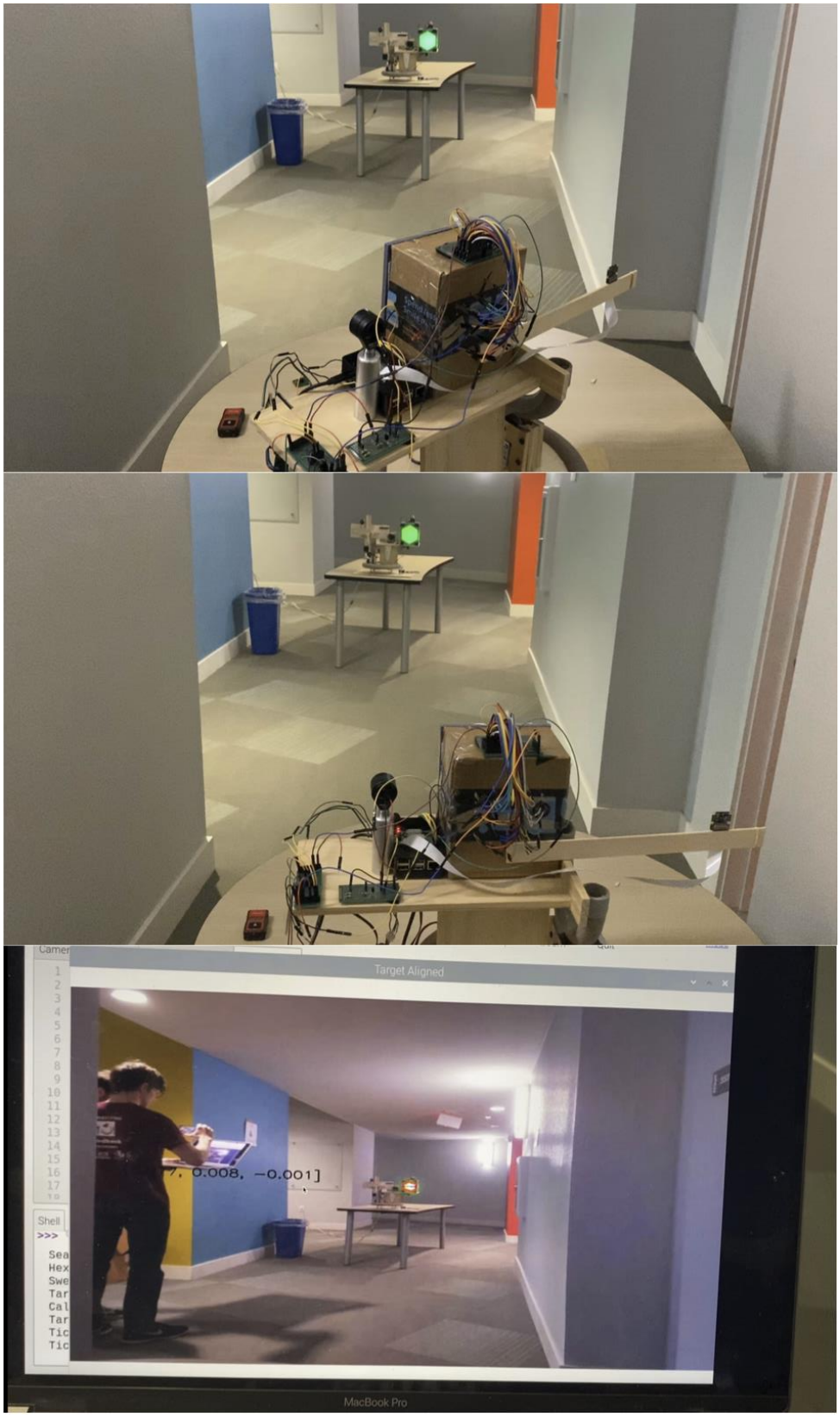

Figure 3.2.3: Example Module Location and Alignment Test Case Photos (Stationary Module, 5 meters)

3.3 Establishing RSL and Inter-Module Power Transfer

The Establishing RSL and Inter-Module Power Transfer phase concerns three major components. The first is confirming the beam characteristics of the collimated VCSEL mounted on the Stationary Module. Next, the optical path distance measurements completed in section 1.6 need to be reproduced for the integrated system. This also includes updating the physical mounting and alignment of the VCSEL optomechanical mount with respect to other Stationary Module components. Finally, the feedback mechanisms and remaining processes leading up to establishing the Representative Stationary Link (RSL) need to be implemented in code. Following these components, the functionality of the Establishing RSL and Inter-Module Power Transfer phase will be tested, the methods by which will be included in section 2.3 while the results will be included in this section.

3.3.1 VCSEL Beam Check

The first step in reexamining the VCSEL beam is to adjust the collimating lens in the lens tube of the optomechanical mount in order to optimize the VCSEL beam pattern at 10 meters. Figure 3.3.1 (left) depicts the beam pattern at 10 meters observed in section 1.6. This beam pattern exhibits light and dark rings with areas of significant differences in measured voltages (as shown in the distance measurements in section 1.6). After adjusting the collimating lens and observing the changes in the VCSEL beam pattern at 10 meters, the beam pattern shown in Figure 3.3.1 (right) was chosen. It seems that adjusting the collimating lens with respect to the VCSEL diode in the lens tube results in the collimation of different modes of the VCSEL diodes. In the case of that shown in Figure 3.3.1 (right), the measured voltages are likely to be more consistent across the beam pattern. This, of course, will be confirmed through subsequent distance measurements in section 3.3.4.

Figure 3.3.1: Comparison of Old vs New Collimated VCSEL Beam Pattern at 10 Meters

The second step in reexamining the VCSEL beam is to take a look at the potential power supplies for the LDC which controls the VCSEL. This supply voltage can either be provided by the Raspberry Pi 5V pin or by a wire connected to the 5V wall power supply which powers the other constant current sources on the module. At a distance of 10 meters, the VCSEL beam was manually aligned with the PD of the Mobile Module and the measured voltages resulting from each power supply were compared. Figure 3.3.2 depicts the measured voltage against time plot generated by the Mobile Module when changing the power supply of the LDC. Evidently, the difference in the measured voltages is noticeable, with the 5V wall power supply resulting in an additional ~40 mV of measured voltage. Therefore, moving forward, the 5V wall power supply will be used over the Raspberry Pi 5V pin to ensure a better ability to distinguish the VCSEL

beam from ambient noise. The remaining measurements and tests will be performed with the LDC being powered by the 5V wall power supply.

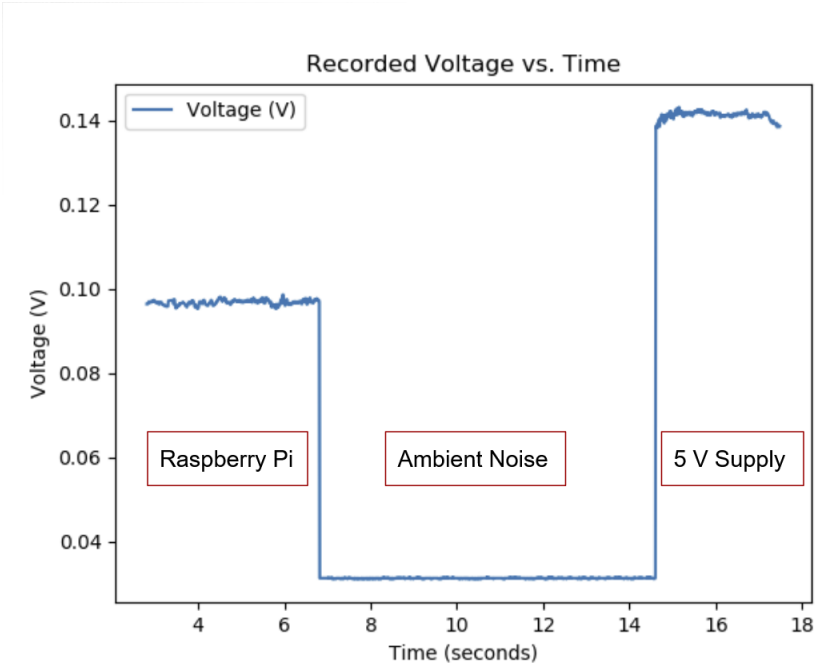

Figure 3.3.2: Comparison of Aligned VCSEL Beam Measured Voltages at 10 Meters with Different LDC Power Supplies

The final task in reexamining the VCSEL beam is to compare its measured voltage with ambient noise values for the average room. At a distance of 10 meters, the VCSEL beam will be manually aligned with the PD of the Mobile Module to preform the test. As the Mobile Module records the measured voltages read by the PD, different levels of ambient noise will be compared with the VCSEL beam. Figure 3.3.3 depicts the resulting plot of measured voltages vs time for this test. At time 0 seconds, half of the room's lights were on. They consist of overhead, broadband LED light sources. At time 9 seconds, the previously aligned VCSEL beam was turned on. Next, at time 15 seconds, the remaining lights in the room were turned on. Finally, at 19 seconds, the VCSEL beam was turned off. Evidently, the VCSEL beam is clearly distinguishable from ambient noise, as it contributes to over 100 mV of the measured voltage.

Ambient noise from the room lights, at its maximum value, contribute under 30 mV of the measured voltage. These results are consistent with those shown in section 1.6 for ambient noise measurements and confirm that the newly collimated and integrated VCSEL beam is still clearly distinguishable from ambient noise at the maximum operational range distance of 10 meters.

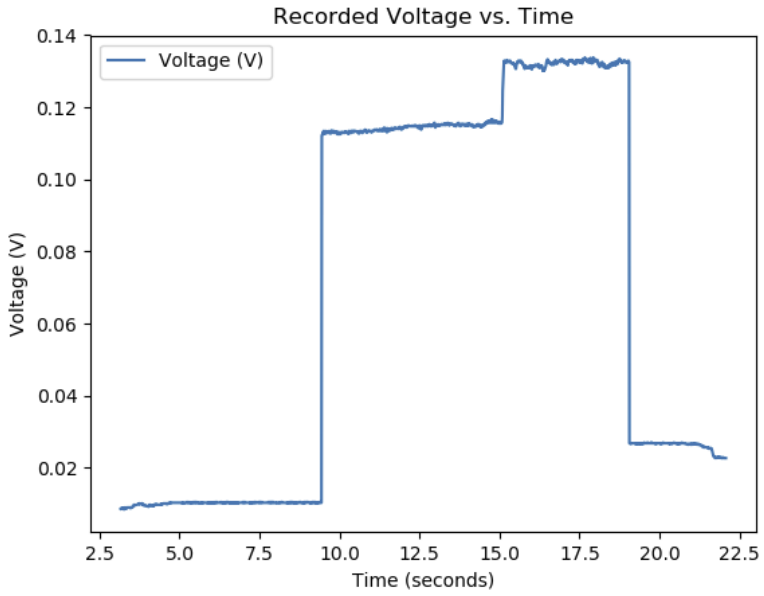

Figure 3.3.3: Measured Voltages vs Time for Ambient Noise to VCSEL Beam Comparison Test

3.3.2 Distance Measurements and Physical Alignment

Following the outlined procedures described in section 2.3.2 of the Methods section, the following test set up was devised for the distance measurements and physical alignment process. Figure 3.3.4 depicts the Stationary Module and Mobile Module manually aligned at a distance of one meter. Figure 3.3.4 (right) shows the 10 meter space by which the Mobile Module will be moved through to make the measurements. Note that tools like levels, measuring tape, and straight lines (such as those inherent to the floor tiles) facilitate manually aligning the two modules as well as making the necessary physical adjustments.

Figure 3.3.4: Distance Measurements and Physical Alignment Set Up

Following the completion of the distance measurements and physical alignment process, the VCSEL optomechanical mount had to be manually adjusted to facilitate inherent beam alignment as described in sections 2.1 and 2.3.2. Figure 3.3.5 depicts the updated appearance of the physically adjusted optomechanical mount on the Stationary Module. With this adjustment and given that the modules have been aligned properly, the VCSEL beam will be inherently incident on the PD of the Mobile Module when it is in its center of the X-Y axis range of motion.

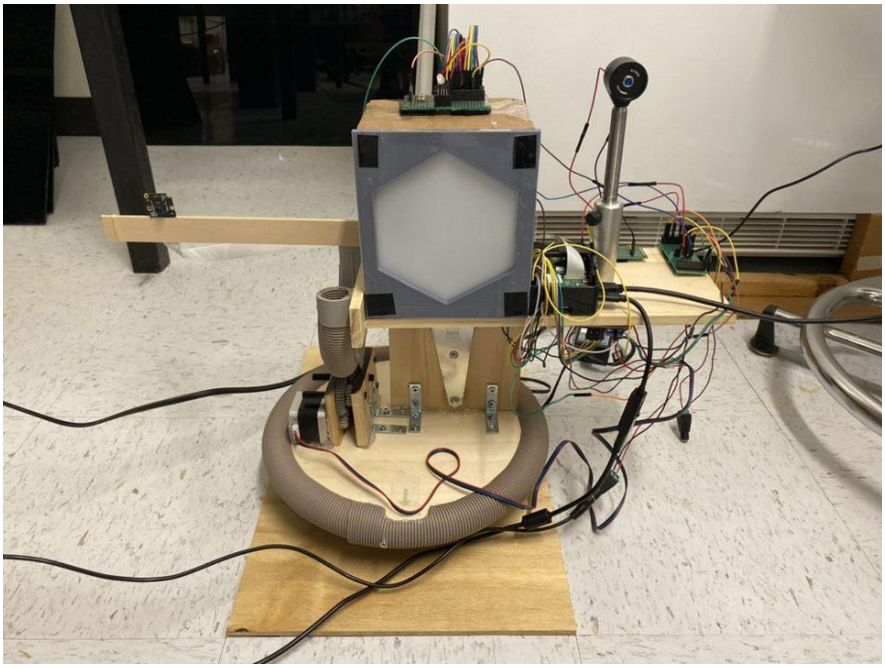

Figure 3.3.5: Updated VCSEL Optomechanical Mount on Stationary Module

The distance measurements tests are summarized in Table 3.3.1. At each distance, the pixel-width of the hexagon on the Mobile Module's tracking target was measured. Also, distance-dependent and alignment-dependent measured voltages for the VCSEL beam were successfully measured through manually alignment and the X-Y axis sweep.

Table 3.3.1: Distance Measurements Summary

Distance Measurements Tests Summary		
Distance (m)	Hexagon Pixel Width	Pass/Fail
0	372	Pass
1	93	Pass
2	53	Pass
3	38	Pass
4	31	Pass
5	26	Pass
6	21	Pass
7	18	Pass
8	16	Pass
9	N/A	Pass
10	N/A	Pass
Success Criteria: X-Y Axis was able to move the PD around the aligned beam and track the differences in the detected optical power (also, successful hexagon pixel width measurement was taken when necessary)		

The measured voltage vs time plots for three measurements (1, 5, and 10 meters) will be provided along with the beam pattern observed at that distance on the infrared sensor card. Figure 3.3.6 shows these results at 1 meter, Figure 3.3.7 shows these results at 5 meters, and Figure 3.3.8 shows these results at 10 meters.

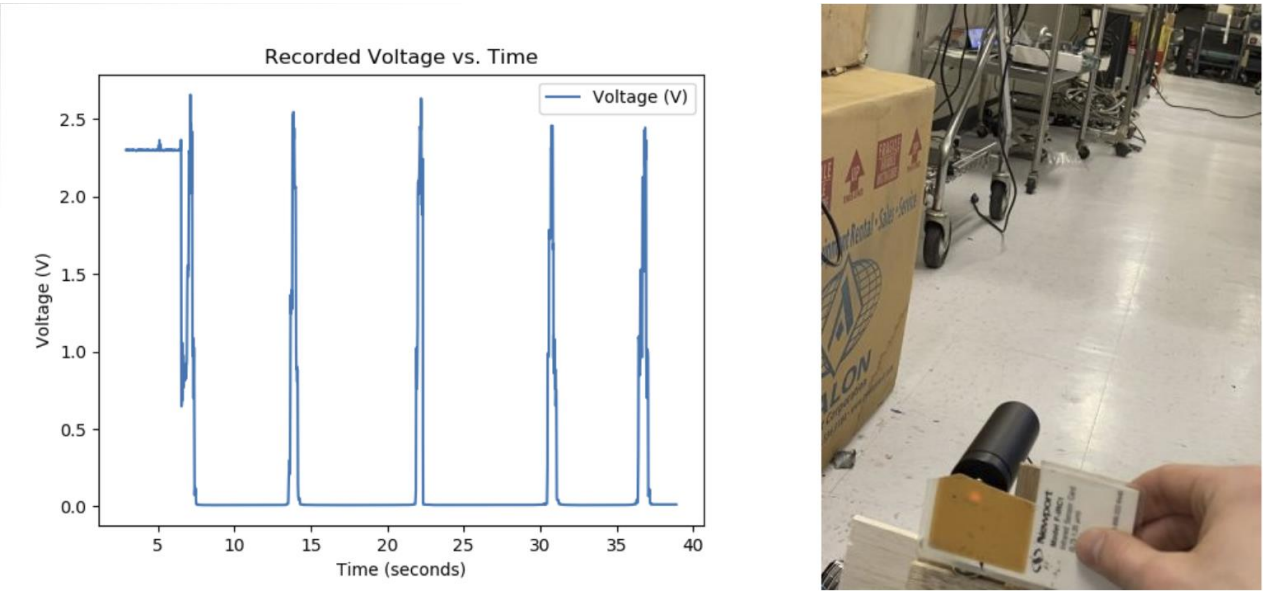

Figure 3.3.6: Distance Measurements Results at 1 Meter

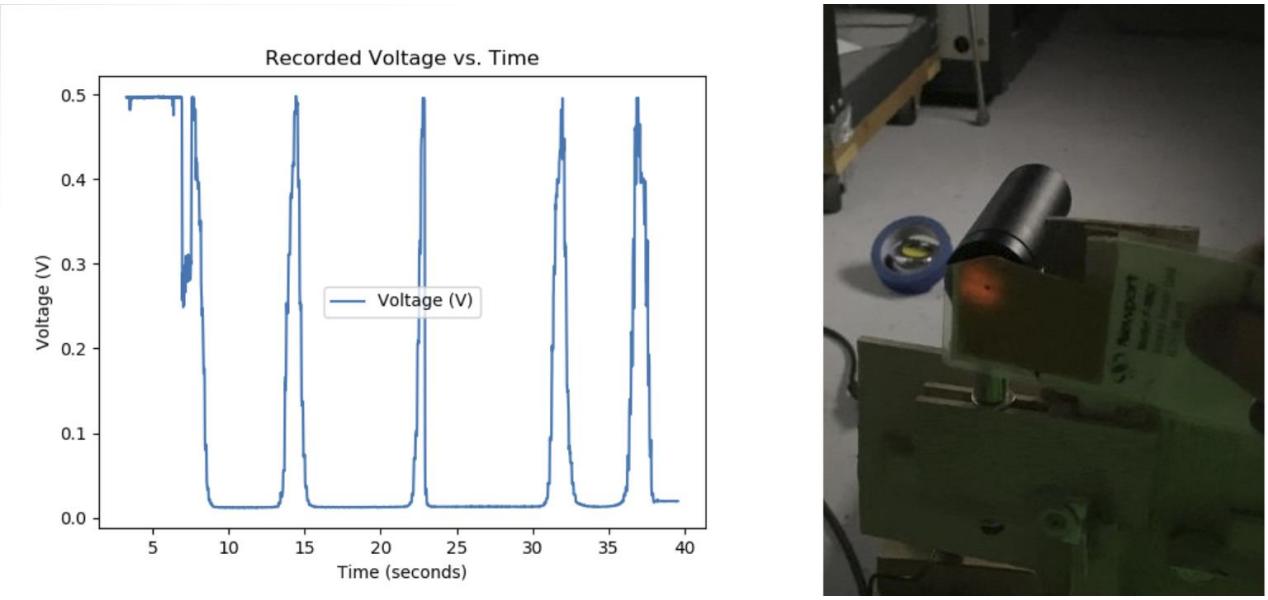

Figure 3.3.7: Distance Measurements Results at 5 Meters

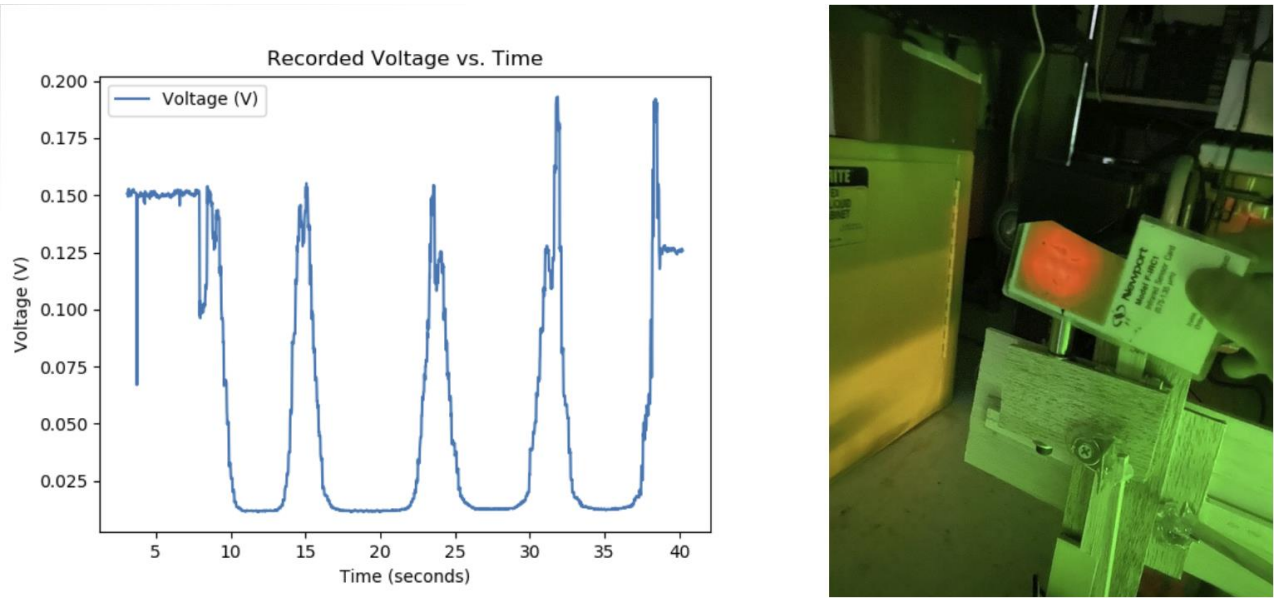

Figure 3.3.8: Distance Measurements Results at 10 Meters

Evidently, as distance increased, the peak measured voltages decreased and the length of time that the beam was distinguished from noise during the sweep increased. This corresponds to the beam expanding and its emitted optical power being spread out with distance. After examining these measured voltage vs time graphs at every distance, the maximum and minimum peak corresponding to VCSEL beam alignment were recorded and plotted vs distance using MATLAB as shown in Figure 3.3.9. It is at this point that it is noted that the PD is operating in the photoconductive (PC) mode. Section 1.6 mentioned the potential benefits of using the PV mode (lesser variability, no power from Raspberry Pi); however, once the PD, PD operating circuit, and ADC were implemented onto the Mobile Module, it became apparent that the ADC would not record the correct voltages unless its 3V3 pin from the Raspberry Pi was supplying a reverse bias to the PD operating circuit (resulting in the PC mode operation by the PD). That being said, the PC mode still operates sufficiently well and results in the VCSEL beam being clearly distinguishable from ambient noise in terms of measured voltages (as shown in Figure 3.3.9).

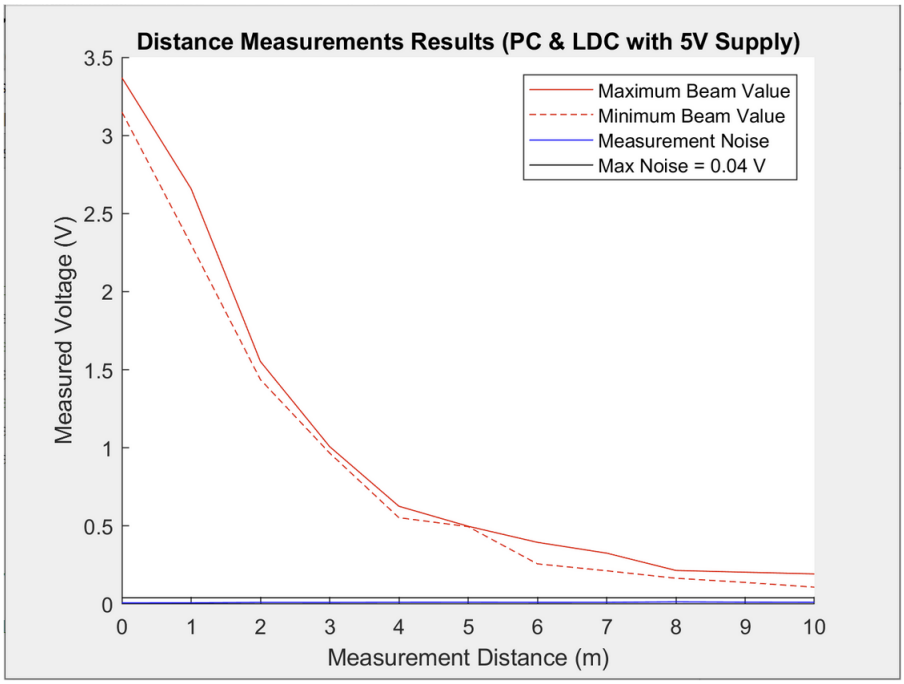

Figure 3.3.9: Maximum and Minimum VCSEL Beam Alignment Measured Voltages Across Distance

3.3.3 Establishing RSL Feedback Algorithm

The Establishing RSL Feedback Algorithm as described by the processes depicted in the flow chart of section 2.3.3 was implemented on the Raspberry Pi of each module. This implementation combined with the results of the VCSEL beam check, distance measurements, and physical alignment set the stage for the test outlined in section 2.3.4.

3.3.4 Establishing RSL and Inter-Module Power Transfer Test

Following the test described in section 2.3.4, the feedback mechanisms described in section 2.3.3 needed to complete the establishment of a RSL were demonstrated and validated. At the distance of one meter, the Stationary Module was initially offset from the Mobile Module. After completing its sweep and placing the tracking target of the Mobile Module in its Raspberry Pi Camera's field of view, the Stationary Module turned on its feedback blue LED as well as the VCSEL diode. Figure 3.3.10 (top) depicts the Stationary Module with its feedback blue LED on. Figure 3.3.10 (bottom) depicts the view of the Stationary Module's Raspberry Pi Camera with

the opposite tracking target centered in its field of view with the corresponding spherical coordinates. Moreover, in the top left of the PD, the VCSEL beam can be seen (this is due to the Raspberry Pi Camera being able to detect NIR wavelengths).

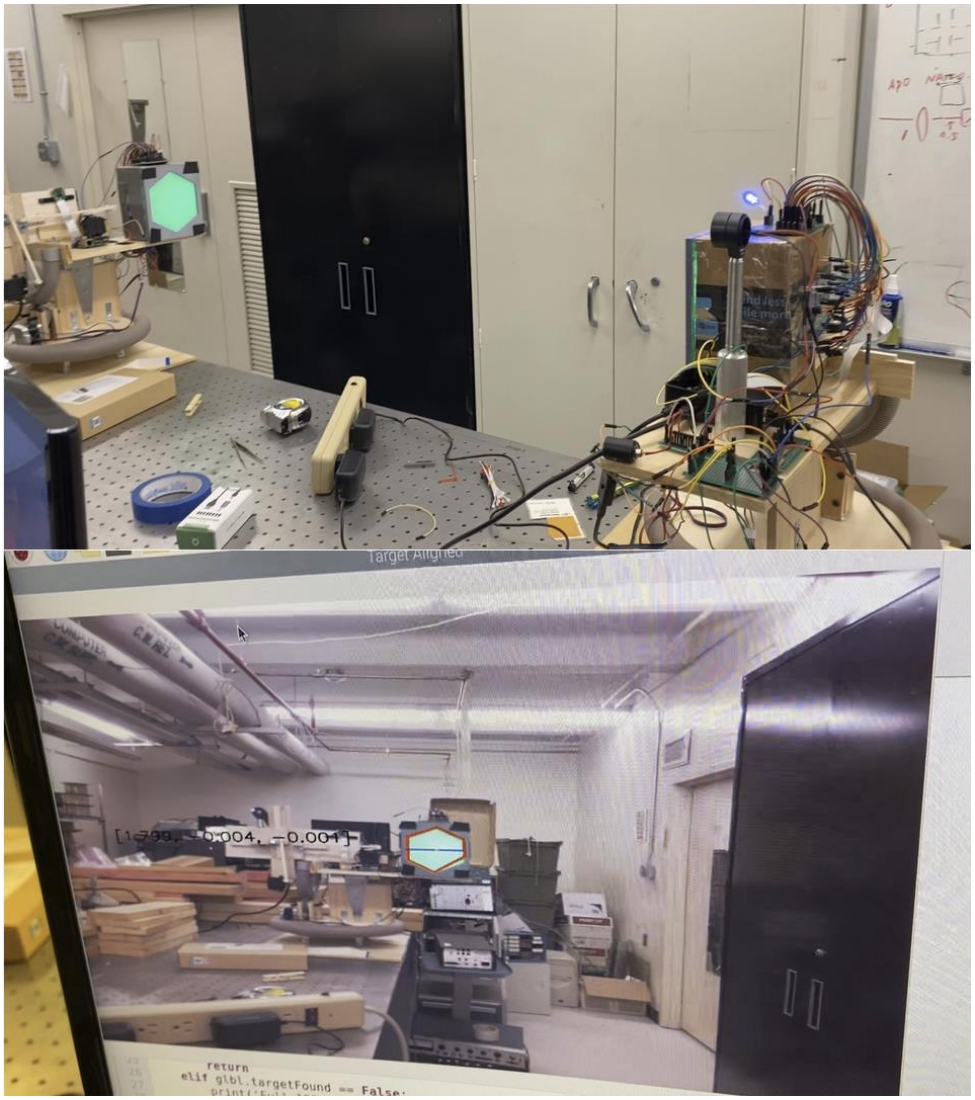

Figure 3.3.10: Stationary Module Feedback Mechanism (Top) Depicting Met Conditions (Bottom)

After the Stationary Module turned on its blue LED, the Mobile Module recognized it and finalized its alignment. After this, the PD was snaked by the X-Y axis frame searching for the beam. Once a sufficient measured voltage above the link threshold was read by the ADC, the PD stopped and the Mobile Module's own feedback blue LED was turned on. Figure 3.3.11 (top)

depicts the Mobile Module's feedback blue LED being turned on at this point. Figure 3.3.11 (middle) shows the resulting measured voltage vs time plot resulting from the link. Figure 3.3.11 (bottom) shows the alignment of the VCSEL beam with respect to the PD on the Mobile Module using the infrared sensor card. Finally, the Stationary Module recognized the feedback blue LED of the Mobile Module signifying that the RSL has been established.

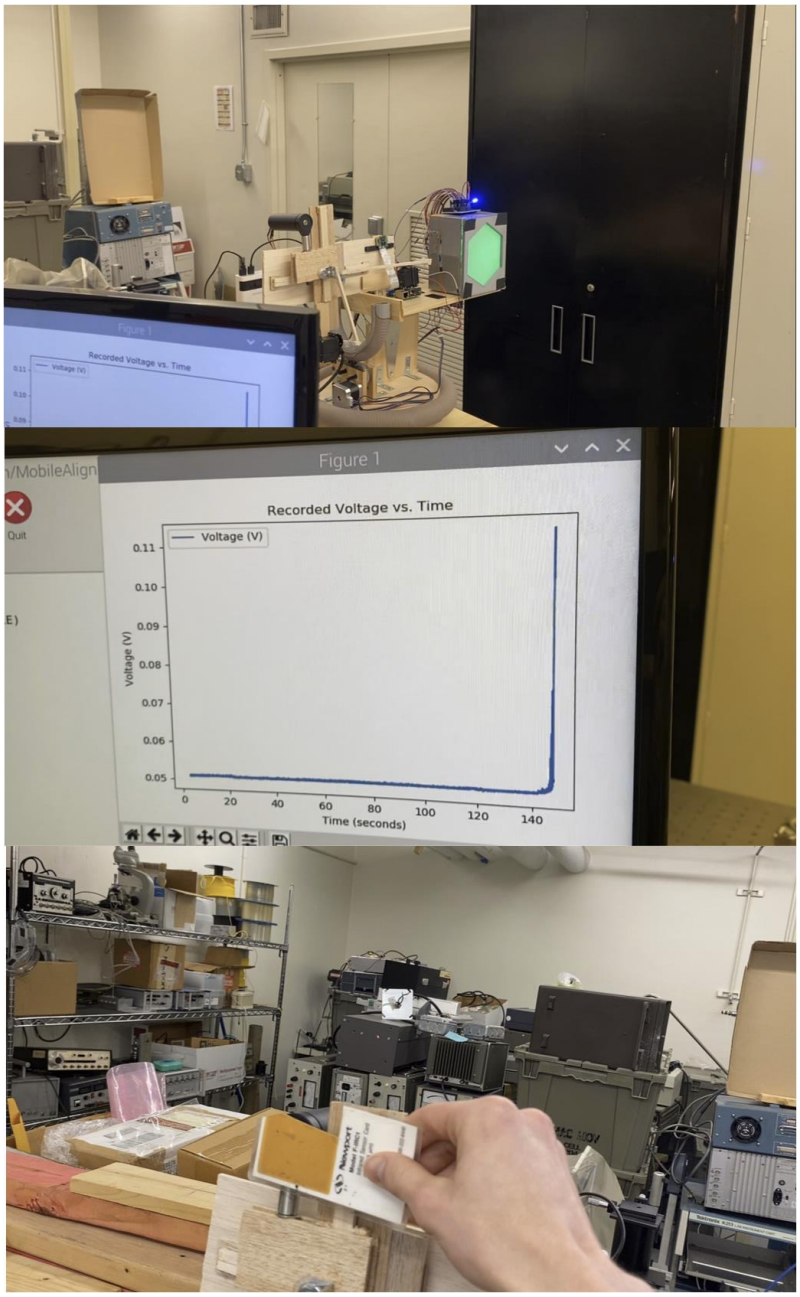

Figure 3.3.11: Mobile Module Feedback Mechanism (Top) Depicting Met Conditions (Middle and Bottom)

With the successful completion of this test, the goals of the Establishing RSL and Inter-Module Power Transfer phase has been met. This functionality will be expanded across the entire steradian and operational ranges in subsequent phases once the remaining code functionality (Restoring a Broken RSL) is implemented. Sequencing the feedback mechanisms with simultaneous module activity will also be implemented in the subsequent phases.

3.4 Restoring a Broken RSL

The Restoring a Broken RSL phase involves implementing functionality to ensure the robust establishment of an initial RSL and then introduce functionality by which to restore a broken RSL. As mandated by the system description outlined in section 1.3, the modules must be able to restore a broken RSL after mobile module movement. According to the scope and operational description of the system as described in sections 1.1, the system does not need to establish or restore a broken RSL in the event that an obstacle is left in the optical path for an extended period of time. However, an obstacle temporarily breaking the RSL and then being removed will be addressed by enabling the modules to restore the broken link. These processes can be implemented in code by following the processes outlined in the flow chart depicted in Figure 2.4.1. The processes depicted in this figure will be tested with the methods described in section 2.4 and the results included in the subsequent sections. A summary and description of the performed tests for the Restoring a Broken RSL phase are included in Table 3.4.1.

Table 3.4.1: Performed Tests for Restoring a Broken RSL Phase

Restoring Link: Performed Tests				
Test Name	Module	Test Purpose	Success Criteria	Pass/Fail
Steradian Sweep	Stationary	Failure Propagation	Stationary module scans entire steradian range and notifies user if no module was found	Pass
Steradian Sweep	Mobile	Failure Propagation	Mobile module scans entire steradian range and notifies user if no module was found	Pass
X-Y Axis Snake	Mobile	Failure Propagation	Mobile module snakes PD across entire range of X-Y axis and notifies user if no beam was found	Pass
Simultaneous Alignment	Both	Establishing RSL	RSL established with modules initially unaligned and code started simultaneously on each module	Pass
Mobile Module Obstacle	Mobile	Restoring RSL	After initial RSL, mobile module recognizes if an obstacle temporarily breaks link and then restores the link (stationary code stopped after RSL to simulate obstacle conditions)	Pass
Both Modules Obstacle	Both	Restoring RSL	After initial RSL, both modules recognize if an obstacle temporarily breaks the link and then restore the link	Pass
Mobile Module Movement	Both	Restoring RSL	After initial RSL, both modules recognize if the link is broken from mobile module movement and then restore the link	Pass
Note: Tests were performed at a distance of around one meter. Tests exhibit functionality and highlight potential errors or areas of improvement in the code that can be addressed in the Final Testing phase				

3.4.1 Failure Propagation

3.4.1.1 Empty Steradian Range

The Empty Steradian Range Failure Propagation mode described in section 2.4.1.1 was implemented on the Raspberry Pi of each module. Both modules are able to scan their entire steradian range and notify the user if no module was found. In order to test this, the horizontal and vertical Raspberry Pi Camera fields of view had to be estimated. These values were estimated by taping ends of string to edges of the Raspberry Pi Camera's field of view and bringing the strings together at the Raspberry Pi Camera and measuring the resulting angle with a protractor. Figure 3.4.1 (left) shows the vertical field of view estimated to be ~52°. Figure 3.4.1 (right) shows the horizontal field of view estimated to be ~65°.

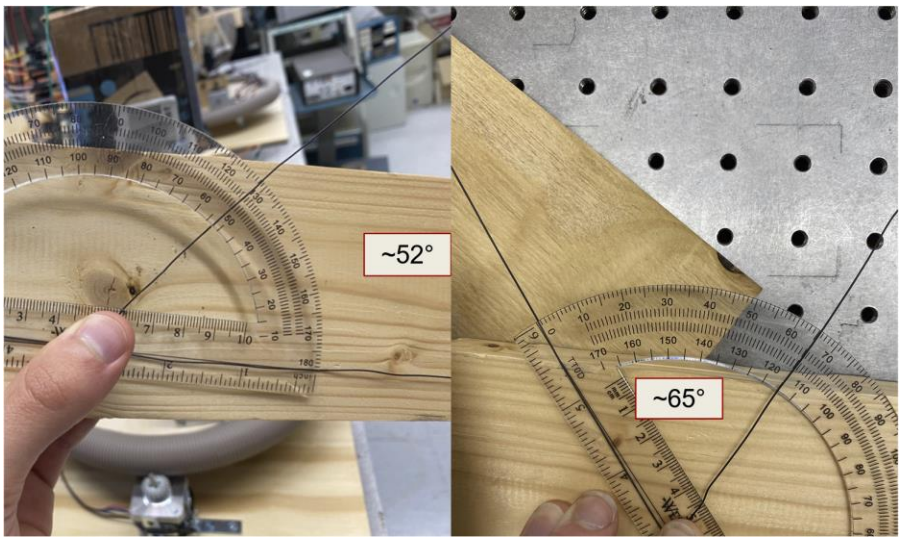

Figure 3.4.1: Raspberry Pi Camera Estimated Vertical (Left) and Horizontal (Right) Fields of View

3.4.1.2 No VCSEL Beam in X-Y Axis Range

The No VCSEL Beam in X-Y Axis Range Failure Propagation mode described in section 2.4.1.2 was implemented on the Raspberry Pi of the Mobile Module. The Mobile Module is able to snake the PD across the entire range of the X-Y axis and notifies the user if no beam was found.

3.4.2 Simultaneous Alignment

As mentioned in section 2.4.2, the modules had not completed the alignment process simultaneously until this point. After attempting and troubleshooting detected errors, the RSL can now be established with the modules being initially unaligned and with their code started simultaneously. This functionality was confirmed at a distance of 1 meter and will be further tested at other distances during the Full Steradian and Operational Range Tests and Validation phase. At this point, the code functionality depicted in Figure 2.4.1 required to restore a broken RSL can be implemented and tested.

3.4.3 Restoring a RSL Temporarily Broken by an Obstacle

The Restoring a Broken RSL Algorithm as described by the processes depicted in the flow chart (Figure 2.4.1) in section 2.4 was implemented on the Raspberry Pi of each module. After an initial RSL, a test outlined in Table 3.4.1 shows that both modules recognize if an obstacle temporarily breaks the link and then restore the link. This functionality was confirmed at a distance of 1 meter and will be further tested at other distances during the Full Steradian and Operational Range Tests and Validation phase. Figure 3.4.2 (top) shows an obstacle obstructing an established RSL and the Stationary Module recognizing that the RSL has been broken by turning its feedback blue LED off. Figure 3.4.2 (bottom) then shows that the RSL was restored after the obstacle was removed.

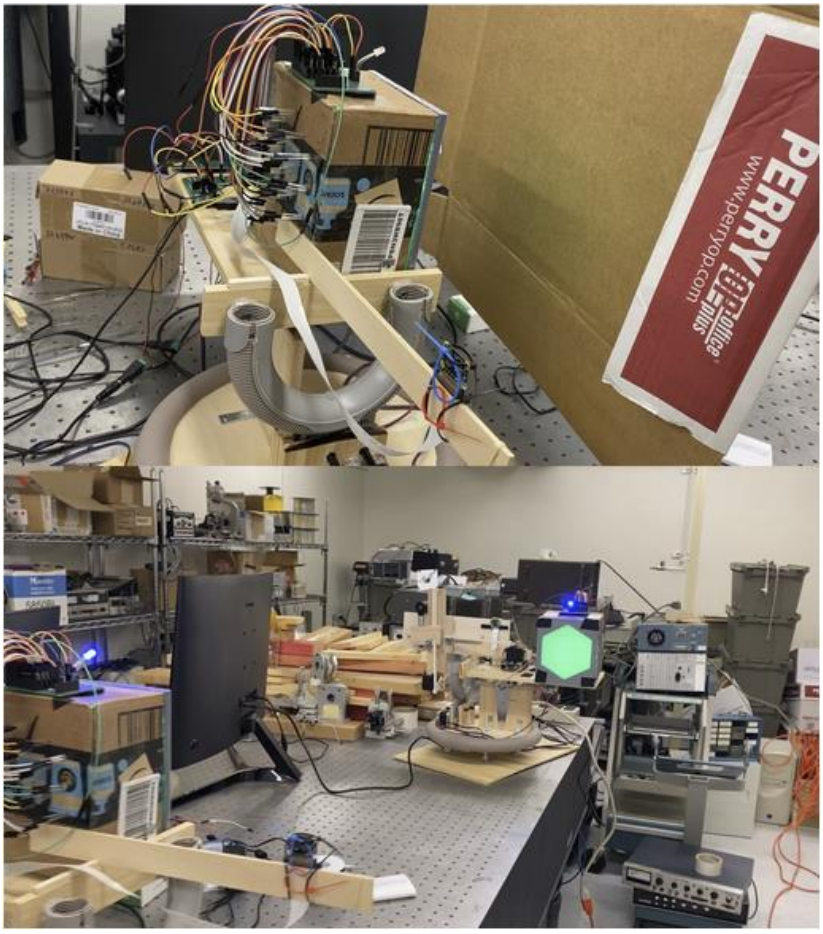

Figure 3.4.2: RSL Being Restored After an Obstacle Temporarily Breaks an Established RSL

3.4.4 Restoring a RSL After Mobile Module Movement

The Restoring a Broken RSL Algorithm as described by the processes depicted in the flow chart (Figure 2.4.1) in section 2.4 was implemented on the Raspberry Pi of each module. After an initial RSL, a test outlined in Table 3.4.2 shows that both modules recognize if the RSL is broken from Mobile Module movement and then restore the RSL. This functionality was confirmed at a distance of 1 meter and will be further tested at other distances during the Full Steradian and Operational Range Tests and Validation phase. Figure 3.4.3 (top) shows an established RSL from the perspective of the Stationary Module's Raspberry Pi Camera. The modules formed an initial link starting in the same position depicted in Figure 3.4.2 (bottom). Figure 3.4.3 (bottom) shows the restored RSL after the Mobile Module was moved.

Figure 3.4.3: RSL Being Restored After a Mobile Module Movement Breaks an Established RSL

3.5 Full Steradian and Operational Range Tests and Validation

The Full Steradian and Operational Range Tests and Validation phase consists of extending and verifying proper and consistent operation of the system throughout the entire steradian and operational range. Up until this point, system functionality for the earlier phases was tested at a distance of one meter and with only slight variation in the initial module unalignment. As mentioned in sections 1.1 and 1.3, the modules must be able to form and restore a RSL between one another whenever each module is in one another's steradian and operational range. As a reminder, the steradian range is defined as a full horizontal 180° and vertical 90° centered with respect to the module for an operational range of 1 to 10 meters. To validate system operation within the steradian and operational range, a series of tests covering the operational range at distances around one, five, and ten meters will be performed along with varying initial module unalignments corresponding to edge cases within the steradian range. At each distance, initial RSL and RSL restoration tests will be performed and the time durations for each of these RSL establishments will be recorded. The results of these tests will be included in the subsequent sections, but an overall summary of the performed tests is included in Table 3.5.1.

Table 3.5.1: Full Steradian and Operational Range Performed Tests

Steradian & Operational Range Tests				
Test Name	RSL Time (s)	RSL Restoration Time(s) (s)	Success Criteria	Pass/Fail
One Meter - RSL	375*	N/A	With initial module unalignment, an RSL was established at a distance of 1 meter	Pass
One Meter - Full	158	331, 112, 189**, 216**	With initial module unalignment, an RSL was established at a distance around 1 meter. Then, the mobile module was moved twice within the steradian ranges and the RSL was restored each time	Pass
Five Meters - RSL	160	N/A	With initial module unalignment, an RSL was established at a distance of 5 meters	Pass
Five Meters - Full	165	270, 259	With initial module unalignment, an RSL was established at a distance around 5 meters. Then, the mobile module was moved twice within the steradian ranges and the RSL was restored each time	Pass
Ten Meters - RSL	135	N/A	With initial module unalignment, an RSL was established at a distance of 10 meters	Pass
Ten Meters - Full	250	359	With initial module unalignment, an RSL was established at a distance around 10 meters. Then, the mobile module was moved once within the steradian ranges and the RSL was restored	Pass
*Times for tests that were performed before calibration procedure was removed, the time for this procedure was retrospectively removed when calculating the time(s) **Times corresponding to cases where the RSL was broken due to a system error which recovered itself Note: Tests were performed at distances near one meter, five meters, or ten meters. Tests exhibit the ability of the modules to establish and restore a Representative Stationary Link (RSL) at all distances throughout the Operational Range of one to ten meters with varying initial unalignment in the Steradian Range				

3.5.1 One Meter Testing

As shown in Table 3.5.1, at a distance of 1 meter, the One Meter – RSL and One Meter – Full tests were successfully performed. The One Meter – RSL test showed that with initial module unalignment, a RSL was established at a distance of 1 meter. The One Meter – Full test showed that with initial module unalignment, a RSL was established at a distance around 1 meter. Then, the mobile module was moved twice within the steradian ranges and the RSL was restored each time. Figure 3.5.1 (top) shows the initial unalignment for the One Meter – Full test. Figure 3.5.1 (bottom) shows the initial RSL established from the perspective of the Stationary Module's Raspberry Pi Camera.

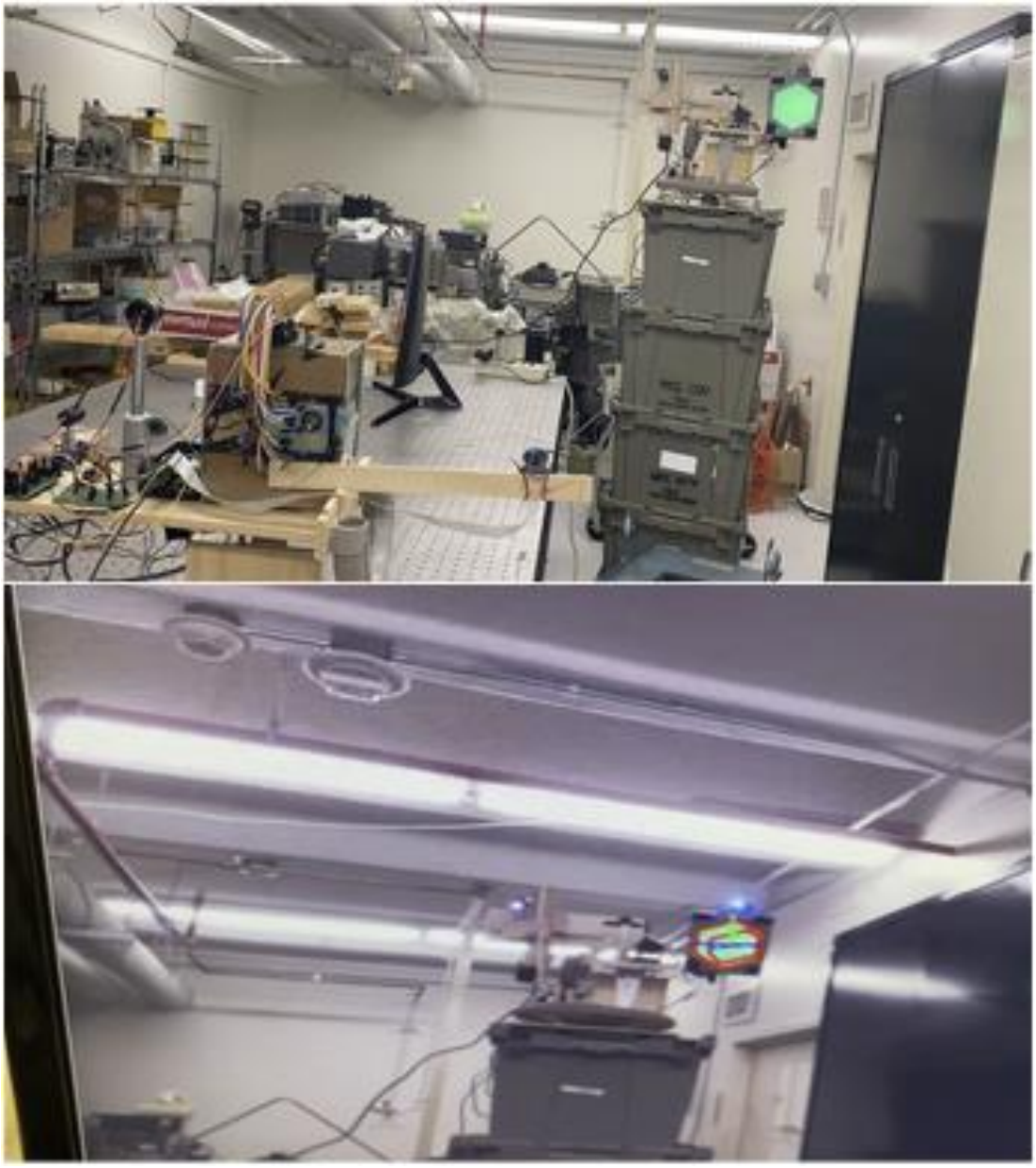

Figure 3.5.1: One Meter – Full Test Initial Module Unalignment (Top) and Initial RSL (Bottom)

Figure 3.5.2 (top) then shows the Mobile Module moved down to the table and the RSL restored after this movement from the perspective of the Stationary Module's Raspberry Pi Camera. Figure 3.5.2 (bottom) shows the Mobile Module moved again to a cart below the table and the RSL restored after this movement.

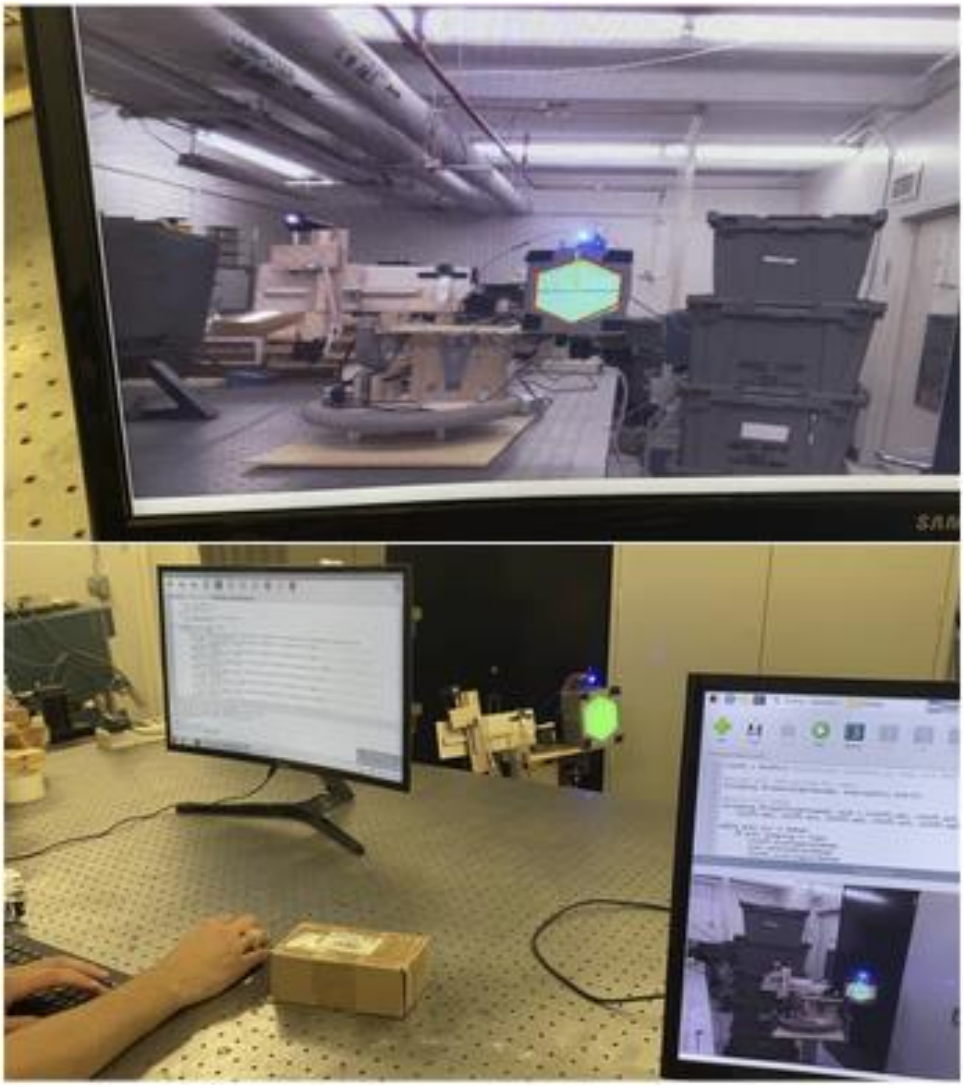

Figure 3.5.2: One Meter – Full Test First Restored RSL (Top) and Second Restored RSL (Bottom) After Mobile Module Movement

Figure 3.5.3 shows the resulting Measured Voltage vs Time plot recorded by the PD and ADC showing the peaks corresponding to the various RSLs for the One Meter – Full test. Note, as shown in the RSL Restoration times of Table 3.5.1 and the extra peaks in Figure 3.5.3, during the One Meter – Full test, the RSL was established and quickly broken immediately a couple times. This was due to a specific issue. First, the PD on the X-Y axis detected the VCSEL beam edge above the measured voltage threshold (set to 0.1 V, see sections 3.5.5 and 4.2.6) and recognized the link was established. Then, the measured voltage dropped below the measured

voltage threshold and the RSL was broken (likely due to imprecise and jumpy movements in the X-Y axis or due to variability in the VCSEL beam power). At this point, the system recognized the RSL was broken and reset the X-Y axis to its origin to begin searching for the Stationary Module again under the assumption the RSL was broken due to Mobile Module movement or an obstacle. Eventually, the X-Y axis placed the PD at a point on the VCSEL beam where the measured voltage was able to stay above the threshold. This issue was noted and solved by adding an additional lower measured voltage required to break an established RSL (set to 0.05 V, see section 3.5.5). It is noted in section 4.2.6 that this could be further addressed by adjusting the PD on the X-Y axis to become more centered on the VCSEL beam with an improved alignment algorithm.

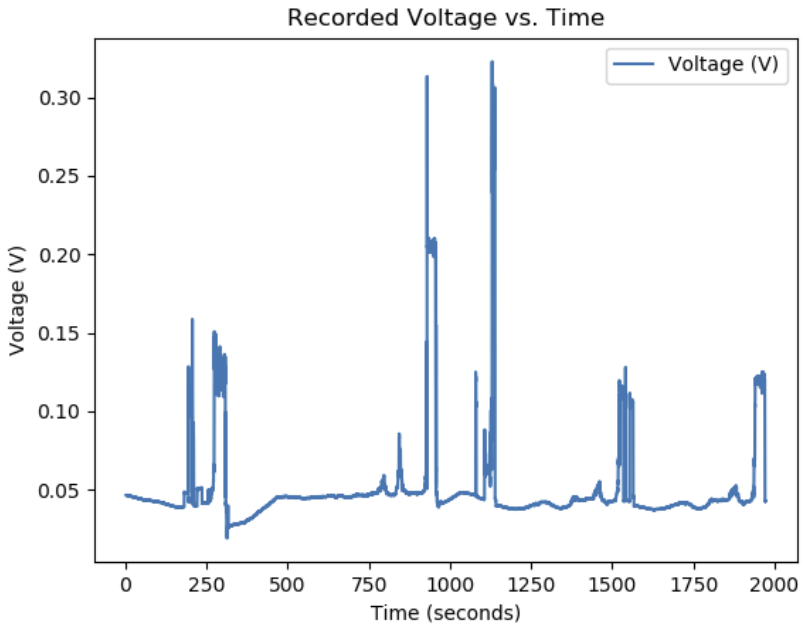

Figure 3.5.3: One Meter – Full Test Measured Voltage vs Time Plot

3.5.2 Five Meter Testing

As shown in Table 3.5.1, at a distance of 5 meters, the Five Meter – RSL and Five Meter – Full tests were successfully performed. The Five Meter – RSL test showed that with initial

module unalignment, a RSL was established at a distance of 5 meters. The Five Meter – Full test showed that with initial module unalignment, a RSL was established at a distance around 5 meters. Then, the mobile module was moved twice within the steradian ranges and the RSL was restored each time. Figure 3.5.4 (top) shows the initial unalignment for the Five Meter – Full test. Figure 3.5.4 (bottom) shows the initial RSL established from the perspective of the Stationary Module's Raspberry Pi Camera.

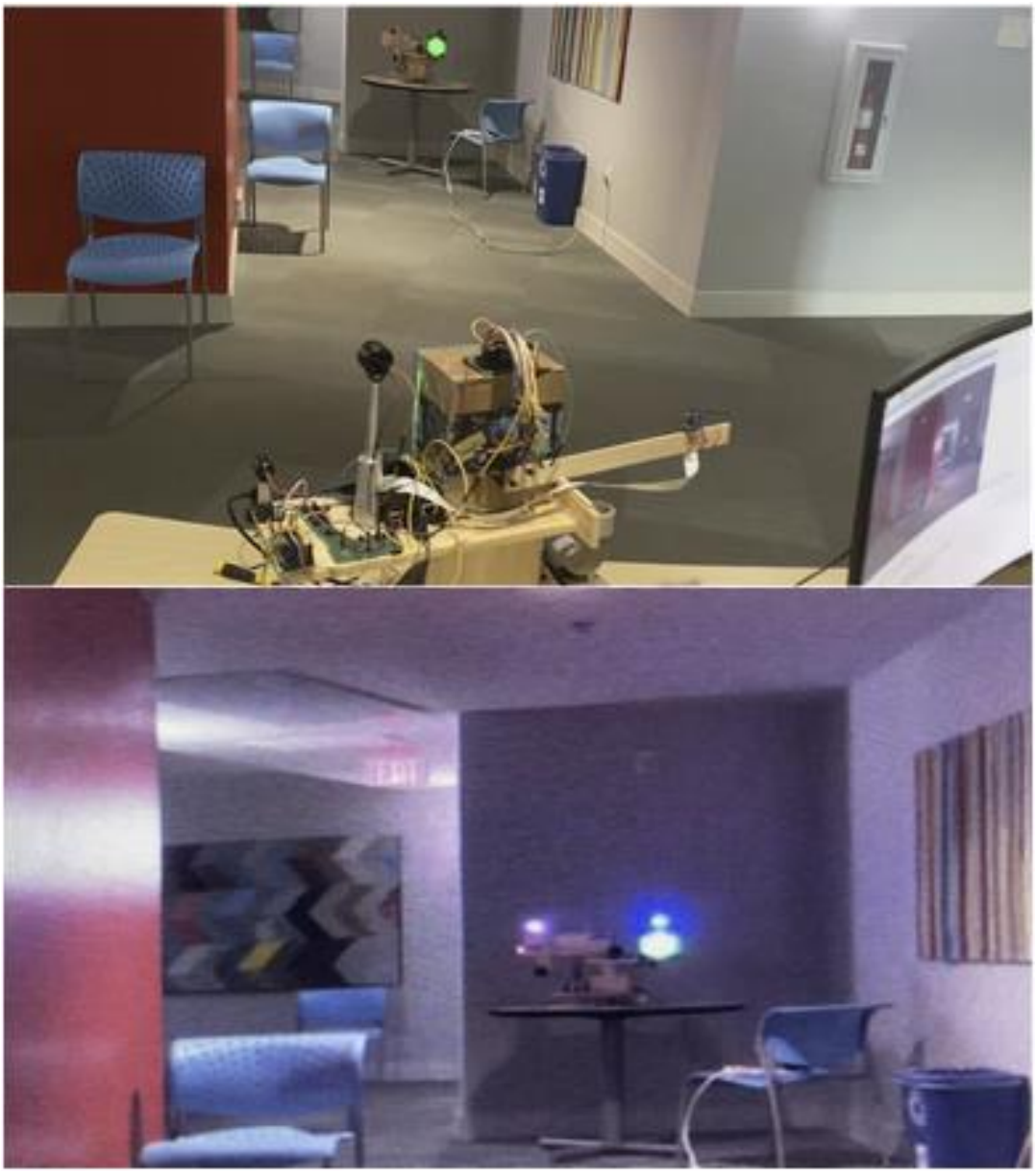

Figure 3.5.4: Five Meter – Full Test Initial Module Unalignment (Top) and Initial RSL (Bottom)

Figure 3.5.5 (top) then shows the Mobile Module moved down to the floor and the RSL restored after this movement. Figure 3.5.5 (bottom) shows the Mobile Module moved again to a chair and the RSL restored after this movement.

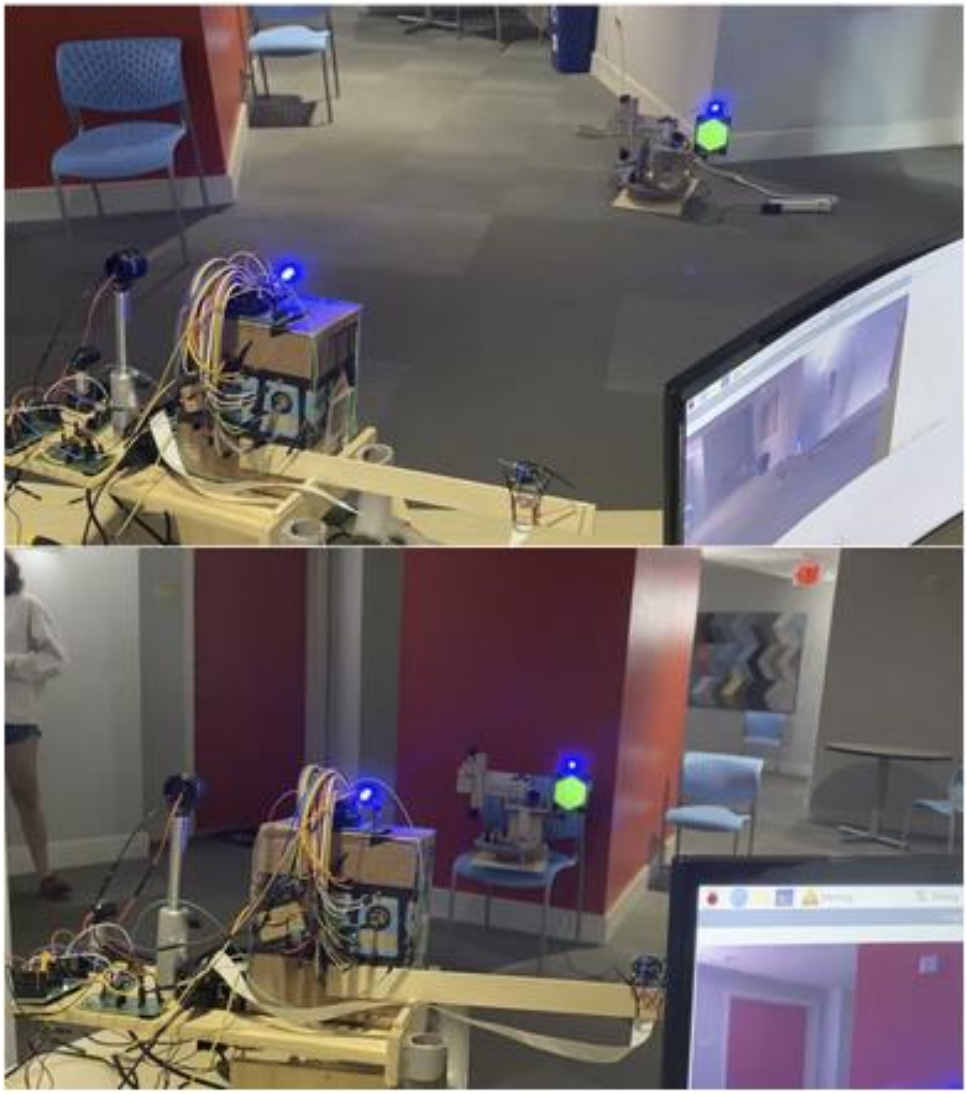

Figure 3.5.5: Five Meter – Full Test First Restored RSL (Top) and Second Restored RSL (Bottom) After Mobile Module Movement

Figure 3.5.6 shows the resulting Measured Voltage vs Time plot recorded by the PD and ADC showing the peaks corresponding to the various RSLs for the Five Meter – Full test. With the code adjustment mentioned in section 3.5.1, the additional RSL peak and system reset errors were absent.

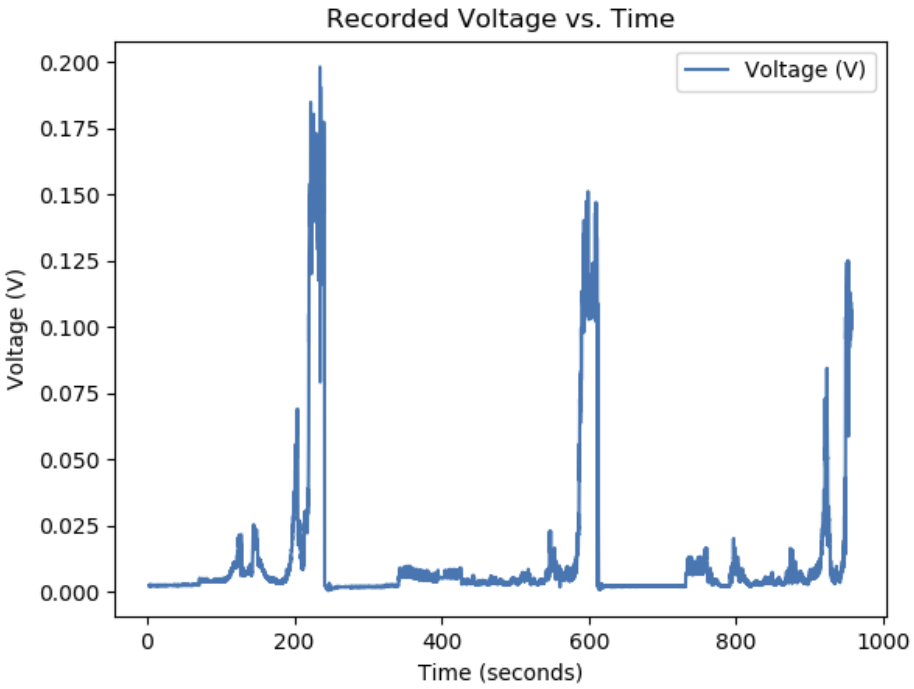

Figure 3.5.6: Five Meter – Full Test Measured Voltage vs Time Plot

3.5.3 Ten Meter Testing

As shown in Table 3.5.1, at a distance of 10 meters, the ten Meter – RSL and Ten Meter – Full tests were successfully performed. The Ten Meter – RSL test showed that with initial module unalignment, a RSL was established at a distance of 10 meters. The 10 Meter – Full test showed that with initial module unalignment, a RSL was established at a distance around 10 meters. Then, the mobile module was moved within the steradian ranges and the RSL was restored. Figure 3.5.7 (top) shows the initial unalignment for the Ten Meter – Full test. Figure 3.5.4 (middle) shows the initial RSL established. Figure 3.5.7 (bottom) then shows the Mobile Module moved to a different hallway onto a chair and the RSL restored. Figure 3.5.8 shows the resulting Measured Voltage vs Time plot recorded by the PD and ADC showing the peaks corresponding to the various RSLs for the Ten Meter – Full test. With the code adjustment mentioned in section 3.5.1, the additional RSL peak and system reset errors were absent.

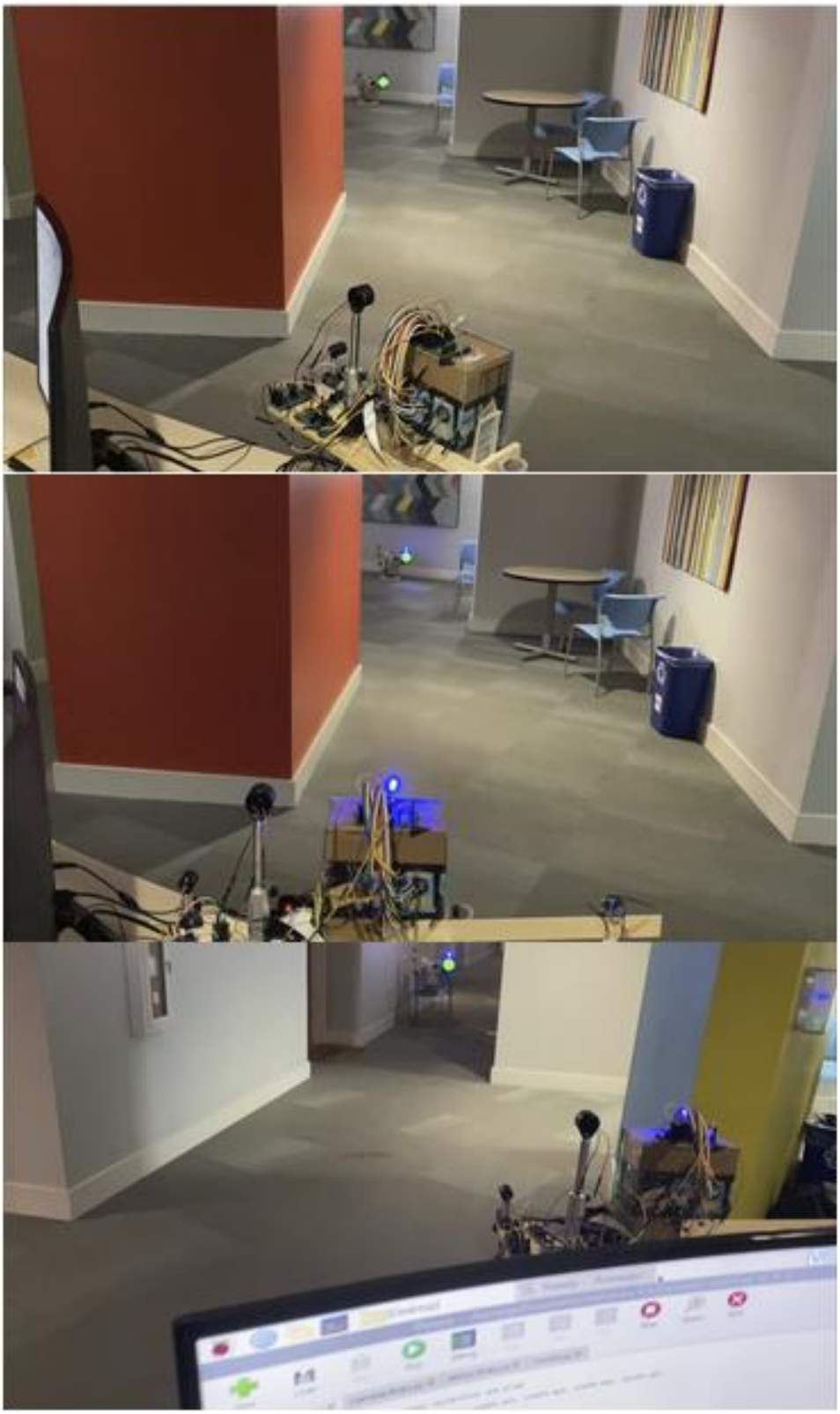

Figure 3.5.7: Ten Meter – Full Test Initial Module Unalignment (Top), Initial RSL (Middle), and Restored RSL After Mobile Module Movement (Bottom)

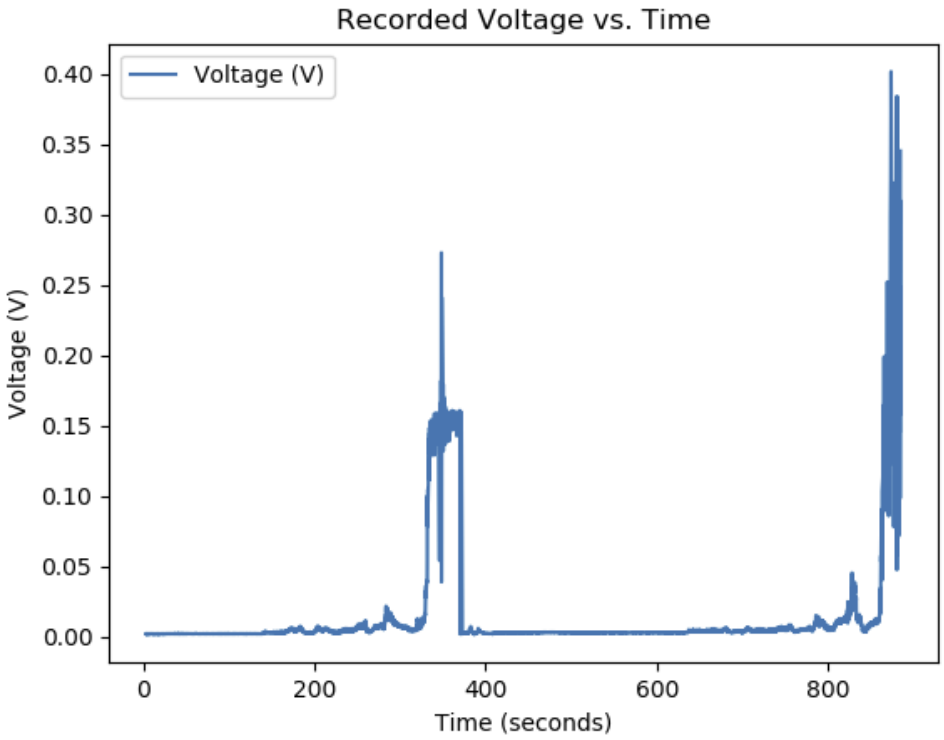

Figure 3.5.8: Ten Meter – Full Test Measured Voltage vs Time Plot

3.5.4 RSL Establishment Times

Table 3.5.1 provides the times for establishing the initial and restored RSLs for each test, and the various times have a wide range of values. With a range from 112 to 375 seconds, there is a lot of variability in the amount of time required to establish the RSLs. This variability is a direct result of the different various unalignments of the modules within one another's steradian and operational range. The time taken to complete the sweeping process, alignment corrections, and X-Y axis snaking process of each module is entirely dependent on this the initial unalignment of the modules attempting to form the RSL. Moreover, some of the feedback processes result in one module waiting for another to finish a certain part of the RSL establishment or re-establishment process. Therefore, this variability is expected and unavoidable with the current system design and defined steradian and operational range. However, each of

these processes have the potential to be individually sped up by improving upon the code algorithm, physical hardware, and Raspberry Pi model (see section 4.2).

3.5.5 RSL Measured Voltage Threshold

Based on the combined distance-dependent and alignment-dependent measurements of sections 1.6.2 and 3.3.2, the measured voltage threshold was set to 0.1 V. This threshold defines the minimum voltage measured by the ADC required to constitute the establishment of a RSL. That is, this measured voltage threshold corresponds to enough of an alignment of the PD with a VCSEL beam such that the VCSEL beam is clearly distinguishable from ambient noise throughout the entire steradian and operational range. Sections 1.6.2 and 3.3.2 showed that the ambient noise measurements had a maximum value around 40-50 mV. Therefore, the measured voltage threshold of 0.1 V corresponds to a signal-to-noise ratio of at least 2. A consequence of this design choice is that the PD will likely not be perfectly aligned with the VCSEL beam since the ADC will measure a voltage above the threshold when the PD approaches the radial edges of the beam at shorter distances. Section 4.2.6 provides a recommended solution.

As mentioned in section 3.5.1, jumpy movements in the X-Y axis frame and variability in the measured voltage readings necessitated a lower measured voltage threshold which corresponds to the maximum measured voltage that can be measured before an established RSL is recognized to be broken. This value was set to 0.05 V which is the maximum ambient noise value from sections 1.6.2 and 3.3.2. If there is an established RSL and the measured voltage of the ADC drops below 0.05 V, the Mobile Module will recognize that the RSL has been broken.

Note that the stepper motor calibration procedure used in the One Meter – RSL test and the earlier phases of system development was deemed unnecessary and was removed from the alignment process. This change was made after noticing that the stepper motors on each module

could sufficiently align the modules as required without having to complete the calibration procedure. This reduced the RSL establishment and re-establishment times by a few minutes.

3.5.6 Test Laser Diode

Sections 3.5.1 – 3.5.3 contain figures which show a new piece of hardware on the Stationary Module. In order to assist with testing, a visible test laser diode was mounted to the Stationary Module and aligned with the VCSEL beam. This allows for the general location of the VCSEL beam to be known during tests, and it serves as a reminder that the non-visible VCSEL beam is on for safety reasons. As Figure 3.5.9 shows, the test laser diode was mounted to the Stationary Module using optomechanical hardware. Note that a CCS protoboard was designed and attached to the Stationary Module as well in order to power the test laser diode (with the supply voltage supplied by the 5 V wall power supply). The design for this CCS was identical to that used for the tracking target, since the test laser diode used requires a near 20 mA drive current. Also, the test laser diode was mounted and aligned with the VCSEL mount such that the test laser diode beam would never end up in the range of the PD on the X-Y axis. This avoids any additional optical power contributing to the measured voltages of the ADC.

As mentioned before and shown in previous figures, the Raspberry Pi Camera is able to detect the NIR wavelengths of the VCSEL beam. Therefore, the Stationary Module's Raspberry Pi Camera's view was observed during testing to see where the VCSEL beam was during the alignment process. The test laser diode did not pose any concerns in this regard, as the two beam spots were sufficiently distinguishable. Figure 3.5.10 (top) shows the red visible beam of the test laser diode to the lower left of the white/purple beam of the VCSEL diode at a distance of one meter from the perspective of the Stationary Module's Raspberry Pi Camera. Figure 3.5.10 (bottom) shows the same beam spots at a distance of ten meters.

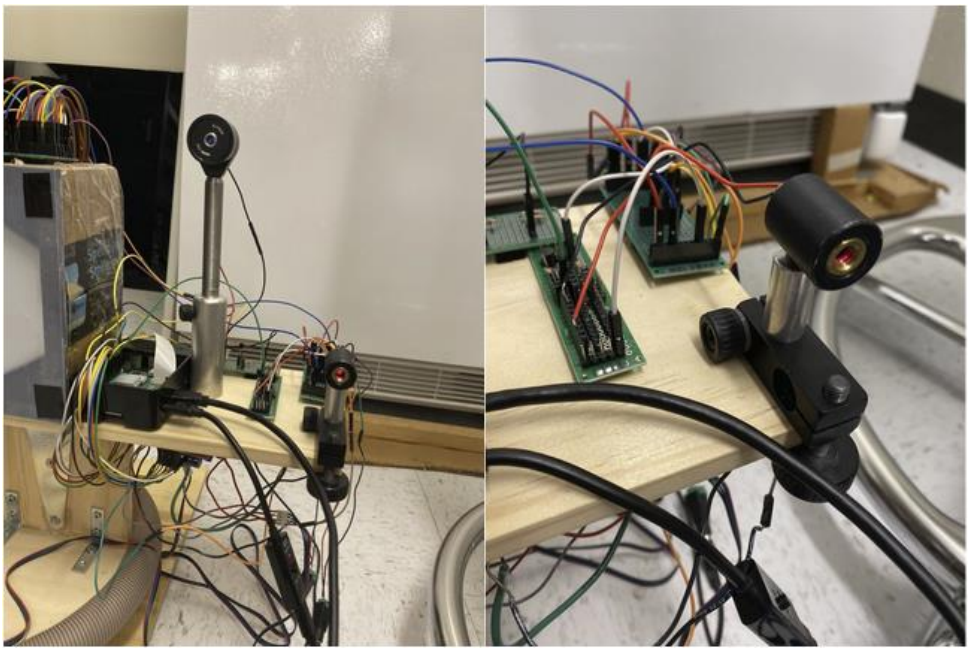

3.5.9: Test Laser Diode and CCS Mounted on Stationary Module

Figure 3.5.10: Test Laser Diode and VCSEL Diode Beam Spots Seen by the Stationary Module's Raspberry Pi Camera at Distances of One Meter (Top) and Ten Meters (Bottom)

4. CONCLUSIONS

After the completion, testing, and validation of the Light Fidelity Tracking System, several conclusions relating to system performance, comparisons to existing research, and future recommendations can be drawn. These conclusions will be included in the following sections.

4.1 System Performance

4.1.1 System Evaluation

The Light Fidelity Tracking System has satisfied its requirements as outlined in sections 1.1-1.3. The system is able to successfully establish an initial RSL and restore a broken RSL between the Stationary Module and the Mobile Module throughout the entire steradian and operational range. After doing so, the measured voltage of the ADC on the Mobile Module corresponding to the VCSEL beam alignment with the PD is clearly distinguishable from ambient noise. Due to the inherent variability of potential test cases, the time required to establish and restore an RSL ranges from about 100 to 400 seconds.

4.1.2 System Limitations

Limitations to system performance revolve around aspects of the system that restrict or complicate alignment. While these limitations did not prevent successful system performance, they are areas that can be improved upon and would limit system performance if the steradian and operational range were increased. These limitations are the following:

- Gear Ratio: The gear ratios of the Stationary and Mobile Modules paired with the stepper motors place an inherent angle-based limitation on the alignment capability of the modules. As a result, every tick of the stepper motors for the horizontal sweep and vertical tilt of the modules has an angular resolution of about 0.105-0.115 degrees (see

section 1.4). As distance increases, this angular resolution becomes non-negligible and may limit system performance at distances larger than the operational range.

- Collimated VCSEL Beam: Since the collimating lens was chosen to suit the defined operational range (see section 1.6), the VCSEL beam would expand further at larger distances. This would result in the VCSEL beam becoming less distinguishable from ambient noise. At a certain point, the beam radius would be so large that it would be indistinguishable from ambient noise.
- X-Y Axis Range: The X-Y axis has a finite range of movement for the PD. It was designed to compensate slight misalignments between the modules and allow for the VCSEL beam to be found and aligned with the PD. As distances increase and the misalignments collectively get larger, the X-Y axis range will eventually be insufficient to cover the misalignments unless it is expanded.
- Mounting of Raspberry Pi Camera and VCSEL Diode on Stationary Module: The Raspberry Pi Camera is the primary method by which the Stationary Module is aligned with the Mobile Module by centering the Mobile Module's tracking target in its field of view. As such, it is not necessarily the transverse plane of the Stationary Module which is aligned with the Mobile Module, but the transverse plane of the Raspberry Pi Camera. Therefore, any misalignments between the transverse plane of the Raspberry Pi Camera and the transverse plane of the VCSEL diode in its optomechanical mount will result in non-normal radiation of the VCSEL beam. These misalignments are existent and are a result of how the two components are mounted on the Stationary Module. Over large distances, this angular misalignment will become a larger issue, much like the discussion related to the gear ratios. The inverse case (the PD on the Mobile Module) is not a

comparable issue because of the negligible effect of small incident angle offsets on the PD measured voltages (see section 1.6.2.4).

4.1.3 System Cost

The Light Fidelity Tracking System achieved its goals with a relatively low cost. Expensive aspects of the project include the Raspberry Pis, Raspberry Pi Cameras, optical path components, motors, motor drivers, gears, portable batteries, and materials needed for the module bases (wood, hardware, etc.). The cost of all these components could be significantly reduced when considering the potential cost reductions their manufacturability could produce. That is, mass production of the modules would permit lower cost individual components that could be specifically designed for the system rather than having to be independently bought and adapted to fit the system. An example would be the ability to mass produce gears (see section 4.2.3) and the physical components needed for the module bases which would avoid the need to buy gears as part of an expensive toy kit or being limited to expensive materials and hardware for the module bases.

The cost of the Light Fidelity Tracking System (a gross estimate of under $1000) is relatively low compared to existing OWC tracking methods such as those which rely on many more expensive optical components (i.e. by beam steering) [4, 5]. That being said, adapting the Light Fidelity Tracking System would require altering the optical path to support actual OWC components. Of course, this would introduce further costs; however, the absence of a need for exceedingly expensive optical components for tracking purposes like spatial light modulators (over $10,000) and the potential for manufacturable, cheap, and plastic lenses (see section 4.2.7) could keep the overall price relatively low.

4.2 Recommendations

The following sections outline various recommendations that have been developed over the course of evaluating the Light Fidelity Tracking System. Those attempting to use, improve upon, or learn from the Light Fidelity Tracking System should consider these recommendations as potential improvements or alternative approaches.

4.2.1 Motors

The stepper motors used within the Stationary and Mobile Modules required 12V at 2A. Finding a cost effective, commercial portable battery that was capable of supplying sufficient power was difficult due to the high voltage. Using motors with lower power requirements would make portable power of the stepper motors simpler, given that the user wanted to continue to use the L298N motor drivers. Furthermore, the current stepper motors do not offer positioning feedback. The use of hall sensors would allow for such feedback and are therefore recommended in future iterations of this system.

4.2.2 Motor Drivers

The L298N motor drivers were determined to be incapable of current regulation, a discovery made after a portable battery trial on the mobile module. After further research, this determination was solidified by retailer information regarding the L298N. Due to this lack of current regulation, the stepper motors were more difficult to portably power in terms of budgetary and time allowance. In order to combat this problem, motor drivers that offer current regulation are recommended. Using current regulated motor drivers would allow for the use of a lithium-ion portable battery in conjunction with DC boosters; this combination would offer a stable voltage at a variable current to the motor drivers. The alternative option would be to use different stepper motors, as detailed in section 4.2.1.

4.2.3 Gears

The gears used within the Stationary and Mobile Modules consist of toy gears from a parts kit alongside makeshift gears formed from vacuum tubes. Although these gears perform the necessary tasks, there are more robust gear solutions available. Due to the COVID-19 pandemic, 3D printing the desired gears with the proper material was not a feasible option. The 3D printers within the Texas A&M University Fischer Engineering Design Center (FEDC) could not produce a gear large enough to meet the needs of the system. Given proper consultation with a solid works subject matter expert to determine gear characteristics and a larger available printer space, the gears could have been 3D printed. The use of 3D printed gears would offer more robustness within the modules and a more aesthetically cohesive appearance.

4.2.4 Tracking Method

While an LED backlit hexagon was functional, the tracking target was large and restricted the size of the modules. To minimize module size, a new target methodology might rely on infrared vision or GPS sensors. Upon testing, it was discovered that the Raspberry Pi camera has decent visibility of infrared light and could see the VCSEL beam from the stationary module. This suggests that infrared reflectors on each module might be a sufficient substitute for the camera vision algorithm when paired with infrared masking. Alternatively, enabling Bluetooth with a cheap GPS module for the Pi could dramatically speed up the process by allowing remote location transmission irrespective of visibility. Utilizing GPS, Bluetooth, and infrared sensors all together could dramatically reduce sweeping time.

4.2.5 Tracking Algorithm and Code

Integrating the Pi's built-in Bluetooth capabilities would allow for more consistent communication of feedback. Data transmission would still occur via the RSL, but Bluetooth

feedback could replace the blue LED as a means of communicating link status and allow additional status checks for which piece of the algorithm the modules are currently running. Additionally, our project currently uses one Raspberry Pi 4 and one Raspberry Pi 3b. Running both modules on a Raspberry Pi 4 would increase the processing power of the mobile module and potentially lead to more accurate behavior stemming from increased capability.

4.2.6 X-Y Axis Alignment Process

As mentioned in section 3.5.5, the current code implementation for establishing a RSL involves monitoring the measured voltages of the ADC of the Mobile Module and the use of an initial measured voltage threshold of 0.1 V to define the establishment of a RSL and a lower measured voltage threshold of 0.05 V to define the breaking of an established RSL. These thresholds set the main limitations of the X-Y Axis Alignment Process. That is, once the Mobile Module completes its alignment and begins snaking the PD on the X-Y axis, it will stop the PD adjustment as soon as the initial measured voltage threshold is surpassed. As shown in sections 1.6.2 and 3.3.2, the measured voltages can be much higher than this threshold of 0.1 V for different distances and levels of alignment of the PD with the VCSEL beam. This means that perfect alignment of the VCSEL beam with the PD would correspond to measured voltages much higher than the threshold (see Figure 3.3.9). Therefore, the current X-Y Axis Alignment Process provides a minimum level of alignment of the PD with the VCSEL beam by stopping the PD as it approaches the VCSEL beam spot before optimal alignment is achieved. For the Light Fidelity Tracking System, this level of alignment was acceptable; however, if optimized alignment and signal-to-noise ratios are desired, then a modification would be recommended.

Instead of the provided X-Y Axis Alignment Process, one could modify the process by implementing code functionality to find the maximum measured voltage of the ADC

corresponding to optimal alignment of the PD with the VCSEL beam at a given distance. Using the data from section 3.3.2 and shown in Figure 3.3.9 paired with the distance calculations of the Module Search Subsystem (see section 1.5), one could set distance-dependent thresholds for the measured voltages. By doing so, the X-Y axis would continue snaking the PD until a closer to optimal alignment is achieved.

4.2.7 Optical Path Components

The optical path component selection process outlined in section 1.6 can certainly be improved upon. After working with the chosen components and learning through the course of developing the system, several potential improvements or alternative choices were noted.

If cost is a predominant concern, the consideration of a cheaper lens for collimating the VCSEL diode should be addressed. The chosen glass aspheric lens from Thorlabs was certainly sufficient, but its quality and cost may have been more than needed. Considering cheaper, plastic lenses (most likely still aspheric) should certainly be considered. If one could find plastic lenses of a similar focal length with suitable optomechanical mounts, the necessary collimation may still be possible. This is an avenue to research that could potentially reduce the overall cost of the Light Fidelity Tracking System by a significant amount.

By using an isolated VCSEL diode and PD, it will be difficult to directly adapt the Light Fidelity Tracking System into a proper LiFi communication system. That is, using the Light Fidelity Tracking System as a tracking method for an actual LiFi communication system would likely require changing the entire optical path. In order to avoid this, the Light Fidelity Tracking System could be redesigned with an optical path consisting of actual LiFi communication system optical components. One example could be attaching fiber optic connectors to the necessary free space optical components (i.e. beam expanders, GRIN lenses, fiber optic couplers, etc.) so that

actual fiber optic devices (i.e. laser sources, modulators, power meters, etc.) could be directly connected to the system without requiring a lot of modification. However, this would likely increase the cost of the Light Fidelity Tracking System due to the need for additional optical components.

REFERENCES

[1] M. Chowdhury, “A Comparative Survey of Optical Wireless Technologies: Architectures and Applications”, Arxiv.org. [Online]. Available: https://arxiv.org/pdf/1810.02594.pdf. [Accessed: 01- Sep- 2020].

[2] H. Haas, L. Yin, Y. Wang and C. Chen, “What is LiFi?”, Ieeexplore.ieee.org, 2015. [Online]. Available: https://ieeexplore.ieee.org/document/7360112. [Accessed: 07- Sep- 2020].

[3] H. Lu et al., “A 56 Gb/s PAM4 VCSEL-Based LiFi Transmission With Two-Stage Injection-Locked Technique”, Ieeexplore.ieee.org, 2016. [Online]. Available: https://ieeexplore.ieee.org/stamp/stamp.jsp?arnumber=7778224. [Accessed: 01- Sep- 2020].

[4] M. Wolf, J. Li, L. Grobe, D. O. Brien, and H. Le Minh, “Challenges in Gbps Wireless Optical Transmission,” Mob. Light. Wirel. Syst., vol. 45, pp. 484–495, 2010.

[5] A. Gomez, K. Shi, C. Quintana, G. Faulkner, B. C. Thomsen, M. Ieee, D. O. Brien, and M. Ieee, “A 50 Gb / s Transparent Indoor Optical Wireless Communications Link with an Integrated Localization and Tracking System,” J. Light. Technol., vol. 34, no. 10, pp. 1–8, 2016.

[6] “Laser Safety Program Manual”, Ehs.tamu.edu. [Online]. Available: https://ehs.tamu.edu/media/1176296/Laser%20Safety%20Manual.pdf. [Accessed: 01- Sep-2020].

[7] “IEEE 802.15.7-2018 - IEEE Standard for Local and metropolitan area networks--Part 15.7: Short-Range Optical Wireless Communications”, Standards.ieee.org, 2019. [Online]. Available: https://standards.ieee.org/standard/802_15_4-2020.html. [Accessed: 31- Aug- 2020].

[8] “ANSI Z136.8 - Safe Use of Lasers in Research, Development, or Testing”, The Laser Institute. [Online]. Available: https://www.lia.org/resources/laser-safety-information/laser-safety-standards/ansi-z136-standards/z136-8. [Accessed: 01- Sep- 2020].

[9] E. Hecht, Optics, 5th ed. Boston: Pearson, 2016.

[10] “Choosing a Collimation Lens for Your Laser Diode,” Laser Diodes: Ø3.8 mm, TO-46, Ø5.6 mm, Ø9 mm, and Ø9.5 mm TO Cans. [Online]. Available: https://www.thorlabs.com/newgrouppage9.cfm?objectgroup_id=5260. [Accessed: 27-Feb-2021].